

**AFRL-SN-WP-TR-2005-1039**

**ULTRA-LOW THRESHOLD VERTICAL-  
CAVITY SURFACE-EMITTING LASERS  
FOR USAF APPLICATIONS**



**Thomas R. Nelson, Jr., Ph.D.**

**Electron Devices Branch (AFRL/SNDD)**

**Aerospace Components Division**

**Sensors Directorate**

**Air Force Research Laboratory, Air Force Materiel Command**

**Wright-Patterson Air Force Base, OH 45433-7320**

**JANUARY 2005**

**Final Report for 01 March 1996 – 31 December 2002**

**Approved for public release; distribution is unlimited.**

**STINFO FINAL REPORT**

**SENSORS DIRECTORATE**

**AIR FORCE RESEARCH LABORATORY**

**AIR FORCE MATERIEL COMMAND**

**WRIGHT-PATTERSON AIR FORCE BASE, OH 45433-7320**

## NOTICE

Using Government drawings, specifications, or other data included in this document for any purpose other than Government procurement does not in any way obligate the U.S. Government. The fact that the Government formulated or supplied the drawings, specifications, or other data does not license the holder or any other person or corporation; or convey any rights or permission to manufacture, use, or sell any patented invention that may relate to them.

This report has been reviewed and is releasable to the National Technical Information Service (NTIS). It will be available to the general public, including foreign nationals.

This technical report has been reviewed and is approved for publication.

/s/

---

THOMAS R. NELSON, Project Engineer  
Electron Devices Branch  
Aerospace Components Division

/s/

---

KENICHI NAKANO, Chief  
Electron Devices Branch  
Aerospace Components Division

/s/

---

ROBERT T. KEMERLEY, Chief  
Aerospace Components Division  
Sensors Directorate

This report is published in the interest of scientific and technical information exchange and does not constitute approval or disapproval of its ideas or findings.

REPORT DOCUMENTATION PAGE					Form Approved OMB No. 0704-0188	
<p>The public reporting burden for this collection of information is estimated to average 1 hour per response, including the time for reviewing instructions, searching existing data sources, gathering and maintaining the data needed, and completing and reviewing the collection of information. Send comments regarding this burden estimate or any other aspect of this collection of information, including suggestions for reducing this burden, to Department of Defense, Washington Headquarters Services, Directorate for Information Operations and Reports (0704-0188), 1215 Jefferson Davis Highway, Suite 1204, Arlington, VA 22202-4302. Respondents should be aware that notwithstanding any other provision of law, no person shall be subject to any penalty for failing to comply with a collection of information if it does not display a currently valid OMB control number. <b>PLEASE DO NOT RETURN YOUR FORM TO THE ABOVE ADDRESS.</b></p>						
1. REPORT DATE (DD-MM-YY) January 2005		2. REPORT TYPE Final		3. DATES COVERED (From - To) 03/01/1996 – 12/31/2002		
4. TITLE AND SUBTITLE ULTRA-LOW THRESHOLD VERTICAL-CAVITY SURFACE-EMITTING LASERS FOR USAF APPLICATIONS				5a. CONTRACT NUMBER In-house		
				5b. GRANT NUMBER		
				5c. PROGRAM ELEMENT NUMBER 61102F		
6. AUTHOR(S) Thomas R. Nelson, Jr., Ph.D.				5d. PROJECT NUMBER 2305		
				5e. TASK NUMBER DW		
				5f. WORK UNIT NUMBER 01		
7. PERFORMING ORGANIZATION NAME(S) AND ADDRESS(ES) Electron Devices Branch (AFRL/SNDD) Aerospace Components Division Sensors Directorate Air Force Research Laboratory, Air Force Materiel Command Wright-Patterson Air Force Base, OH 45433-7320				8. PERFORMING ORGANIZATION REPORT NUMBER AFRL-SN-WP-TR-2005-1039		
9. SPONSORING/MONITORING AGENCY NAME(S) AND ADDRESS(ES) Sensors Directorate Air Force Research Laboratory Air Force Materiel Command Wright-Patterson AFB, OH 45433-7320				10. SPONSORING/MONITORING AGENCY ACRONYM(S) AFRL/SNDD		
				11. SPONSORING/MONITORING AGENCY REPORT NUMBER(S) AFRL-SN-WP-TR-2005-1039		
12. DISTRIBUTION/AVAILABILITY STATEMENT Approved for public release; distribution is unlimited.						
13. SUPPLEMENTARY NOTES Report contains color.						
14. ABSTRACT This report summarizes research on the development of ultra-low threshold vertical-cavity surface-emitting lasers. This in-house lab task, supported by AFOSR under LRIR 2305DW01, was initiated by Dr. John Loehr, with AFOSR Program Manager Dr. Alan Craig. In 2001, Dr. Thomas Nelson became the in-house project lead on this effort, with AFOSR management transferred first to Dr. Kent Miller, and most recently to Dr. Gernot Pomrenke. This task was initiated in March 1996, and this report covers roughly the time period of March 1996 - December 2002.						
15. SUBJECT TERMS Vertical-cavity surface-emitting laser, optoelectronics, molecular beam epitaxy, semiconductors, finite element method, modeling and simulation, oxidation furnace						
16. SECURITY CLASSIFICATION OF:			17. LIMITATION OF ABSTRACT: SAR	18. NUMBER OF PAGES 108	19a. NAME OF RESPONSIBLE PERSON (Monitor) Dr. Thomas R. Nelson 19b. TELEPHONE NUMBER (Include Area Code) (937) 255-1874 x3361	
a. REPORT Unclassified	b. ABSTRACT Unclassified	c. THIS PAGE Unclassified				

# Ultra-Low Threshold Vertical-Cavity Surface-Emitting Lasers for USAF Applications

Thomas R. Nelson, Jr., PhD.  
*AFRL/SNDD, 2241 Avionics Circle,*  
*Wright Patterson AFB, OH 45419\**

(Dated: January 11, 2005.)

## Abstract

This report summarizes research on the development of ultra-low threshold vertical-cavity surface-emitting lasers. This in-house lab task, supported by AFOSR under LRIR 2305DW01, was initiated by Dr. John Loehr, with AFOSR Program Manager Dr. Alan Craig. In 2001, Dr. Thomas Nelson became the in-house project lead on this effort, with AFOSR management transferred first to Dr. Kent Miller, and most recently to Dr. Gernot Pomrenke. This task was initiated in March 1996, and this report covers roughly the time period of March 1996 - Dec 2002.

## INTRODUCTION: GOAL OF THIS RESEARCH

The goal of this Air Force Office of Scientific Research (AFOSR) sponsored in-house laboratory task has been the development of ultra-low threshold vertical-cavity surface emitting lasers (VCSELs) for USAF applications. Interest in VCSELs by the Air Force Research Laboratory (AFRL) Sensors Directorate, specifically from the Aerospace Components and Subsystems Concept Division, Electron Devices Branch (AFRL/SNDD) was in several areas:

- \* Low cost, short haul optical local area networks (LANS), with the vision of a "fly-by-fiber" approach to future aircraft systems.
- \* Phased arrays of VCSELs for potential laser radar (LADAR) applications.
- \* High speed optical components for implementation in radio-frequency to photonic links (RF/Photonic links) for cost effective information transmission of conventional RF radar signals.
- \* The development of photonic elements involved in optical true-time-delay systems, again for improving conventional RF radar systems by the use of optoelectronic subsystems.

In all of these efforts, several underlying goals were desirable. These include low-cost mass production methods, high-speed device operation, ease of integration onto existing or future platforms, and a robust device capable of withstanding the unique environments experienced by air and space craft.

At the time of the initiation of this in-house laboratory task, semiconductor optoelectronic devices, including laser diodes, were advancing from fundamental research concepts to advanced engineering projects for inclusion in photonic components and subsystems. Indeed, a few companies were emerging that for the first time were making vertical-cavity surface-emitting lasers (VCSELs) commercially available. Early emphasis was on high-bandwidth applications and developing arrays of such devices for transceiver modules in telecommunications systems. Such products were based on high-yield processes, not necessarily state-of-the-art optoelectronics fabrication methods designed at high-performance devices. Furthermore, as their usage was intended for terrestrial systems, overall power

consumption, heat dissipation, etc were not effects of enormous concern. On an aerospace platform, however, total power budget is a primary driving force in total system design, and the use of high efficiency components is mandatory. These concerns, among others, gave the ultra-low threshold focus to the effort summarized in this document.

In all the work detailed below, unless otherwise noted, the research was performed entirely “in-house.” To clarify, the effort started with theoretical device design based upon the work of AFRL/SNDD scientists, working in conjunction with the Air Force Institute of Technology (co-located at Wright-Patterson Air Force Base). Device material growth was accomplished by means of molecular beam epitaxy (MBE) using a *Varian GENII* MBE system owned by the Materials Directorate (AFRL/MLPSM). This growth system is located in the cleanroom of the Sensors Directorate, is operated by AFRL/MLPSM scientists, and many upgrades and modifications were made to this tool to improve its device growth capability as a direct result of the stringent growth requirements of this project. These will be detailed in later sections. Similarly, all device fabrication and characterization were also accomplished at AFRL/SNDD. One significant accomplishment as a result of this effort was the development of a steam oxidation furnace with in-situ oxidation monitoring, and its role in device fabrication will be explained in later sections.

## **BACKGROUND AND THEORY**

This project officially commenced in March 1996, under the guidance of in-house project leader Dr. John Loehr, and AFOSR program manager Dr. Alan Craig. The first goal was to determine exactly what type of VCSEL structure to pursue. An overview VCSEL taxonomy is presented in Fig. 1 showing the most common three varieties of such devices, namely the etched post VCSEL (Fig. 1A), the proton-implanted VCSEL (Fig. 1B), and the intra-cavity contacted VCSEL with native-oxide aperture layers (Fig. 1C). From these examples, several design issues are apparent: VCSELs can be completely monolithic in nature, with both top and bottom distributed Bragg reflector (DBR) mirrors formed from epitaxial growth (as in Fig. 1A and Fig. 1B), or partially monolithic using a combination of epitaxial (bottom mirror, Fig. 1C) and post-growth deposition (top mirror, Fig. 1C); VCSELs can have their current contacts formed outside the cavity by suitably doping the DBR mirrors (Fig. 1A and Fig. 1B), or via intra-cavity contacting (Fig. 1C); and there are

a variety of means for confining the optical field as well as the injected current via etched posts, proton implantation followed by annealing, native oxide apertures, or selective etching (not shown). In each case, significant tradeoffs exist. For instance, proton implanted devices without mesa isolation etching received the earliest commercial interest due to their relative ease of fabrication. Production of these devices requires extensive initial calibrations of the proton implant profile, however, not to mention the availability of an implantation system. Etched post structures provide better optical confinement, but the deep etching through the DBR mirrors required in these structures warrants exploring the relative benefits of wet versus dry etching, in addition to the potential need to passivate the sidewalls roughened by such etching to avoid surface recombination losses. Finally, the native-oxide aperture devices require not only the etched post techniques above, but also an apparatus (steam bubbler type system) running at sufficiently high temperature ( $T > 375^\circ\text{C}$ ) to convert high mole fraction  $\text{Al}_x\text{Ga}_{1-x}\text{As}$  ( $x \geq 0.95$ ) material into native oxides of aluminum.

In order to determine which structure to study, a program was initiated to develop a suite of modelling tools to allow us to compare the relative benefits of each structure. Much of the bandstructure code useful in determining laser gain as a function of injected carriers was already in place from previous research [1–3], and could readily be incorporated into this suite. More challenging, however, was the ability to model the optical “cold cavity” fields in structures such as the oxide-apertured etched-post designs. The goal in this design effort is the reduction (ideally, elimination) of threshold current, that is, carriers (electrons and holes) that recombine but do not contribute to lasing. In large area lasers (edge-emitting or VCSELs), the threshold current is proportional to the volume of the active region. In most designs, this active region consists of one or more quantum wells (QWs) separated by appropriate thickness barriers, and multiple sets of such wells and barriers are then grown at appropriate positions in the lasing cavity so as to have maximum spatial overlap with the intracavity lasing field mode. The use of both etched-post and oxide-apertured structures in early efforts demonstrated improvements in threshold current reduction, primarily by restricting and refining the transverse gain profile to overlap better with the optical field mode. However, worth noting is the fact that such lateral patterning also affects the transverse optical confinement factor. When the posts and/or apertures shrink to dimensions on the order of the lasing emission wavelength, three optical effects begin to emerge: (1) The spatial profile of each cavity mode changes from a plane wave to a 3-D waveguide type of

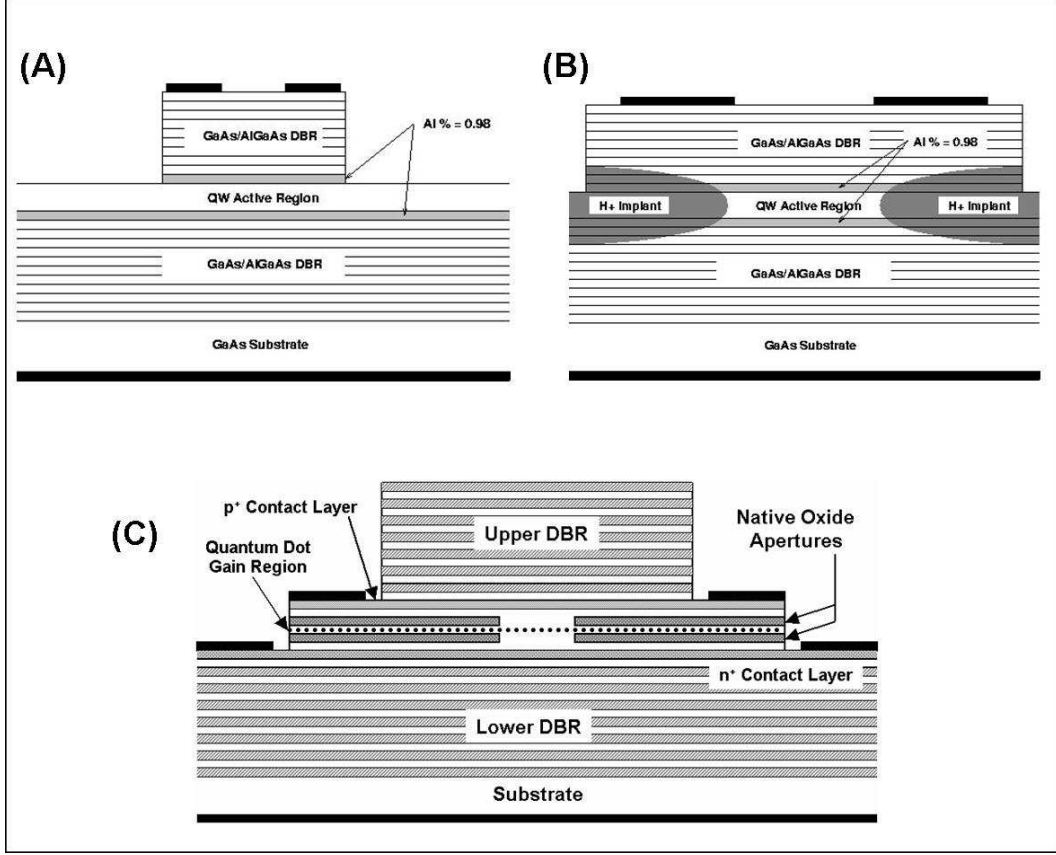


FIG. 1: Schematic cross sections of three common types of VCSELs. (A) An etched post structure, extra-cavity contacted, with oxide apertures (B) A proton implanted, extra-cavity contacted device. (C) An intra-cavity contacted device with oxide apertures, showing the possibility of top and bottom DBR mirrors formed from different methods (epitaxially grown bottom mirror, deposited top mirror).

mode; such a change then alters the modal reflectivity and the optical/active region overlap; (2) The boundaries of the oxide aperture or etched post begin to act as sources of diffraction losses, shedding optical radiation laterally from the device; (3) finally, the cavity lasing mode begins to blueshift in wavelength, with the spacing between modes increasing. All of these effects, then, play an important role in the effective design of low threshold lasers.

Previous efforts to simulate VCSEL cavity structures incorporating oxide apertures have varied significantly in their level of complexity and detail, in addition to their predicted results. Some groups suggested that thin oxides placed at field nodes provide the lowest threshold, while others argued that thick oxides at antinodes are the correct approach. The



disparity in answers is largely due to an incomplete understanding of the optical physics related to the aperture, or, more precisely, the aperture/cavity optical system. In an attempt to understand the physics, several models have been created, all with different approaches to the problem. However none of these models provide a comprehensive description of the optical fields, and no clear, consistent design guidance existed. In order to overcome these limitations, we embarked on efforts to develop methods for modelling lasing modes of various VCSEL structures.

Two sets of simulation codes were developed to aid in ultra-low threshold VCSEL design. The first of these, the *Weighted Index Method with Parasitics* (WIMP), is a semi-analytic hybrid vector-scalar code. As such, it was designed to be implemented on relatively standard computing platforms. Indeed, the source code that our group uses was written in *Visual Fortran* for the *Microsoft Windows* (XP, ME, or 9x) platforms, and it doesn't require unreasonably heavy duty computing power (large RAM or CPU requirements, for example). The only inflexible portions of the code at this point in time are the usage of bundled numerical library routines from the *International Mathematical and Statistical Libraries* (IMSL) suite of software codes. These library routines perform such functions as complex root finding, calculation of Bessel functions, and numerical integration and differentiation. Typical run times for problems seeking to find the first few roots of an oxide aperture VCSEL of typical dimensions (etched post of  $\approx 20\mu\text{m}$  diameter, oxide aperture diameter of  $\approx 5\mu\text{m}$ ) usually run less than 10 minutes on a Pentium 4 1-GHz CPU platform. Drawbacks and limitations of this method will be explained in the later section detailing simulation results.

The second method used for simulation of etched-post and oxide aperture VCSELs is the *Vector Finite Element Method* (VFEM). Unlike WIMP, this is a numerically intensive method due to the meshing of potentially hundreds of layers forming an oxide aperture VCSEL, and also due to the fact that the basis elements are *vector* and not *scalar* in nature. Indeed, as will be shown later, a set of 14 basis vector functions (6 node based, 6 edge based, and 2 face based) were chosen for this model. Physical RAM computing requirements dictated that these simulations be performed at the Major Shared Resources Center (MSRC), a high-performance computing center collocated at Wright Patterson AFB. For typical oxide-apertured or etched-post VCSEL structures, the RAM required was typically on the order of 1-3 GBytes. Present day high performance desktop stations, however, may be able to implement this code without undue strain. Even though this is a computationally intensive

method, this model has the distinct advantage that it calculates the *total* optical loss, including diffraction. As it is a model based on a variational solution of the vector Helmholtz equation, its results not only allow for direct calculation of lasing mode parameters, but also for deeper insight into the underlying physics associated with VCSEL design parameters.

In the sections that follow, these methods, as well as their applications (and limitations!) to VCSEL design will be detailed. Furthermore, a section that describes an analytic solution for the problem of graded interfaces between two slab media of constant refractive indices will also be presented. This solution is very applicable to low-threshold VCSEL structures, as much of the wasted power in driving such a device comes from trying to pass current through heterointerfaces. The use of material grading helps to overcome much of this waste, but subsequent optical design of the cavity is then complicated by these graded layers.

### **Weighted Index Method with Parasitics (WIMP)**

One goal of vertical cavity surface emitting laser (VCSEL) design is to reduce or even eliminate the threshold current. In relatively large devices, the threshold current is proportional to the volume of the electrically-pumped active region. Since the longitudinal dimension of this volume is fixed by the thickness of the active quantum wells, attention has focused on transverse current confinement. Both etched-post and oxide-apertured structures have been introduced in an effort to restrict the current path, and threshold currents have declined accordingly [4–6]. It is important to realize, however, that these lateral patterning techniques will also affect the transverse *optical* confinement. As the transverse dimensions shrink to the order of the lasing wavelength—about 1 micron—two optical microcavity effects emerge. First, the spatial profile of each cavity mode changes from a plane wave to a true three-dimensionally-confined waveguide mode. This change alters both the modal reflectivity of the DBR mirrors and the modal overlap with the active region (the transverse optical confinement factor). Second, the energy spacing between transverse modes increases sharply.

Both of these optical microcavity effects could significantly influence the VCSEL threshold current, either for good or ill. As the cavity shrinks, changes in the modal DBR reflectivity and the transverse optical confinement factor will modify the lasing mode threshold gain. If the threshold gain increases beyond the reach of the quantum wells, the structure will

not lase. Conversely, if the threshold gain remains relatively constant, microcavity VCSELs will lase, and the small cavity volume will result in a low threshold current. In this case, the second microcavity effect should act to reduce the threshold current even further: as the energy spacing between modes increases, fewer nonlasing modes exist within the gain bandwidth, and therefore fewer carriers recombine via nonlasing modes. These submicron VCSELs would lase at some of the lowest currents possible in semiconductor lasers, making them attractive for system applications. They would also exhibit a variety of quantum electrodynamic effects, making them attractive for basic laser research [7–9]. Since fabricating submicron VCSELs is difficult and expensive, it is desirable to prove the effort worthwhile by first calculating the lasing thresholds of these devices.

Unfortunately, the bound and radiative electromagnetic modes of both etched-post and oxide-apertured VCSEL cavities are extremely difficult to calculate. Brute-force numerical methods, such as finite-difference and finite-element, are more difficult in dielectric structures than in metal-clad waveguides since it is no longer possible to set selected field components equal to zero at the boundaries. Absorbing boundary conditions must be introduced or the structure must be placed inside a very large, perfectly-conducting enclosure. Furthermore, in lasing mode calculations we must solve for the threshold material gain in the active region, meaning that the dielectric profile of the structure itself is one of the unknowns. These structural unknowns are difficult to address using numerical techniques.

Often it is better to address problems with unknown structural parameters through analytic calculations, where the solutions are expanded in terms of an infinite set of special functions and the expansion coefficients are determined by boundary conditions. But this technique works well only when the refractive index profile separates in some preferred coordinate system, reducing the infinite expansions to a single term. If, as in realistic VCSEL structures, the refractive index profile does not separate in *any* coordinate system, then simple single-term special-function solutions to the governing partial differential equations do not represent exact solutions for the modes and analytic methods become quite cumbersome. Despite this difficulty, most previous analytic calculations have introduced, at some point in the treatment, a single product term to describe a particular electromagnetic field component [10, 11]. It is vital to realize that this is equivalent to assuming the underlying differential equation separates.

Since separable descriptions facilitate closed-form expressions, rapid calculation, and com-

parison with well-understood “textbook” problems, there is considerable motivation to improve and justify them. In this paper we generalize the weighted index method (WIM)—a separable approximation—to compute cavity modes in cylindrically-symmetric dielectric VCSEL structures. We calculate the electric and magnetic vector potentials and use these to compute the resulting fields. We also show, using the calculus of variations, that this technique provides the *best* separable solution to the scalar Helmholtz equation. The method allows us to approximate the spatial profile, optical confinement factor, resonant frequency, and threshold material gain of cavity modes in both oxide-apertured and etched-post VCSELs. The method explicitly considers complex media, allowing us to include free carrier losses. We start by summarizing the essential vector field equations needed to address VCSEL modes. Next we derive the WIM and outline its application to cylindrically-symmetric VCSEL structures. We then derive weighted boundary conditions needed to apply the method in piecewise-constant index profiles. Next, we outline the iterative procedure for solving the resulting equations. Finally we apply the method to oxide-apertured and etched-post VCSELs, computing field profiles, optical confinement factors, resonant wavelengths, and threshold material gains for several cavity modes. A summary of these results is then presented.

We want to find the electric  $\left(\vec{E}\right)$  and magnetic  $\left(\vec{H}\right)$  field profiles, the resonant wavelength  $(\lambda)$ , and the threshold material gain  $(g_{th})$  for each cavity mode in azimuthally-symmetric VCSEL structures. For this we must solve a vector-wave equation subject to appropriate boundary conditions at each interface. Because there are several equivalent electromagnetic descriptions of any system, we can write wave equations for the electric and magnetic fields, scalar potentials, or vector potentials. The most powerful and convenient method for this problem is to solve for the magnetic  $\left(\vec{A}\right)$  and electric  $\left(\vec{F}\right)$  vector potentials and use them to compute the fields. The steady-state, time-harmonic vector potentials  $\vec{A}$  and  $\vec{F}$  satisfy the three-dimensional vector Helmholtz equation (in Gaussian units)

$$\left\{\nabla^2 + \frac{\omega^2}{c^2}\varepsilon(\rho, z)\right\}\left\{\begin{array}{l}\vec{A}(\rho, \phi, z) \\ \vec{F}(\rho, \phi, z)\end{array}\right\} = 0. \quad (1)$$

Here  $\vec{A}$  and  $\vec{F}$  depend on time as  $e^{i\omega t}$ ,  $\omega = 2\pi c/\lambda$ , and we have assumed a cylindrically-symmetric, complex dielectric function  $\varepsilon$ . Note that

$$\sqrt{\varepsilon} = N \equiv n + i\kappa, \quad (2)$$

where  $N$  is the (complex) refractive index; material gain is incorporated by taking  $\kappa$  positive in the active region. We assume  $\mu = 1$  in all regions.

The power of the vector potential approach comes from the fact that we need only  $F_z$  to generate transverse electric (TE) modes and only  $A_z$  to generate transverse magnetic (TM) modes[12]. Since an arbitrary electromagnetic field can be represented as a superposition of TE and TM modes, we need only solve for the two unknown scalar functions  $A_z$  and  $F_z$ , a dramatic simplification over solving Eq. 1 for all six vector components. The electric and magnetic fields themselves may be computed directly from the  $z$  components of the vector potentials via [13]

$$\vec{E} = -\frac{ic}{\omega\epsilon}\nabla \times \nabla \times (\hat{z}A_z) - \nabla \times (\hat{z}F_z), \quad (3)$$

$$\vec{H} = \nabla \times (\hat{z}A_z) - \frac{ic}{\omega\mu}\nabla \times \nabla \times (\hat{z}F_z), \quad (4)$$

or, more explicitly,

$$E_\rho(\rho, z) = -\frac{ic}{\omega\epsilon}\frac{\partial^2}{\partial\rho\partial z}A_z(\rho, z) - \frac{1}{\rho}\frac{\partial}{\partial\phi}F_z(\rho, z), \quad (5)$$

$$E_\phi(\rho, z) = -\frac{ic}{\omega\epsilon\rho}\frac{\partial^2}{\partial\phi\partial z}A_z(\rho, z) + \frac{\partial}{\partial\rho}F_z(\rho, z), \quad (6)$$

$$E_z(\rho, z) = \frac{ic}{\omega\epsilon}\left\{\frac{\partial^2}{\partial\rho^2} + \frac{1}{\rho}\frac{\partial}{\partial\rho} - \frac{m^2}{\rho^2}\right\}A_z(\rho, z), \quad (7)$$

$$H_\rho(\rho, z) = \frac{1}{\rho}\frac{\partial}{\partial\phi}A_z(\rho, z) - \frac{ic}{\omega\mu}\frac{\partial^2}{\partial\rho\partial z}F_z(\rho, z), \quad (8)$$

$$H_\phi(\rho, z) = -\frac{\partial}{\partial\rho}A_z(\rho, z) - \frac{ic}{\omega\mu\rho}\frac{\partial^2}{\partial\phi\partial z}F_z(\rho, z), \quad (9)$$

$$H_z(\rho, z) = \frac{ic}{\omega\mu}\left\{\frac{\partial^2}{\partial\rho^2} + \frac{1}{\rho}\frac{\partial}{\partial\rho} - \frac{m^2}{\rho^2}\right\}F_z(\rho, z). \quad (10)$$

Since all solutions to Eq 1 are separable in the azimuthal coordinate  $\phi$ , depending on it as  $e^{im\phi}$ , the differential equation for  $A_z$  and  $F_z$  is quite simple. By expressing  $\vec{A}$  and  $\vec{F}$  in cylindrical coordinates and inserting the appropriate  $\phi$  dependence into Eq 1, we have

$$\left\{\frac{\partial^2}{\partial\rho^2} + \frac{1}{\rho}\frac{\partial}{\partial\rho} + \frac{\partial^2}{\partial z^2} + \left(\frac{\omega^2}{c^2}\epsilon(\rho, z) - \frac{m^2}{\rho^2}\right)\right\}\begin{Bmatrix} A_z(\rho, z) \\ F_z(\rho, z) \end{Bmatrix} = 0. \quad (11)$$

In separable geometries, the two-dimensional, azimuthally-symmetric scalar Helmholtz equation (11) may be solved exactly by separation of variables, yielding the potential profiles, resonant wavelength, and threshold material gain for each cavity mode. Realistic

VCSEL structures, however, are not separable, greatly complicating the solution of (11). An exact semianalytic solution could be obtained by expanding  $A_z$  and  $F_z$  in terms of the general solutions in each region, then matching boundary conditions to determine the (infinite) set of expansion coefficients. In practice this technique requires considerable care to implement, though it does have the advantage of incorporating non-separable behavior in the solutions [14]. Below, we present an alternative technique to generate the best *separable* approximations to (11).

Equation (11) represents two uncoupled partial differential equations—one each for  $A_z$  and  $F_z$ —which are quite difficult to solve. For separable geometries, we can exactly replace each equation in (11) with two independent ordinary differential equations, and these can be solved exactly. For non-separable geometries, we approximate the solutions to (11). In general, there are two possible approximation techniques. The most common approach is to maintain the exact equations (11) and construct an approximate *function* that “almost” solves them. An alternative approach is to replace the exact equations (11) with approximate *equations*, and solve these approximate equation exactly. We take the latter approach, and approximate each equation in (11) with two *coupled* ordinary differential equations. We accomplish this by extending the WIM—which was first developed to calculate waveguide modes in horizontal-cavity ridge-waveguide lasers [15, 16]—to address the eigenmodes of cylindrical cavities. This technique has the advantage of giving the *best* separable solution to (11) in the variational sense, and allows us to estimate the field profile, optical confinement factor, resonant wavelength, and threshold material gain of each cavity mode. Below we derive the WIM equations.

Proceeding as if separable solutions to (11) exist, we take

$$A_z(\rho, z) = P(\rho)Q(z), \tag{12}$$

$$F_z(\rho, z) = R(\rho)S(z).$$

Substituting either of these into (11) gives

$$\zeta''(\rho)\xi(z) + \frac{1}{\rho}\zeta'(\rho)\xi(z) + \zeta(\rho)\xi''(z) + \left(\frac{\omega^2}{c^2}\varepsilon(\rho, z) - \frac{m^2}{\rho^2}\right)\zeta(\rho)\xi(z) = 0, \tag{13}$$

where  $\zeta = P$  or  $R$  and  $\xi = Q$  or  $S$ . For each potential in (12), we can separate the resulting equation (13) by integrating it against  $\zeta^*(\rho)$  or  $\xi^*(z)$ . This procedure yields the

axial equation

$$\xi''(z) + (\beta_{eff}^\alpha(z))^2 \xi(z) = 0 \quad (14)$$

and the radial equation

$$\zeta''(\rho) + \frac{1}{\rho} \zeta'(\rho) + \left[ (k_{eff}^\alpha(\rho))^2 - \frac{m^2}{\rho^2} \right] \zeta(\rho) = 0 \quad (15)$$

for each potential. These axial and radial equations are *coupled* by the weighted axial and radial propagation constants, given respectively by

$$(\beta_{eff}^\alpha(z))^2 \equiv \frac{(\omega^2/c^2) \langle \zeta | \varepsilon(\rho, z) | \zeta \rangle + \langle \zeta | \zeta'' \rangle + \langle \zeta | \rho^{-1} | \zeta' \rangle - m^2 \langle \zeta | \rho^{-2} | \zeta \rangle}{\langle \zeta | \zeta \rangle} \quad (16)$$

and

$$(k_{eff}^\alpha(\rho))^2 \equiv \frac{(\omega^2/c^2) \langle \xi | \varepsilon(\rho, z) | \xi \rangle + \langle \xi | \xi'' \rangle}{\langle \xi | \xi \rangle}. \quad (17)$$

Here  $\langle | \rangle$  denotes an inner-product over  $z$  or  $\rho$ , respectively defined by

$$\langle A(z) | B(z) \rangle = \int_{-\infty}^{\infty} A^*(z) B(z) dz \quad (18)$$

and

$$\langle A(\rho) | B(\rho) \rangle = \int_0^{\infty} A^*(\rho) B(\rho) \rho d\rho. \quad (19)$$

Since the weighted propagation constants depend on whether we solve for  $A_z$  or  $F_z$ , we have introduced an additional superscript  $\alpha = \text{TE}$  or  $\text{TM}$  to distinguish between TE modes resulting from  $F_z$  (involving averages over  $\zeta = R$  and  $\xi = S$ ) and TM modes resulting from  $A_z$  (involving averages over  $\zeta = P$  and  $\xi = Q$ ). Coupling occurs only between the radial and axial equations for a given vector potential  $A_z$  or  $F_z$ : the two potentials remain uncoupled in (14) and (15). But  $A_z$  and  $F_z$  will be coupled later by *boundary conditions* when we solve for hybrid modes.

We must now find the solutions of (14) and (15) in piecewise-constant refractive index profiles, paying particular attention to the interfacial boundary conditions. A sample structure is shown in Fig. 2. Since we will work exclusively with piecewise-constant geometries, we simplify our notation by taking  $\varepsilon(\rho, z) \rightarrow \varepsilon_{i,j}$ , where  $i$  and  $j$  index the radial and axial regions, respectively. Thus we also have  $k_{eff}^\alpha(\rho) \rightarrow k_i^\alpha$  and  $\beta_{eff}^\alpha(z) \rightarrow \beta_j^\alpha$ , and (14) and (15) reduce, respectively, to the one-dimensional Helmholtz equation and Bessel's equation.

To solve these equations subject to the refractive index profile  $\varepsilon_{i,j}$  of etched-post or oxide-apertured VCSEL structures, we must supplement (14) and (15) with an appropriate

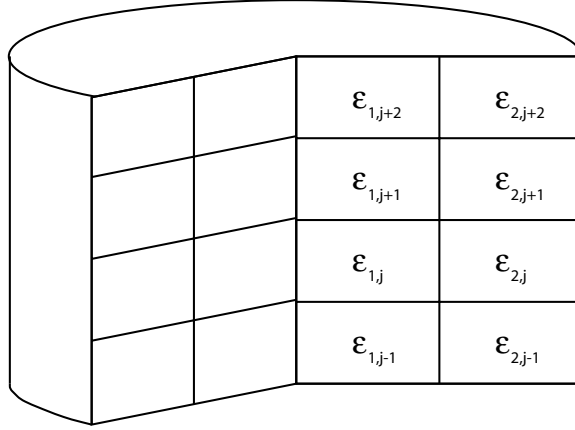


FIG. 2: Illustration of piecewise constant permittivity notation for an axially symmetric VCSEL.

set of interface and endpoint boundary conditions. The interfacial boundary conditions are the usual continuity requirements on the normal and tangential components of various electromagnetic fields. Therefore we cannot directly enforce boundary conditions on  $P$ ,  $Q$ ,  $R$ , and  $S$ , but must perform the intermediate step of computing the electric and magnetic fields via (5)–(10). Furthermore, since the underlying partial differential equations (11) do not separate, these boundary conditions cannot be satisfied at all points on the boundary surfaces—if they could, (11) would be separable.

In preparation for generating approximate boundary conditions, we rewrite the weighted index formulas (16) and (17). By integrating (15) against  $\zeta^*(\rho)$  we have

$$\langle \zeta | \zeta'' \rangle + \langle \zeta | \rho^{-1} | \zeta' \rangle - m^2 \langle \zeta | \rho^{-2} | \zeta \rangle = -\langle \zeta | (k_i^\alpha)^2 | \zeta \rangle, \quad (20)$$

allowing us to express (16) as

$$(\beta_j^\alpha)^2 = \frac{(\omega^2/c^2) \langle \zeta | \varepsilon_{i,j} | \zeta \rangle - \langle \zeta | (k_i^\alpha)^2 | \zeta \rangle}{\langle \zeta | \zeta \rangle} \equiv \frac{\omega^2}{c^2} \langle \varepsilon_{\zeta,j}^\alpha \rangle - \langle k^\alpha \rangle^2, \quad (21)$$

where

$$\langle \varepsilon_{\zeta,j}^\alpha \rangle \equiv \frac{\langle \zeta | \varepsilon_{i,j} | \zeta \rangle}{\langle \zeta | \zeta \rangle} \quad \text{and} \quad \langle k^\alpha \rangle \equiv \sqrt{\frac{\langle \zeta | (k_i^\alpha)^2 | \zeta \rangle}{\langle \zeta | \zeta \rangle}}. \quad (22)$$

Similarly, by integrating (14) against  $\xi^*(z)$  we find

$$\langle \xi | \xi'' \rangle = -\langle \xi | (\beta_j^\alpha)^2 | \xi \rangle, \quad (23)$$

allowing us to express (17) as

$$(k_i^\alpha)^2 = \frac{(\omega^2/c^2) \langle \xi | \varepsilon_{i,j} | \xi \rangle - \langle \xi | (\beta_j^\alpha)^2 | \xi \rangle}{\langle \xi | \xi \rangle} \equiv \frac{\omega^2}{c^2} \langle \varepsilon_{i,\xi}^\alpha \rangle - \langle \beta^\alpha \rangle^2, \quad (24)$$



where

$$\langle \varepsilon_{i,\xi}^\alpha \rangle \equiv \frac{\langle \xi | \varepsilon_{i,j} | \xi \rangle}{\langle \xi | \xi \rangle} \quad \text{and} \quad \langle \beta^\alpha \rangle \equiv \sqrt{\frac{\langle \xi | (\beta_j^\alpha)^2 | \xi \rangle}{\langle \xi | \xi \rangle}}. \quad (25)$$

The compact expressions (21) and (24) allow us to compute weighted variables without using the derivatives of  $\zeta$  and  $\xi$ .

We specialize these expressions to VCSEL lasing modes by truncating the inner product over  $z$ , replacing (18) with

$$\langle A(z) | B(z) \rangle = \int_{z_{\min}}^{z_{\max}} A^*(z) B(z) dz, \quad (26)$$

where  $z_{\min}$  and  $z_{\max}$  denote the lower and upper VCSEL boundary planes. This truncation is necessary to force (24) to converge and reflects the assumption that most of the energy is contained inside the VCSEL cavity. In contrast, we force the radial wavefunctions to decay evanescently to zero—to find guided modes—and the inner product defined by (19) presents no difficulty.

We now present boundary conditions and solutions for the axial and radial equations (14) and (15). Recall that the unknowns in this formalism are, for each mode, the functions  $P(\rho)$ ,  $Q(z)$ ,  $R(\rho)$ , and  $S(z)$ , the resonant frequency  $\omega$ , and the threshold material gain in the active region  $g_{th} \equiv 4\pi\kappa_{active}/\lambda$ .

We solve the axial equation (14) in piecewise constant geometries, such as in Fig. 3. The general solutions of (14) are given in each axial region  $[z_j, z_{j+1}]$  by

$$Q_j(z) = a_j^{TM} e^{i\beta_j^{TM} z} + b_j^{TM} e^{-i\beta_j^{TM} z}, \quad (27)$$

$$S_j(z) = a_j^{TE} e^{i\beta_j^{TE} z} + b_j^{TE} e^{-i\beta_j^{TE} z},$$

where we explicitly denote both the TE and TM solutions for clarity. Using the iterative solution procedure described below, we compute  $\beta_j^{TE}$  and  $\beta_j^{TM}$  from (21); assume for now that they are known constants. These solutions must be joined at each interface  $z_j$  by matching the tangential electric and magnetic fields. Inserting (12) into (5)–(10), we compute these

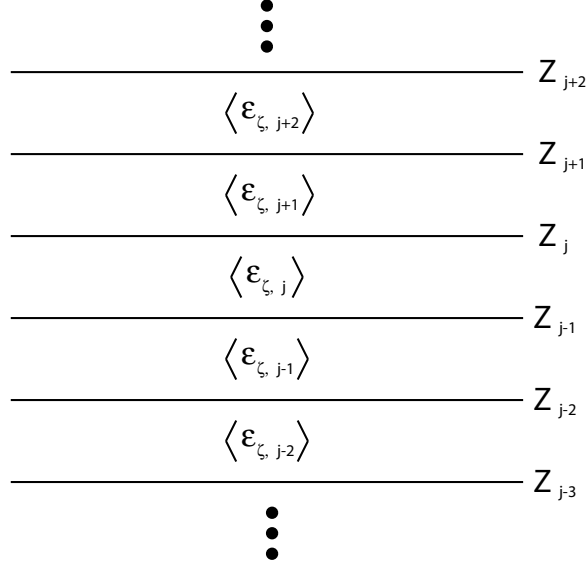


FIG. 3: Illustration of weighted permittivity profile for the WIM axial solution.

tangential field components as

$$E_\rho(\rho, z) = -\frac{ic}{\omega\epsilon}P'(\rho)Q'(z) - \frac{im}{\rho}R(\rho)S(z), \quad (28)$$

$$E_\phi(\rho, z) = \frac{cm}{\omega\epsilon\rho}P(\rho)Q'(z) + R'(\rho)S(z), \quad (29)$$

$$H_\rho(\rho, z) = \frac{im}{\rho}P(\rho)Q(z) - \frac{ic}{\omega\mu}R'(\rho)S'(z), \quad (30)$$

$$H_\phi(\rho, z) = -P'(\rho)Q(z) + \frac{cm}{\omega\mu\rho}R(\rho)S'(z). \quad (31)$$

We consider, in turn, two distinct cases:  $m = 0$  and  $m \neq 0$ .

When  $m = 0$  we can match boundary conditions with  $Q = 0$  (pure TE modes) or  $S = 0$  (pure TM modes). For these modes, it is sufficient to force just two tangential field components to be continuous: demanding continuity of the other two components gives redundant conditions. For TE modes we require  $E_\phi$  and  $H_\rho$  to be continuous; for TM modes we require  $E_\rho$  and  $H_\phi$  to be continuous. As we will see below, for pure TE and TM modes the fields themselves, and not just the vector potentials, are separable. This makes it easy to generate weighted boundary conditions for these modes.

For pure TE modes, we have

$$E_\phi(\rho, z) = R'(\rho)S(z), \quad (32)$$

$$H_\rho(\rho, z) = -\frac{ic}{\omega\mu}R'(\rho)S'(z). \quad (33)$$

Since we assume  $\mu = 1$  in all regions, both  $E_\phi$  and  $H_\rho$  depend on  $z$  only via  $S(z)$  and  $S'(z)$ , respectively. Therefore we can force both tangential fields to be continuous by setting  $S(z)$  and  $S'(z)$  continuous across each interface.

For pure TM modes, on the other hand, we have

$$E_\rho(\rho, z) = -\frac{ic}{\omega\varepsilon}P'(\rho)Q'(z), \quad (34)$$

$$H_\phi(\rho, z) = P'(\rho)Q(z). \quad (35)$$

Again, we can make  $H_\phi$  continuous by forcing  $Q(z)$  to be continuous across each interface. However,  $E_\rho$  depends on  $z$  through both  $Q'(z)$  and  $\varepsilon$ . Since  $\varepsilon$  is not a separable function of  $z$  and  $\rho$ , we must weight the relative permittivity to obtain average boundary conditions holding for all  $\rho$ . Therefore we require  $Q'(z)/\langle\varepsilon_P^{TM}\rangle$  to be continuous at each interface, where  $\langle\varepsilon_P^{TM}\rangle$  has already been defined in each region by (25). (We could also have generated average boundary conditions using  $\langle\frac{1}{\varepsilon}\rangle$ , but this approach gave inferior results.)

Inserting the functional forms (27) and applying the continuity conditions for either  $\alpha = \text{TE}$  or  $\alpha = \text{TM}$  modes, we relate  $a_j^\alpha, b_j^\alpha$  to  $a_{j+1}^\alpha, b_{j+1}^\alpha$  at each axial boundary  $z = z_j$  through the transfer matrices

$$L_j^\alpha \begin{bmatrix} a_j^\alpha \\ b_j^\alpha \end{bmatrix} = R_j^\alpha \begin{bmatrix} a_{j+1}^\alpha \\ b_{j+1}^\alpha \end{bmatrix}, \quad (36)$$

where

$$L_j^{TE} \equiv \begin{bmatrix} e^{i\beta_j^{TE}z_j} & e^{-i\beta_j^{TE}z_j} \\ i\beta_j^{TE}e^{i\beta_j^{TE}z_j} & -i\beta_j^{TE}e^{-i\beta_j^{TE}z_j} \end{bmatrix}, \quad R_j^{TE} \equiv \begin{bmatrix} e^{i\beta_{j+1}^{TE}z_j} & e^{-i\beta_{j+1}^{TE}z_j} \\ i\beta_{j+1}^{TE}e^{i\beta_{j+1}^{TE}z_j} & -i\beta_{j+1}^{TE}e^{-i\beta_{j+1}^{TE}z_j} \end{bmatrix}, \quad (37)$$

$$L_j^{TM} \equiv \begin{bmatrix} e^{i\beta_j^{TM}z_j} & e^{-i\beta_j^{TM}z_j} \\ \frac{i\beta_j^{TM}}{\langle\varepsilon_{P,j}^{TM}\rangle}e^{i\beta_j^{TM}z_j} & -\frac{i\beta_j^{TM}}{\langle\varepsilon_{P,j}^{TM}\rangle}e^{-i\beta_j^{TM}z_j} \end{bmatrix}, \quad R_j^{TM} \equiv \begin{bmatrix} e^{i\beta_{j+1}^{TM}z_j} & e^{-i\beta_{j+1}^{TM}z_j} \\ \frac{i\beta_{j+1}^{TM}}{\langle\varepsilon_{P,j+1}^{TM}\rangle}e^{i\beta_{j+1}^{TM}z_j} & -\frac{i\beta_{j+1}^{TM}}{\langle\varepsilon_{P,j+1}^{TM}\rangle}e^{-i\beta_{j+1}^{TM}z_j} \end{bmatrix}. \quad (38)$$

The composite transfer matrix  $[T^\alpha]$  for the whole system is formed by cascading the individual transfer matrices, giving

$$[T^\alpha] = [L_1^\alpha]^{-1}[R_1^\alpha][L_2^\alpha]^{-1}[R_2^\alpha][L_3^\alpha]^{-1}[R_3^\alpha] \cdots [L_{N-1}^\alpha]^{-1}[R_{N-1}^\alpha], \quad (39)$$

where  $N$  is the number of axial regions (including substrate and air) in the problem geometry. Thus we relate the unknown coefficients in the  $j = 1$  region (substrate) to the coefficients in the  $j = N$  region (air) via

$$\begin{bmatrix} a_1^\alpha \\ b_1^\alpha \end{bmatrix} = \begin{bmatrix} t_{11}^\alpha & t_{12}^\alpha \\ t_{21}^\alpha & t_{22}^\alpha \end{bmatrix} \begin{bmatrix} a_N^\alpha \\ b_N^\alpha \end{bmatrix}. \quad (40)$$

Since we are searching for axially-emitting (lasing) modes, we permit only outgoing radiation by setting

$$b_1^\alpha = a_N^\alpha = 0. \quad (41)$$

Finally, substituting (41) into (40) we obtain the axial threshold condition

$$t_{22}^\alpha(\omega, \kappa_{active}) = 0. \quad (42)$$

Setting the real and imaginary parts of  $t_{22}^\alpha$  equal to zero gives two independent equations that we solve to obtain the modal frequency  $\omega = 2\pi c/\lambda$  and threshold material gain  $g_{th} = 4\pi\kappa_{active}/\lambda$  for pure TE and TM modes. The expansion coefficients  $a_j^\alpha$  and  $b_j^\alpha$  for each region are found by back substitution through (40) and (36).

In order to generate sensible boundary conditions when  $m \neq 0$ , we must construct *hybrid* modes in which both  $S$  and  $Q$  nonzero. In this case *none* of the tangential fields are separable, since each has both TE and TM parts. Each TE and TM part is, in turn, a sum of *cylindrical wave* terms like  $e^{im\phi} J_m(k\rho) e^{i\beta z}$  ( $P$  and  $R$  will turn out to be Bessel functions). An exact solution would require us to include a superposition of cylindrical waves involving all values of  $k$ , and the boundary conditions would couple all terms at each interface. Fortunately, the coupling between cylindrical waves with different  $k$  is small enough to ignore [14, 17, 18]. Therefore we simultaneously and independently enforce the continuity of the TE and TM mode components of each tangential field, and our hybrid mode boundary conditions become the same as those for pure TE and TM modes.

We solve the radial equation (15) in piecewise constant geometries, such as in Fig. 4. The general solutions of (15) are given in each radial region  $[\rho_i, \rho_{i+1}]$  by

$$P_i(\rho) = \begin{cases} c_i^{TM} J_m(k_i^{TM} \rho) + d_i^{TM} Y_m(k_i^{TM} \rho) & i \neq M \\ c_M^{TM} K_m(ik_M^{TM} \rho) + d_M^{TM} I_m(ik_M^{TM} \rho) & i = M \end{cases}, \quad (43)$$

$$R_i(\rho) = \begin{cases} c_i^{TE} J_m(k_i^{TE} \rho) + d_i^{TE} Y_m(k_i^{TE} \rho) & i \neq M \\ c_M^{TE} K_m(ik_M^{TE} \rho) + d_M^{TE} I_m(ik_M^{TE} \rho) & i = M \end{cases},$$

where  $J_m$  and  $Y_m$  are  $m$ -th order Bessel functions of the first and second kind,  $I_m$  and  $K_m$  are modified  $m$ -th order Bessel functions of the first and second kind, and  $i = 1, 2, \dots, M$  indexes the inner to outer radial regions. Using the iterative solution procedure described later, we compute  $k_i^{TE}$  and  $k_i^{TM}$  from (24); assume for now that they are known constants.

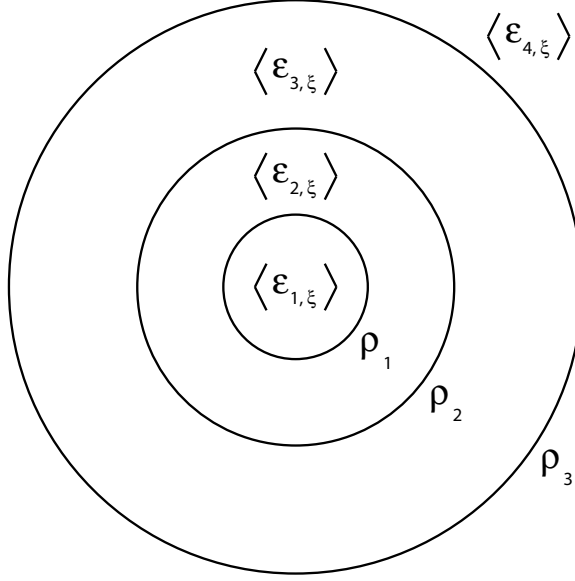


FIG. 4: Illustration of weighted permittivity profile for the WIM radial solution.

These solutions must be joined at each interface  $\rho_j$  by matching tangential electric and magnetic fields. Inserting (12) into (5)–(10) we compute these tangential field components as

$$E_z(\rho, z) = -\frac{ic}{\omega\epsilon} (k_i^{TM})^2 P(\rho)Q(z), \quad (44)$$

$$E_\phi(\rho, z) = \frac{cm}{\omega\epsilon\rho} P(\rho)Q'(z) + R'(\rho)S(z), \quad (45)$$

$$H_z(\rho, z) = -\frac{ic}{\omega\mu} (k_i^{TE})^2 R(\rho)S(z), \quad (46)$$

$$H_\phi(\rho, z) = -P'(\rho)Q(z) + \frac{cm}{\omega\mu\rho} R(\rho)S'(z). \quad (47)$$

We consider, in turn, the distinct cases  $m = 0$  and  $m \neq 0$ .

As in the axial problem, when  $m = 0$  we can match boundary conditions with  $P = 0$  (pure TE modes) or  $R = 0$  (pure TM modes), and it is sufficient to force just two tangential field components to be continuous. For TE modes we require  $E_\phi$  and  $H_z$  to be continuous; for TM modes we require  $E_z$  and  $H_\phi$  to be continuous. Following the same arguments as in the axial problem, we construct weighted boundary conditions to require the continuity of

$$(k_i^{TE})^2 R(\rho) \text{ and } R'(\rho) \text{ (for TE modes),} \quad (48)$$

$$\frac{(k_i^{TM})^2}{\langle \epsilon_Q^{TM} \rangle} P(\rho) \text{ and } P'(\rho) \text{ (for TM modes),} \quad (49)$$

at each radial interface  $\rho = \rho_i$ . To generate radial boundary conditions independent of  $z$ , we have replaced  $\varepsilon_{i,j}$  by the weighted permittivity  $\langle \varepsilon_{i,Q}^{TM} \rangle$  defined in (25).

Inserting the functional forms (43) and applying the continuity conditions for either  $\alpha =$  TE or TM modes, we relate  $c_i^\alpha, d_i^\alpha$  to  $c_{i+1}^\alpha, d_{i+1}^\alpha$  at each radial boundary  $\rho = \rho_i$  through the transfer matrices

$$A_i^\alpha \begin{bmatrix} c_i^\alpha \\ d_i^\alpha \end{bmatrix} = B_i^\alpha \begin{bmatrix} c_{i+1}^\alpha \\ d_{i+1}^\alpha \end{bmatrix}, \quad (50)$$

where

$$A_i^{TE} \equiv \begin{bmatrix} (k_i^{TE})^2 J_m(k_i^{TE} \rho_i) & (k_i^{TE})^2 Y_m(k_i^{TE} \rho_i) \\ k_i^{TE} J'_m(k_i^{TE} \rho_i) & k_i^{TE} Y'_m(k_i^{TE} \rho_i) \end{bmatrix}, \quad (51)$$

$$B_i^{TE} \equiv \begin{bmatrix} (k_{i+1}^{TE})^2 \Xi_m(\gamma k_{i+1}^{TE} \rho_i) & (k_{i+1}^{TE})^2 \Pi_m(\gamma k_{i+1}^{TE} \rho_i) \\ \gamma k_{i+1}^{TE} \Xi'_m(\gamma k_{i+1}^{TE} \rho_i) & \gamma k_{i+1}^{TE} \Pi'_m(\gamma k_{i+1}^{TE} \rho_i) \end{bmatrix}, \quad (52)$$

$$A_i^{TM} \equiv \begin{bmatrix} \frac{(k_i^{TM})^2}{\langle \varepsilon_{i,Q}^{TM} \rangle} J_m(k_i^{TM} \rho_i) & \frac{(k_i^{TM})^2}{\langle \varepsilon_{i,Q}^{TM} \rangle} Y_m(k_i^{TM} \rho_i) \\ k_i^{TM} J'_m(k_i^{TM} \rho_i) & k_i^{TM} Y'_m(k_i^{TM} \rho_i) \end{bmatrix}, \quad (53)$$

$$B_i^{TM} \equiv \begin{bmatrix} \frac{(k_{i+1}^{TM})^2}{\langle \varepsilon_{i+1,Q}^{TM} \rangle} \Xi_m(\gamma k_{i+1}^{TM} \rho_i) & \frac{(k_{i+1}^{TM})^2}{\langle \varepsilon_{i+1,Q}^{TM} \rangle} \Pi_m(\gamma k_{i+1}^{TM} \rho_i) \\ \gamma k_{i+1}^{TM} \Xi'_m(\gamma k_{i+1}^{TM} \rho_i) & \gamma k_{i+1}^{TM} \Pi'_m(\gamma k_{i+1}^{TM} \rho_i) \end{bmatrix}. \quad (54)$$

Here we have defined

$$\gamma = \begin{Bmatrix} 1 & \text{inner regions} \\ \sqrt{-1} & \text{outer region} \end{Bmatrix}, \quad \Xi_m = \begin{Bmatrix} J_m & \text{inner regions} \\ K_m & \text{outer region} \end{Bmatrix}, \quad \Pi_m = \begin{Bmatrix} Y_m & \text{inner regions} \\ I_m & \text{outer region} \end{Bmatrix}. \quad (55)$$

As in (39), we form a composite system matrix

$$[U^\alpha] \equiv [A_1^\alpha]^{-1} [B_1^\alpha] [A_2^\alpha]^{-1} [B_2^\alpha] [A_3^\alpha]^{-1} [B_3^\alpha] \cdots [A_{M-1}^\alpha]^{-1} [B_{M-1}^\alpha] \quad (56)$$

relating the unknown coefficients in the  $i = 1$  region (core) to the coefficients in the  $i = M$  region (cladding) via

$$\begin{bmatrix} c_1^\alpha \\ d_1^\alpha \end{bmatrix} = \begin{bmatrix} u_{11}^\alpha & u_{12}^\alpha \\ u_{21}^\alpha & u_{22}^\alpha \end{bmatrix} \begin{bmatrix} c_M^\alpha \\ d_M^\alpha \end{bmatrix}. \quad (57)$$

Since we are searching for longitudinally-propagating, laterally-confined VCSEL modes we force regularity at the origin and exponential decay as  $\rho \rightarrow \infty$  by setting

$$d_1^\alpha = d_M^\alpha = 0. \quad (58)$$

Finally, substituting (58) into (57) we obtain the radial threshold condition

$$u_{21}^\alpha(\omega, \kappa_{active}) = 0. \quad (59)$$

In order to generate sensible boundary conditions when  $m \neq 0$ , we must construct *hybrid* modes in which both  $R$  and  $P$  are nonzero. Again, none of the tangential field components are separable and it is impossible to match them for all  $z$  at a radial interface. Furthermore, if we mirror our axial treatment and independently force the TE and TM components to be continuous we generate an inconsistent boundary condition. For example, independently forcing  $E_z$  and the TM part of  $E_\phi$  to be continuous requires  $(k_i^{TM})^2 P(\rho)/\langle \varepsilon_Q^{TM} \rangle$  and  $P(\rho)/\langle \varepsilon_Q^{TM} \rangle$  be continuous at each interface. But this forces  $k_i^{TM}$  itself to be continuous, which is absurd. We cannot hope to work with TE and TM modes independently. Therefore we approximate our problem with an equivalent cylindrical dielectric waveguide problem, which admits analytic solutions for hybrid modes. These approximations are used *only* to generate boundary conditions, *not* as a substitution for the actual radial and axial solutions in each region.

Cylindrical waveguide modes depend on  $z$  as  $e^{i\beta z}$  or  $e^{-i\beta z}$ . Our fields, in contrast, depend on  $z$  via (27). There are two differences we must overcome. First, cylindrical waveguide modes are characterized by a *single* axial propagation constant  $\beta$ , whereas our fields have a different axial propagation constant  $\beta_j^a$  for each axial region and polarization. We can easily remedy this by replacing  $\beta_j^a$  with  $\langle \beta^\alpha \rangle$ , as defined in (25). Second, cylindrical waveguide modes depend on  $z$  as *either*  $e^{i\beta z}$  *or*  $e^{-i\beta z}$ . But even after replacing  $\beta_j^a$  with  $\langle \beta^\alpha \rangle$  our fields have a different linear combination of  $e^{i\langle \beta^\alpha \rangle z}$  and  $e^{-i\langle \beta^\alpha \rangle z}$  in each region, depending on the relative values of  $a_j^\alpha$  and  $b_j^\alpha$ . Therefore, for the purpose of constructing boundary conditions, we assume that the fields approximate a “pure” standing wave in the axial direction, with

$$a_j^{TE} = b_j^{TE} \text{ and } a_j^{TM} = -b_j^{TM}. \quad (60)$$

We assume further that  $a_j^{TE} \approx a_j^{TM}$ , and approximate the  $z$ -dependence of our fields as

$$\begin{aligned} \tilde{Q}(z) &\equiv \sin(\langle \beta^{TM} \rangle z), \\ \tilde{S}(z) &\equiv \cos(\langle \beta^{TE} \rangle z). \end{aligned} \quad (61)$$

Substituting (61) into (45) and (47), we approximate the  $\hat{\phi}$  field components as

$$\begin{aligned}\tilde{E}_\phi(\rho, z) &= \frac{cm}{\omega\langle\varepsilon_Q^{TM}\rangle\rho}P(\rho)\tilde{Q}'(z) + R'(\rho)\tilde{S}(z), \\ &\approx \left\{ \frac{cm\langle\beta^{TM}\rangle}{\omega\langle\varepsilon_Q^{TM}\rangle\rho}P(\rho) + R'(\rho) \right\} \cos(\langle\beta\rangle z)\end{aligned}\quad (62)$$

and

$$\begin{aligned}\tilde{H}_\phi(\rho, z) &= -P'(\rho)\tilde{Q}(z) + \frac{cm}{\omega\rho}R(\rho)\tilde{S}'(z), \\ &\approx \left\{ -P'(\rho) - \frac{cm\langle\beta^{TE}\rangle}{\omega\rho}R(\rho) \right\} \sin(\langle\beta\rangle z).\end{aligned}\quad (63)$$

Here we have replaced  $\varepsilon_{i,j}$  by the appropriate weighted value, and have selectively assumed  $\langle\beta^{TE}\rangle \approx \langle\beta^{TM}\rangle \approx \langle\beta\rangle$  to factor out the  $z$  dependence. Through *a-posteriori* comparison with our calculated results, we find all these assumptions well justified.

These approximate expressions for  $\tilde{E}_\phi$  and  $\tilde{H}_\phi$  are separable, as are expressions (44) and (46) for  $E_z$  and  $H_z$ . Therefore we can immediately construct suitable boundary conditions for radial hybrid modes by requiring the continuity of

$$\frac{(k_i^{TM})^2}{\langle\varepsilon_Q^{TM}\rangle}P(\rho), \quad (64)$$

$$(k_i^{TE})^2 R(\rho), \quad (65)$$

$$\frac{cm\langle\beta^{TM}\rangle}{\omega\langle\varepsilon_Q^{TM}\rangle\rho}P(\rho) + R'(\rho), \quad (66)$$

$$\text{and } P'(\rho) + \frac{cm\langle\beta^{TE}\rangle}{\omega\mu_0\rho}R(\rho). \quad (67)$$

By inserting the functional forms (43) and forcing all four of the above combinations to be continuous, we link the unknown coefficients at each radial interface  $\rho = \rho_i$  through the  $4 \times 4$  transfer matrix

$$A_i \begin{bmatrix} c_i^{TM} \\ d_i^{TM} \\ c_i^{TE} \\ d_i^{TE} \end{bmatrix} = B_i \begin{bmatrix} c_{i+1}^{TM} \\ d_{i+1}^{TM} \\ c_{i+1}^{TE} \\ d_{i+1}^{TE} \end{bmatrix}, \quad (68)$$



where

$$\begin{aligned}
A_i &\equiv \begin{bmatrix} \frac{(k_i^{TM})^2}{\langle \varepsilon_{i,Q}^{TM} \rangle} J_m(k_i^{TM} \rho_i) & \frac{(k_i^{TM})^2}{\langle \varepsilon_{i,Q}^{TM} \rangle} Y_m(k_i^{TM} \rho_i) & 0 & 0 \\ 0 & 0 & (k_i^{TE})^2 J_m(k_i^{TE} \rho_i) & (k_i^{TE})^2 Y_m(k_i^{TE} \rho_i) \\ \frac{cm\langle \beta^{TM} \rangle}{\omega\langle \varepsilon_{i,Q}^{TM} \rangle \rho} J_m(k_i^{TM} \rho_i) & \frac{cm\langle \beta^{TM} \rangle}{\omega\langle \varepsilon_{i,Q}^{TM} \rangle \rho} Y_m(k_i^{TM} \rho_i) & k_i^{TE} J'_m(k_i^{TE} \rho_i) & k_i^{TE} Y'_m(k_i^{TE} \rho_i) \\ k_i^{TM} J'_m(k_i^{TM} \rho_i) & k_i^{TM} Y'_m(k_i^{TM} \rho_i) & \frac{cm\langle \beta^{TE} \rangle}{\omega \rho} J_m(k_i^{TE} \rho_i) & \frac{cm\langle \beta^{TE} \rangle}{\omega \rho} Y_m(k_i^{TE} \rho_i) \end{bmatrix}, \\
B_i &\equiv \begin{bmatrix} \frac{(k_{i+1}^{TM})^2}{\langle \varepsilon_{i+1,Q}^{TM} \rangle} \Xi_m(\gamma k_{i+1}^{TM} \rho_i) & \frac{(k_{i+1}^{TM})^2}{\langle \varepsilon_{i+1,Q}^{TM} \rangle} \Pi_m(\gamma k_{i+1}^{TM} \rho_i) & 0 & 0 \\ 0 & 0 & (k_{i+1}^{TE})^2 \Xi_m(\gamma k_{i+1}^{TE} \rho_i) & (k_{i+1}^{TE})^2 \Pi_m(\gamma k_{i+1}^{TE} \rho_i) \\ \frac{cm\langle \beta^{TM} \rangle}{\omega\langle \varepsilon_{i+1,Q}^{TM} \rangle \rho_i} \Xi_m(\gamma k_{i+1}^{TM} \rho_i) & \frac{cm\langle \beta^{TM} \rangle}{\omega\langle \varepsilon_{i+1,Q}^{TM} \rangle \rho_i} \Pi_m(\gamma k_{i+1}^{TM} \rho_i) & \gamma k_{i+1}^{TE} \Xi'_m(\gamma k_{i+1}^{TE} \rho_i) & \gamma k_{i+1}^{TE} \Pi'_m(\gamma k_{i+1}^{TE} \rho_i) \\ \gamma k_{i+1}^{TM} \Xi'_m(\gamma k_{i+1}^{TM} \rho_i) & \gamma k_{i+1}^{TM} \Pi'_m(\gamma k_{i+1}^{TM} \rho_i) & \frac{cm\langle \beta^{TE} \rangle}{\omega \rho_i} \Xi_m(\gamma k_{i+1}^{TE} \rho_i) & \frac{cm\langle \beta^{TE} \rangle}{\omega \rho_i} \Pi_m(\gamma k_{i+1}^{TE} \rho_i) \end{bmatrix}.
\end{aligned} \tag{69}$$

$$\tag{70}$$

These matrices are mathematically equivalent to those for a cylindrical dielectric waveguide.

Cascading the interface transfer matrices, we again derive a composite system transfer matrix

$$\begin{bmatrix} c_1^{TM} \\ d_1^{TM} \\ c_1^{TE} \\ d_1^{TE} \end{bmatrix} = \begin{bmatrix} u_{11} & u_{12} & u_{13} & u_{14} \\ u_{21} & u_{22} & u_{23} & u_{24} \\ u_{31} & u_{32} & u_{33} & u_{34} \\ u_{41} & u_{42} & u_{43} & u_{44} \end{bmatrix} \begin{bmatrix} c_M^{TM} \\ d_M^{TM} \\ c_M^{TE} \\ d_M^{TE} \end{bmatrix} \tag{71}$$

relating the innermost and outermost radial coefficients. The endpoint boundary conditions (58) remain valid. Applying them to (71) and demanding nontrivial solutions gives the hybrid threshold condition

$$\begin{vmatrix} u_{21}(\omega, \kappa_{active}) & u_{23}(\omega, \kappa_{active}) \\ u_{41}(\omega, \kappa_{active}) & u_{43}(\omega, \kappa_{active}) \end{vmatrix} = 0, \tag{72}$$

which we solve in the complex plane for  $\omega$  and  $\kappa_{active}$ .

We compute the longitudinal and transverse mode spectrum by self-consistently solving the radial and axial problems. The modes are specified by the longitudinal mode number, the transverse mode number, and the azimuthal mode number  $m$ . Different longitudinal modes correspond to successive roots of the axial threshold condition (42), while different transverse modes correspond to successive roots of the radial threshold conditions (59) (for TE/TM modes) or (72) (for hybrid modes). The energy spacing between longitudinal modes is much greater than that between transverse modes. If we let  $n$  denote a generalized mode

index corresponding to a particular TE, TM, or hybrid mode, then the explicit unknowns for each mode are the vector potential functions  $P_n(\rho)$ ,  $Q_n(z)$  and/or  $R_n(\rho)$ ,  $S_n(z)$ , the optical mode frequency  $\omega_n$ , and threshold values for  $(\kappa_{active})_n$ . We iteratively solve the axial and radial problems as follows.

First we focus attention on a particular family of modes by fixing  $m$ : for  $m = 0$  we can compute TE or TM modes, while for  $m > 0$  only hybrid modes are possible. Then we solve the axial problem, taking the effective indices equal to the corresponding values for  $\varepsilon_{r1,j}$  in the innermost radial region: this solution corresponds to the standard plane-wave calculation appropriate for large-area devices. The ordered roots of the axial threshold condition (42) yield initial approximations  $Q_{n_0}(z)$  and/or  $S_{n_0}(z)$ ,  $\omega_{n_0}^{(axial)}$ , and  $(\kappa_{active}^{(axial)})_{n_0}$  for the mode  $n_0$  of interest. For VCSEL lasing mode calculations we are only interested in the first root of (42), corresponding to the fundamental longitudinal mode. We next compute the  $k_i^\alpha$  by inserting  $Q_{n_0}(z)$  and/or  $S_{n_0}(z)$  into (24), giving us enough information to address the radial problem. Depending on whether we are solving for TE, TM or hybrid modes, we then compute the roots of the radial threshold condition (59) or (72), yielding approximations for  $P_{n_0}(\rho)$  and/or  $R_{n_0}(\rho)$ ,  $\omega_{n_0}^{(radial)}$ , and  $(\kappa_{active}^{(radial)})_{n_0}$ : successive roots correspond to progressively higher-order transverse modes. Then we alternate between solving the axial and radial problems, always updating  $\beta_j^\alpha$  and  $k_i^\alpha$  by inserting the most recent wavefunctions into (21) or (24) as appropriate. In this way we generate a self-consistent solution to the coupled WIM equations (14) and (15), terminating when

$$\begin{aligned}\omega_{n_0}^{(axial)} &= \omega_{n_0}^{(radial)}, \\ (\kappa_{active}^{(axial)})_{n_0} &= (\kappa_{active}^{(radial)})_{n_0}\end{aligned}$$

to within prescribed tolerance. The procedure converges quite rapidly, allowing us to solve for a large number of cavity modes.

Finally, we note that the character of the modes found depends on both the differential equations and on the endpoint boundary conditions enforced. The original application of the WIM to rectangular waveguide geometries assumed propagating behavior in the  $\hat{z}$  direction and evanescent decay in the  $\hat{x}$  and  $\hat{y}$  directions. These endpoint conditions resulted in a standard eigenvalue problem, with the longitudinal propagation constant  $\beta$  being the eigenvalue. In this case, the Rayleigh-Ritz variational principle asserts that the resulting approximation of  $\beta$  will be more accurate than the wavefunctions themselves. In our application, we have

enforced evanescent decay in the radial direction and have permitted only *outward* propagating waves in the  $\hat{z}$  direction. This constrains the mode frequency  $\omega$  and the threshold material gain  $\kappa$ , as opposed to the propagation constant  $\beta$ , and these unknown parameters no longer appear as eigenvalues. Therefore the Rayleigh-Ritz principle has nothing to say about the relative accuracy of  $\omega$  and  $\kappa$ . Nevertheless, general variational principles dictate that we have found the best separable solution, and therefore we expect the resulting values for  $\omega$  and  $\kappa$  to be reasonably accurate. Note that we could also have solved for *radial* lasing modes by requiring evanescent decay in the axial direction and outward radial propagation, though these would be difficult to approximate because of the infinite radial inner product. In fact, as the cavity radius shrinks we *do* see evidence of radial propagation, as discussed in the next section.

Using the methods described above, we calculate lasing modes in etched-post [19, 20] and oxide-apertured [5, 21] devices fabricated from a  $\lambda = 980$  nm,  $1.5\lambda$ -cavity VCSEL. The VCSEL reflectors consist of a 17.5 period p-type GaAs/Al<sub>0.92</sub>Ga<sub>0.08</sub>As top Distributed Bragg Reflector (DBR) for the oxide-apertured structure, and a 4 period GaAs/Al<sub>x</sub>O top DBR with a  $\lambda/4$  p<sup>+</sup> GaAs contact layer for the post geometry. The bottom reflector in both structures is a 22 period n-type GaAs/Al<sub>0.92</sub>Ga<sub>0.08</sub>As DBR. The  $1.5\lambda$ -cavity is step-tapered with (intrinsic) layers of Al<sub>0.98</sub>Ga<sub>0.02</sub>As, Al<sub>0.65</sub>Ga<sub>0.35</sub>As, Al<sub>0.30</sub>Ga<sub>0.70</sub>As, and GaAs, culminating in a single In<sub>0.2</sub>Ga<sub>0.8</sub>As quantum well. Both structures are grown on a GaAs substrate. The etched-post structure, illustrated in Fig. 5, is formed by etching the top GaAs/AlAs DBR down to the  $\lambda/4$  GaAs contact layer, then oxidizing the AlAs layers. The oxide-apertured structure, illustrated in Fig. 6, is formed by oxidizing the  $\lambda/4$  Al<sub>0.98</sub>Ga<sub>0.02</sub>As layers in the cavity. We model each region as a cylindrically-symmetric layer of constant refractive index, assuming the material parameters in Table I. Free carrier losses are incorporated by taking  $\kappa_{i,j}$  negative. Material gain is incorporated by taking  $\kappa_{active}$  positive in the active quantum well region.

The lowest frequency, or fundamental, VCSEL lasing mode is analogous to the HEM<sub>11</sub> (or HE<sub>11</sub>) hybrid waveguide mode. Here the first and second subscripts refer respectively to the azimuthal ( $m$ ) and radial mode numbers. The HEM<sub>11</sub> mode is the most plane-wave like of all the propagating bound modes, despite containing both  $E_z$  and  $H_z$  [22, 23]. It is also the only waveguide mode having a radial intensity distribution with a maximum at the center. Following this terminology, we refer to the next higher-order VCSEL modes as

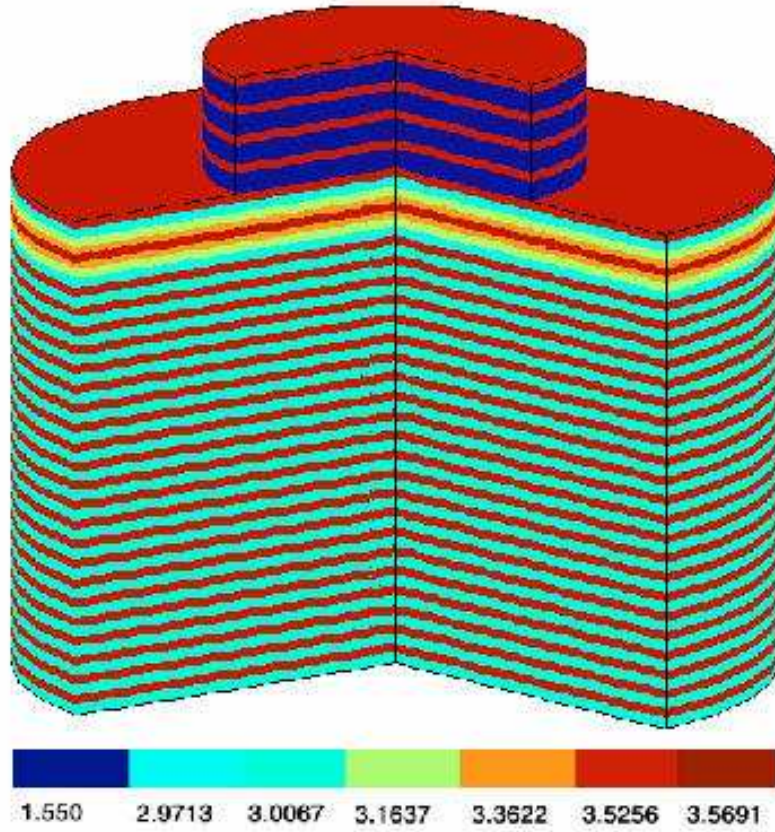


FIG. 5: Quasi-3D plot of the etched-post VCSEL index profile.

HEM<sub>21</sub>, TE<sub>01</sub>, and TM<sub>01</sub> modes: these modes make up the degenerate LP<sub>11</sub> mode under the “linear polarization” approximation [23]. All three of these modes feature a radial intensity profile with a null at the center.

In Figs. 7 and 8 we plot the longitudinal field profile for sample etched-post and oxide-apertured VCSELs. For the oxide-apertured structure, the top DBR is very long and the fields penetrate deeply into the top DBR. Therefore the large index difference between the semiconductor cavity and surrounding oxide is heavily weighted in (25), giving a large discontinuity in  $\langle \varepsilon_{\xi}^{\alpha} \rangle$  between the inner and outer radial regions. As a result, the fields

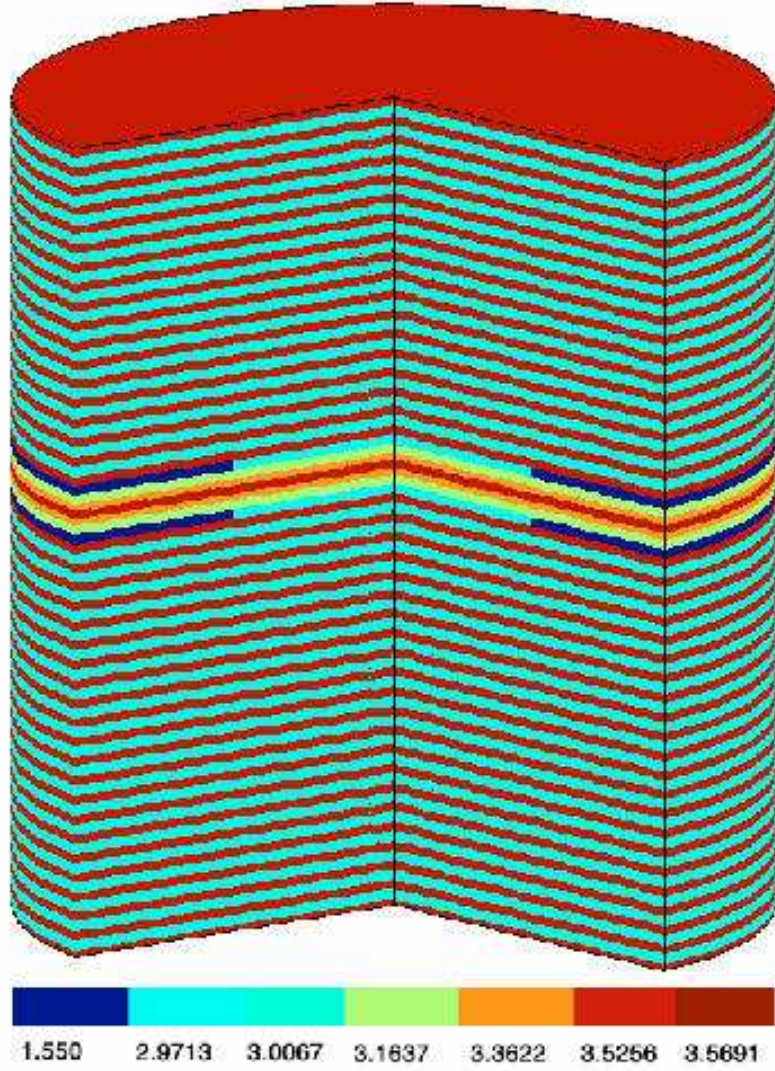


FIG. 6: Quasi-3D plot of the oxide-apertured VCSEL index profile.

within the oxide-aperture VCSEL are tightly confined to the core. In contrast, for the etched-post structure the large index contrast between top DBR layers allows very little field penetration, resulting in a smaller effective index difference and a correspondingly less confined field. In both structures, the fundamental mode is more confined than higher-order modes, and smaller VCSELs exhibit less confinement than larger ones. These effects can also be seen in the three-dimensional field intensity, given by [24]

$$I = \frac{1}{4} \left[ \varepsilon \left| \vec{E} \right|^2 + \mu \left| \vec{H} \right|^2 \right], \quad (73)$$

which we plot in Figs. 9-10. The radial discontinuity in these figures is a measure of the

TABLE I: Material Parameters used for WIM Simulations

Material	Index	Doping ( $10^{18} \text{ cm}^{-3}$ )	Loss ( $\text{cm}^{-1}$ )
$\text{In}_{0.2}\text{Ga}_{0.8}\text{As}$	3.5691	none	N/A
$\text{GaAs}$	3.5256	none	N/A
$\text{Al}_{0.3}\text{Ga}_{0.7}\text{As}$	3.3622	none	N/A
$\text{Al}_{0.65}\text{Ga}_{0.35}\text{As}$	3.1637	none	N/A
$\text{Al}_{0.98}\text{Ga}_{0.02}\text{As}$	2.9713	none	N/A
$\text{Al}_x\text{O}$	1.55	none	N/A
n-GaAs	3.5256	2	10
n- $\text{Al}_{0.92}\text{Ga}_{0.08}\text{As}$	3.0067	2	10
p-GaAs	3.5256	1	11.5
p- $\text{Al}_{0.92}\text{Ga}_{0.08}\text{As}$	3.0067	1	11.5
$\text{p}^+$ -GaAs	3.5256	5	57.5

error in our solution. This error stems from our separable approximation.

The transverse confinement factor  $\Gamma_t$  is usually defined as

$$\Gamma_t = \frac{\int_{\text{active}} |E|^2 ds}{\int |E|^2 ds}, \quad (74)$$

where the integral in the numerator is over the transverse extent of the active region and the integral in the denominator is over the entire transverse extent of the field. Figure 11 shows estimates of the transverse confinement factor for the first two modes of the etched-post and oxide-apertured VCSELs as a function of cavity radius. The estimates are generated from (74), using  $E = E(\rho) \rightarrow \tilde{E}_\phi(\rho)$  for TE modes (see (62)) and  $E \rightarrow \tilde{H}_\phi(\rho)$  for TM modes (see (63)); for hybrid modes we use both  $\tilde{E}_\phi(\rho)$  and  $\tilde{H}_\phi(\rho)$  and average the results. We use the effective  $\phi$  components since they are already averaged over  $z$  and are representative of the total field intensity profile. As the cavity radius decreases, more of the field intensity leaks out of the active region and the confinement factors drop monotonically. This behavior becomes more pronounced for higher-order modes, as illustrated in Fig. 12. Our oxide-apertured devices confine the optical mode more strongly to the active region and have higher transverse confinement factors than our etched-post structures. But the larger rate of change in confine-

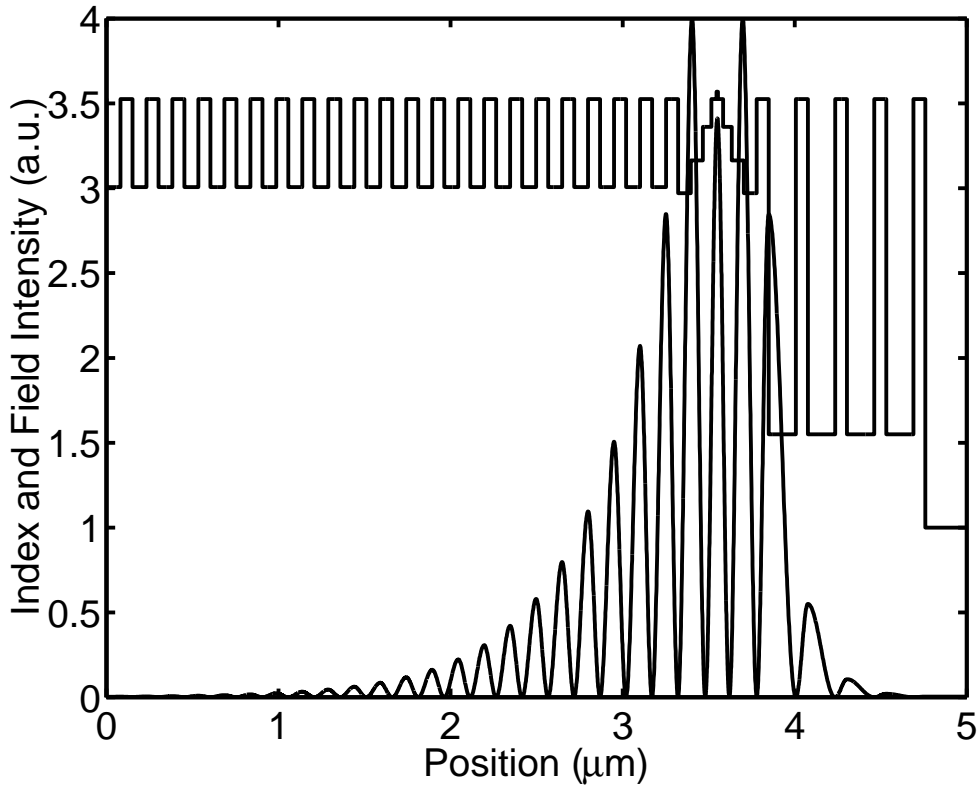


FIG. 7: Index and standing intensity profile along the axial direction for a  $1.4 \mu m$  radius etched-post VCSEL.

ment factor for the etched-post VCSEL, as shown in 11, yields better modal discrimination via  $\Gamma_t$ . For example, a  $1 \mu m$  radius device has  $\Delta\Gamma_t \equiv \Gamma_t(\text{HEM11}) - \Gamma_t(\text{TE01}) = 0.0759$  for the etched-post VCSEL, compared to only 0.0379 for the oxide-apertured VCSEL. This illustrates the effectiveness of employing a small radial index difference to introduce mode selective losses and enhance single mode lasing [25].

In Figs. 13 and 14 we plot the resonant wavelengths as a function of cavity radius for various modes in etched-post and oxide-apertured structures. The resonant wavelength blue-shifts as the oxide or post diameter shrinks, a dramatic departure from plane-wave results. This wavelength shift can be easily explained by examining the weighted dispersion relations (21) and (24), both of which take the functional form

$$\langle k_\rho^2 \rangle + \langle \beta_z^2 \rangle = \frac{\omega^2}{c^2} \langle \epsilon \rangle. \quad (75)$$

Although both  $\langle k_\rho^2 \rangle$  and  $\langle \beta_z^2 \rangle$  change slightly as the radius shrinks,  $\langle \beta_z^2 \rangle$  remains very close

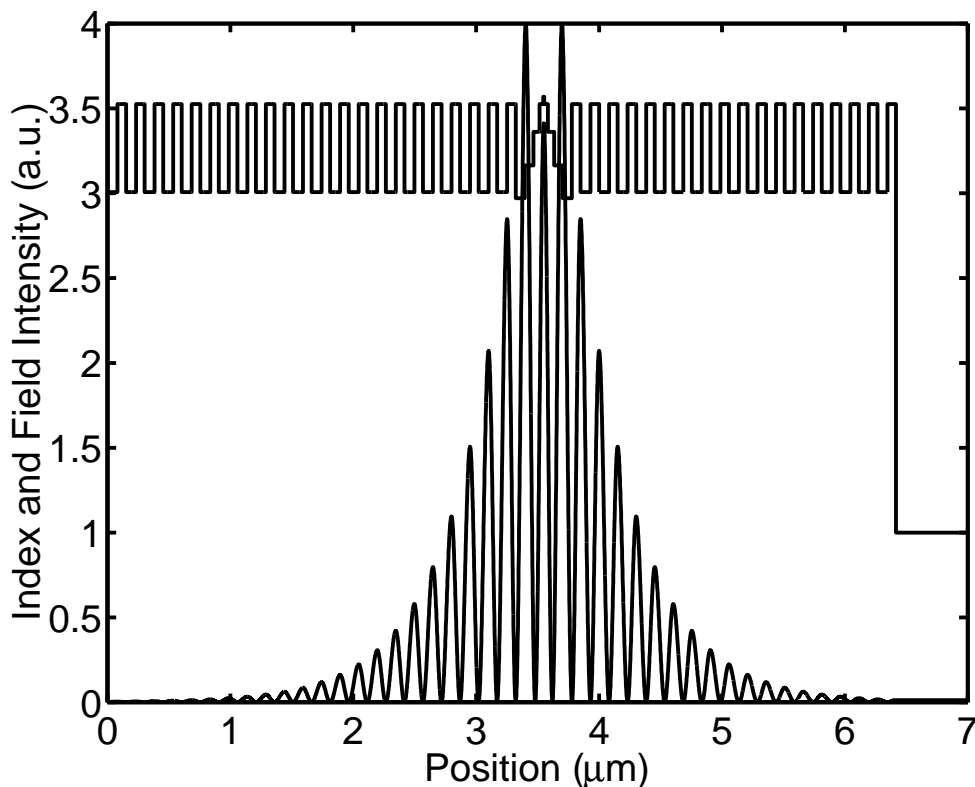


FIG. 8: Index and standing intensity profile along the axial direction for a  $1.4 \mu m$  radius oxide-apertured VCSEL.

to its plane-wave value. Therefore, as  $\langle k_\rho^2 \rangle$  increases from its plane-wave value of zero,  $\omega$  increases, leading to the blue shift illustrated in Figs. 13 and 14. This effect has been previously estimated using simpler approximations [26], but the self-consistent WIM results should be more accurate. To construct low-threshold microcavity VCSELs, the quantum well emission peak must be matched to the blue-shifted cavity resonance of the desired lasing mode.

The resonant wavelength changes more quickly with radius in oxide-apertured VCSELs as compared with the etched-post structures. This occurs because the oxide-apertured device exhibits a larger difference in effective index between the inner and outer radial regions, resulting in a larger field confinement and a correspondingly larger value for  $\langle k_\rho^2 \rangle$  in the waveguide core. As a result, the oxide-apertured structure provides more spectral discrimination between the VCSEL resonant modes. For example, in a  $1 \mu m$  VCSEL  $\Delta\lambda \equiv$



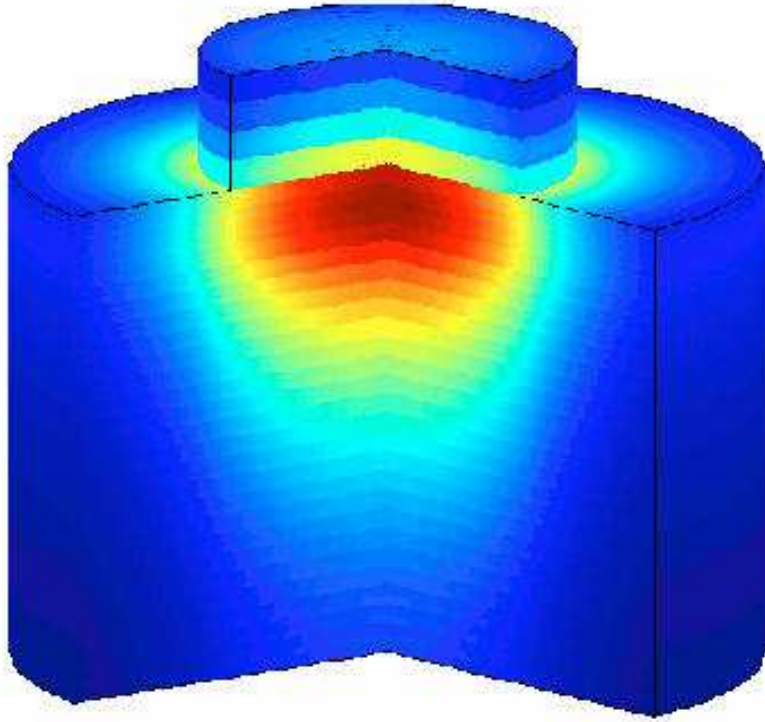


FIG. 9: HEM11 mode standing field intensity for a  $1.4 \mu m$  radius etched-post VCSEL. The field intensity on the top surface is amplified in order to illustrate the emitted mode.

$\lambda(\text{HEM}_{11}) - \lambda(\text{TE}_{01}) = 68.9 \text{ \AA}$  for the oxide-apertured structure as compared to  $59.8 \text{ \AA}$  for the etched-post. This effect might be exploited by tailoring the spontaneous emission of these devices to create lower threshold, higher efficiency devices.

Finally, we plot the components of the quasi-degenerate  $\text{LP}_{11}$  mode in Figure 15. The results show a small, but non-zero, splitting of the mode for aperture radii  $< \approx 0.85 \mu m$ , indicating where the LP mode approximation breaks down.

Within the WIM framework, we approximate the VCSEL cavity *modes* as superpositions

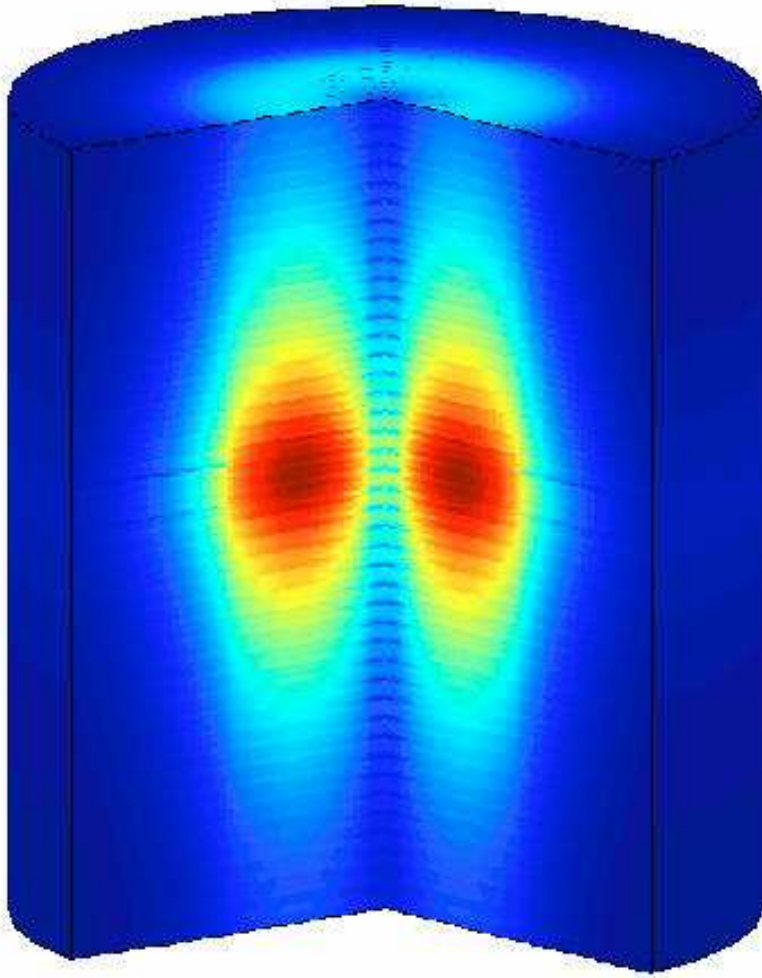


FIG. 10: TE01 mode standing field intensity for a  $1.4 \mu m$  radius oxide-apertured VCSEL. The field intensity of the top surface is amplified in order to illustrate the emitted mode.

of cylindrical *waves*. Each of these, in turn, can be viewed as a superposition of TE and TM *plane* waves propagating at an angle

$$\langle \theta \rangle = \arctan \left( \frac{\langle k_\rho \rangle}{\langle \beta_z \rangle} \right) \quad (76)$$

to the  $z$  axis. As the cavity radius decreases, the effective transverse propagation constant  $\langle k_\rho \rangle$  increases for all modes and, consequently, the average angle of incidence for the component plane waves impinging on each DBR interface increases. The power reflectivity for TE waves increases monotonically with angle until the total internal reflection angle is reached,

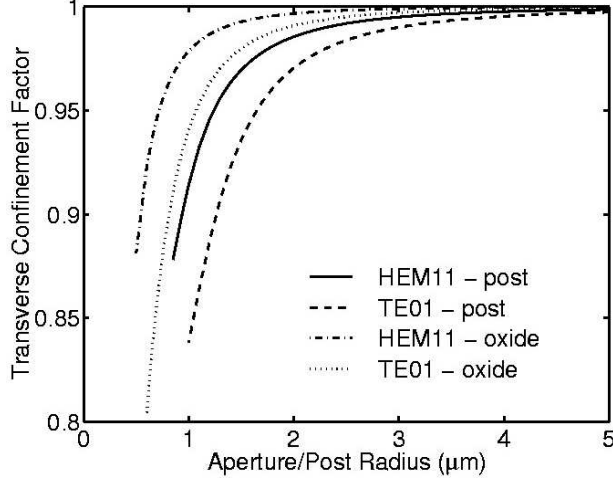


FIG. 11: Transverse confinement factor for the first two modes of the etched-post and oxide-apertured VCSEL.

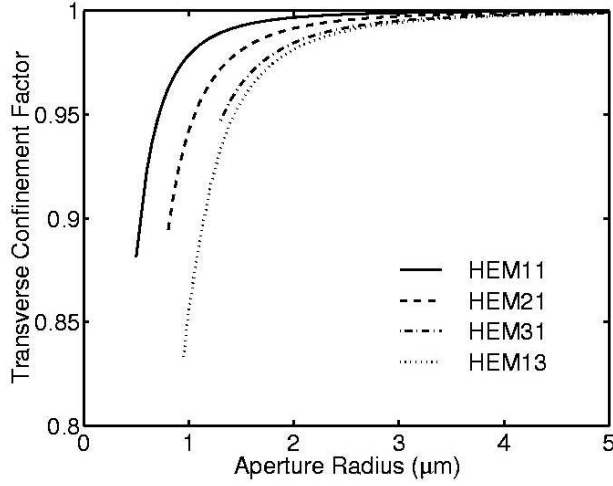


FIG. 12: Transverse confinement factor for the fundamental, and a few sample higher order modes for the oxide-apertured VCSEL.

while the power reflectivity for TM waves decreases monotonically until the Brewster angle is reached [27]. As a result, the TE wave components encounter *more* reflective DBR mirrors as the cavity radius shrinks, while the TM wave components encounter *less* reflective DBRs: Fig. 16 illustrates this behavior for the oxide-apertured structure. Therefore the TE wave components require less threshold material gain, the TM wave components more, and the

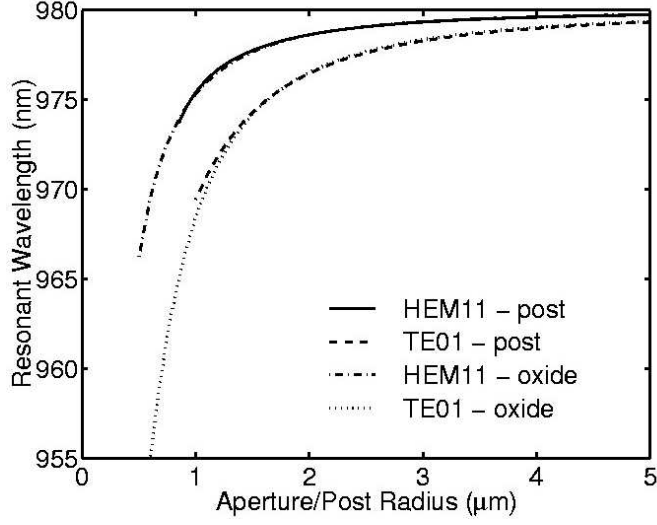


FIG. 13: Resonant wavelength for the first two modes of the etched-post and oxide-apertured VCSEL.

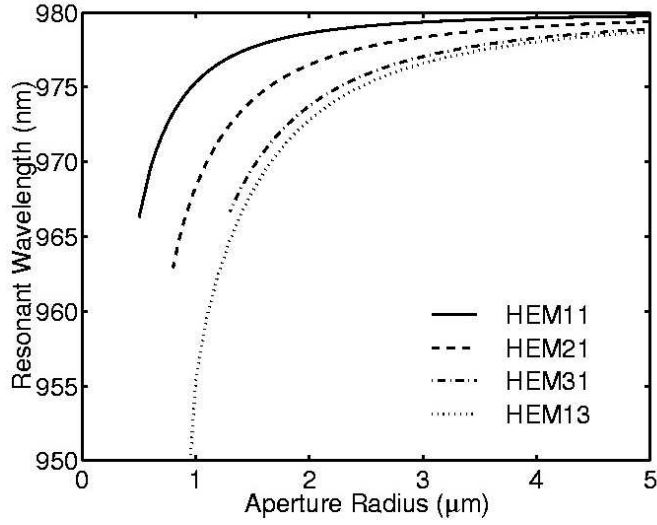


FIG. 14: Resonant wavelength for the fundamental, and a few sample higher order modes for the oxide-apertured VCSEL.

threshold gain for pure TE VCSEL *modes* decreases with cavity radius, while the threshold gain for TM modes increases.

HEM modes contain both TE and TM wave components, approximately canceling out the changing reflectivity effects. All of these trends are evident in Figs. 17-18, which show

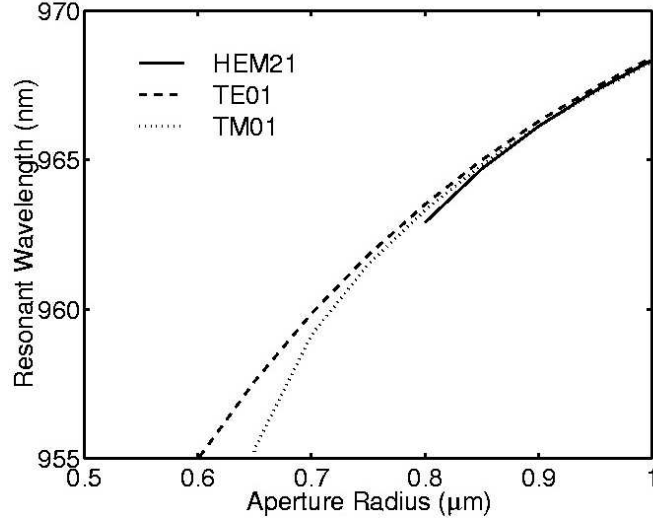


FIG. 15: Resonant wavelength for the components of the quasi-degenerate LP11 mode, illustrating the point at which the degeneracy is broken.

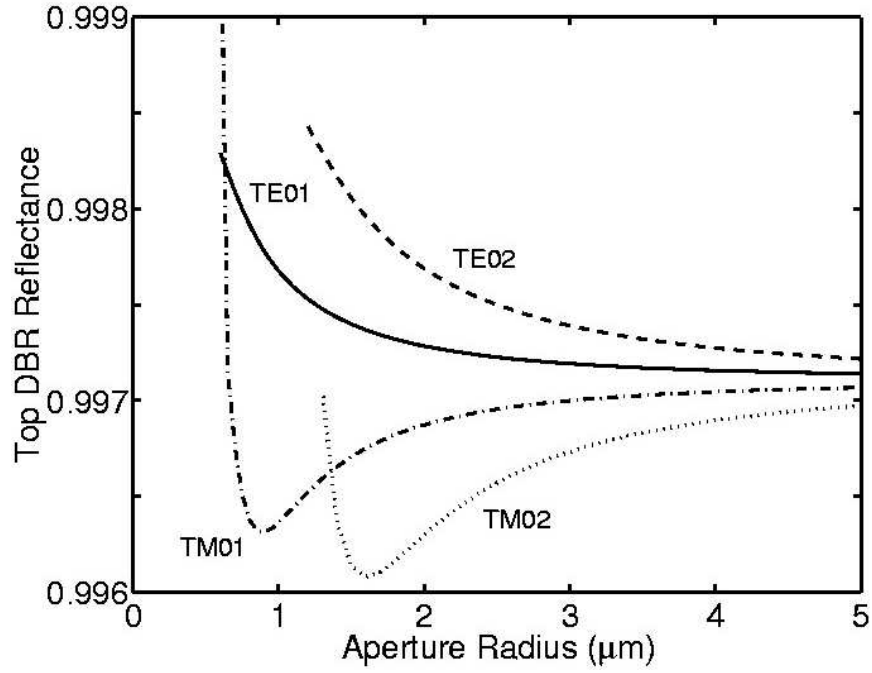


FIG. 16: Top DBR reflectance for the TE and TM modes of the oxide-apertured VCSEL.

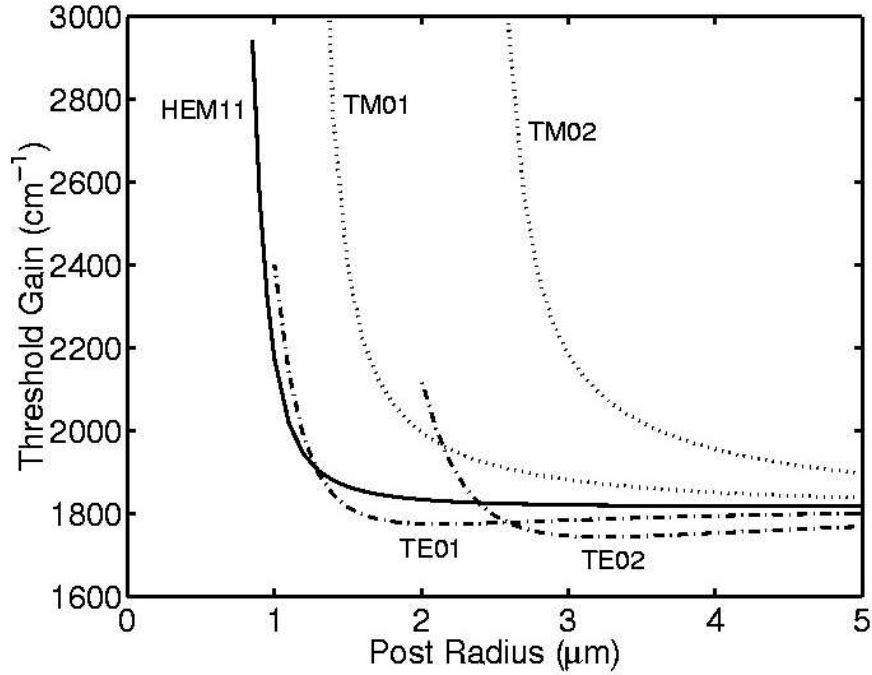


FIG. 17: Threshold gain for the fundamental, and transverse electric and magnetic modes for the etched-post VCSEL.

the threshold material gain  $g_{th} \equiv 4\pi\kappa_{active}/\lambda$  for the fundamental and several higher order VCSEL transverse modes. These results agree with prior in-plane laser studies that show a higher facet reflectance for TE than TM modes and a similar propagation constant ( $\beta$ ) for both TE and TM modes [17, 28–30]. For both VCSELs and in-plane lasers, these trends in mirror reflectivity and the associated lasing threshold become more pronounced for higher-order TE modes.

Based on the above arguments, we expect the TE mode thresholds to decrease monotonically with cavity radius and the TM and HEM thresholds to increase monotonically. The TM and HEM modes generally behave as expected in Figs. 17 and 19, but the TE mode thresholds increase abruptly below a critical cavity radius. This increase results from a different effect—the loss of mode confinement as the cavity shrinks. Recall that the transverse confinement factor  $\Gamma_t$  determines the strength of the coupling between a given cavity mode and the active quantum well, and that  $\Gamma_t$  decreases monotonically with cavity radius for all modes. As  $\Gamma_t$  decreases, the material gain must increase accordingly for the cavity mode to reach threshold. At fairly large cavity radii this effect is dominated by the change in DBR

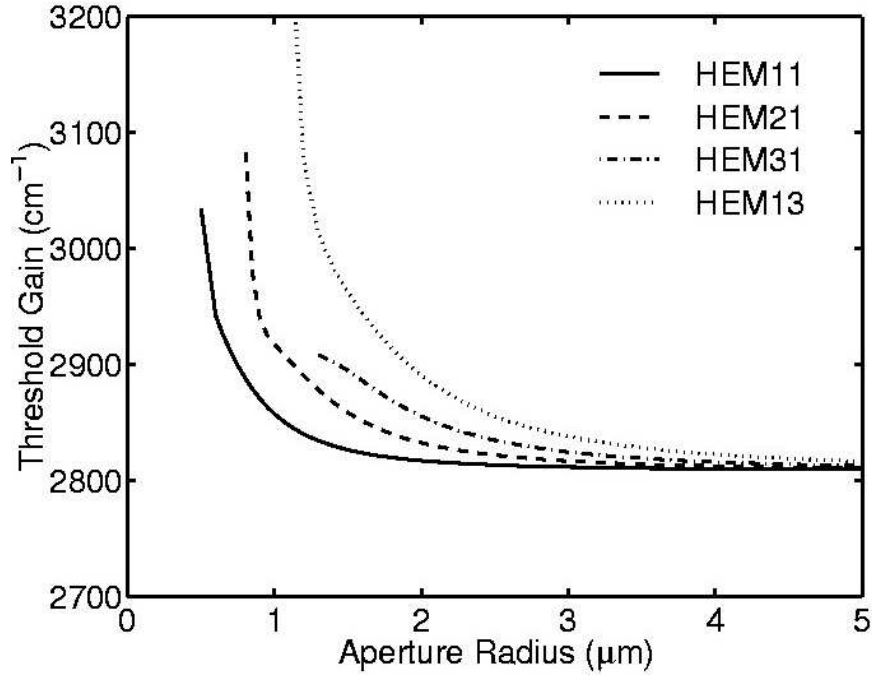


FIG. 18: Theshold gain for the fundamental, and a few sample higher order hybrid modes for the oxide-apertured VCSEL.

reflectivity, and the TE mode thresholds continue to decrease with cavity radius. But below a critical cavity radius the modal confinement effect dominates, and the quantum well gain must increase sharply for the cavity mode to reach threshold. Eventually the transverse confinement becomes so weak that the cavity cannot support a radially-bound mode at all. The radii at which our curves terminate in Figs. 17-18 indicate this “minimum” cavity size for each optical mode. This size effect has been previously estimated by simpler calculations [26], but the WIM values should be more accurate. Since our oxide-apertured structure confines the fields better than the etched-post structure, it supports bound modes at smaller cavity radii.

To summarize the WIMP formalism, we have presented an extremely general and rapid technique for estimating the spatial profile, optical confinement factor, resonant frequency, and threshold material gain of lasing modes in cylindrically-symmetric VCSEL geometries. Variational principles dictate that this method will generate the best solution over the space of all separable functions. We also expect, on variational grounds, that the “eigenvalues” corresponding to each mode—the resonant frequency and threshold gain—will be more ac-

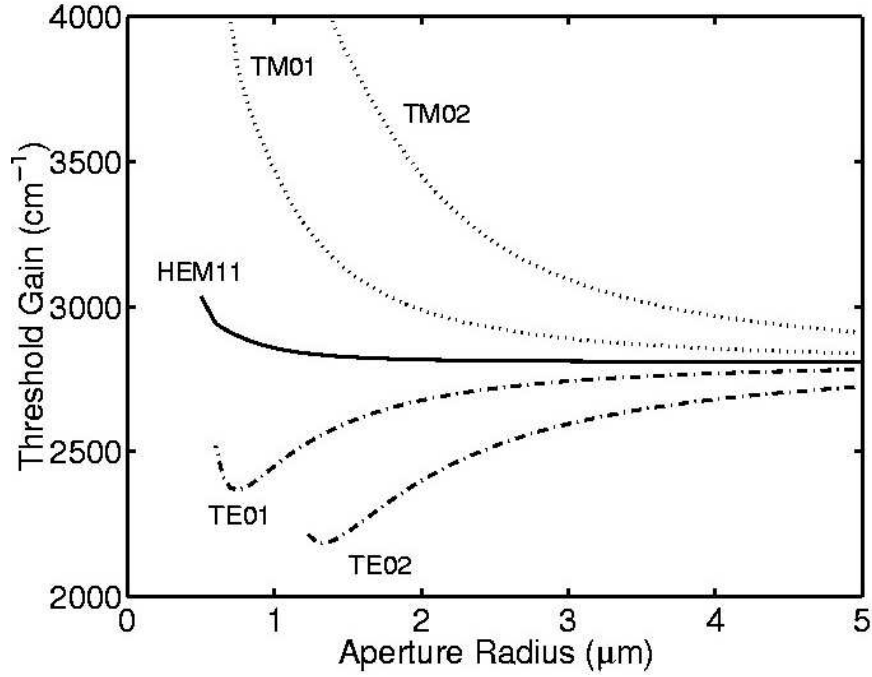


FIG. 19: Theshold gain for the fundamental, and transverse electric and magnetic modes for the oxide-apertured VCSEL.

curate than the wavefunction itself. Thus, among separable or single-term approximations to the lasing modes this method should yield the best possible results. The fundamental limitation to this technique is the base assumption of separability. Therefore non-separable effects, such as mode divergence and possible parasitic diffraction losses, are not addressed.

We have applied the technique to oxide-apertured and etched-post VCSELs, predicting a blue-shift of the lasing wavelength as the cavity radius shrinks. It is essential to incorporate this blue shift when designing the optical cavity, since the lasing resonance must line up precisely with the quantum well gain peak in order to minimize the threshold current. Our calculations suggest that quantum well emission should be tuned to the first TE mode cavity resonance, since this mode exhibits a *decreasing* threshold gain as the cavity radius shrinks. However, below a critical cavity radius the threshold gain increases rapidly and lasing becomes impossible. Our model can be used to investigate a variety of cavity designs in an effort to minimize this critical radius, and thereby minimize the VCSEL threshold current. In order to actually calculate this threshold *current*, it will be necessary to merge this model with quantum well gain and emission models.



The WIMP simulation source code, along with bandstructure source code for quantum well gain calculations and associated source code for predicting threshold currents as a function of oxide aperture diameter and other relevant device parameters, was transferred to *CFD Research Corporation (CFDRC)*, of Huntsville, Alabama. The vehicle for this technology transfer was a Cooperative Research and Development Agreement (CRADA), formalized by signatures from both parties in October, 2000. Under this agreement, AFRL/SND obtained in return a licensed set of *CFDRC*'s bundled suite of simulation tools for semiconductor devices (electrical, thermal, and optical modelling, as well as some MEMS capability). Since this time, *CFDRC* was acquired by *ESI Group* on January 28, 2004. At the time of this writing, many issues regarding customer support, *DARPA* commitments, and other responsibilities of *CFDRC* were still being settled as a result of this merger. The *ESI Group* is headquartered in Paris, with U.S. offices Huntsville, San Diego, and Columbia, Maryland.

### Vector Finite Element Method (VFEM)

In this section, we present a *quasi-exact* finite element method (FEM) model for analyzing the optical modes of microcavity VCSELs. This model, like the WIMP code describe in the previous section, is also based on a variational solution of the vector Helmholtz equation in microcavity geometries. The results of this model not only allow for direct calculation of lasing mode parameters, but also a better understanding of the underlying physics associated with VCSEL oxides.

To begin, we want to find the electric ( $\vec{E}$ ) and magnetic ( $\vec{H}$ ) field profiles, the resonant wavelength ( $\lambda_0$ ), and the threshold gain ( $g_{th}$ ) for each cavity mode in azimuthally-symmetric VCSEL structures. For this we must solve Maxwell's equations subject to appropriate boundary conditions at each material interface. The steady-state, time-harmonic electric field satisfies the vector Helmholtz equation (in MKS units)

$$\nabla \times \frac{1}{\mu_r} \nabla \times \vec{E} - k_0^2 \epsilon_r \vec{E} = -i\omega \mu_0 \vec{J}, \quad (77)$$

where  $\vec{E}$ ,  $\vec{H}$ , and the electric current  $\vec{J}$  depend on time as  $e^{i\omega t}$  ( $\omega = 2\pi c/\lambda$ );  $\epsilon_0$ ,  $\mu_0$ , and  $k_0$  are the free space permittivity, permeability, and propagation constant, respectively. It can be shown [31] that a weak solution to (77) may be obtained by *extremizing* the functional

$$\begin{aligned} \mathbb{J}(\vec{E}) = & \iiint_{\Omega} \frac{1}{\mu_r} (\nabla \times \vec{E}) \cdot (\nabla \times \vec{E}) dv - k_0^2 \iiint_{\Omega} \varepsilon_r \vec{E} \cdot \vec{E} dv \\ & + i\omega\mu_0 \iint_{\Gamma} (\hat{n} \times \vec{E}) \cdot \vec{H} ds + \iiint_{\Omega} \vec{E} \cdot \vec{J} dv. \end{aligned} \quad (78)$$

(By extremize, we mean forcing  $\delta \mathbb{J} = 0$ , where  $\delta$  is the variational operator.) Here  $\Omega$  and  $\Gamma$  are the problem domain and boundary, respectively. For azimuthally-symmetric structures, the material parameters ( $\mu_r$  and  $\varepsilon_r$ ) are functions of  $\rho$  and  $z$  only, and we may separate out the  $\phi$  dependence in (78) by assuming

$$E_{\phi} \sim \cos(m\phi), \quad (79)$$

and

$$E_{\rho}, E_z \sim \sin(m\phi), \quad (80)$$

where  $m$  is the azimuthal mode number. For integer  $m$ , the integrals over  $\phi = [0, 2\pi]$  yield a constant factor which may be ignored, effectively reducing the dimension of the problem from three to two. In addition, since different azimuthal modes are orthogonal, we may deal with each value of  $m$  independently.

For lasing mode analysis, we set the source current  $\vec{J}$  to zero, making (77) a source-free eigenmode problem. By assuming perfect conducting boundary conditions ( $\hat{n} \cdot \vec{E} = 0$ ) on  $\Gamma$ , which we justify later, the surface integral in (78) drops out and we are left with

$$\mathbb{J}(\vec{E}) = \iint_{\Omega} \frac{1}{\mu_r} (\nabla \times \vec{E}) \cdot (\nabla \times \vec{E}) dv - k_0^2 \iint_{\Omega} \varepsilon_r \vec{E} \cdot \vec{E} dv. \quad (81)$$

Here  $\Omega$  represents the two-dimensional domain (of the VCSEL) over the  $\rho - z$  plane. Our task is then to find the  $\vec{E}$  field which extremizes (81). That is, we must find the  $\vec{E}$  that satisfies

$$\iint_{\Omega} \frac{1}{\mu_r} (\nabla \times \vec{E}) \cdot (\nabla \times \delta \vec{E}) dv - k_0^2 \iint_{\Omega} \varepsilon_r \vec{E} \cdot \delta \vec{E} dv = 0, \quad (82)$$

for all field variations  $\delta \vec{E}$ . Equation (82) is a generalized eigenvalue problem,

$$\mathcal{S}(\vec{E}) - \xi \mathcal{T}(\vec{E}) = 0. \quad (83)$$

The  $\mathcal{S}$  and  $\mathcal{T}$  operators are defined by

$$\mathcal{S}(\vec{\Psi}) \equiv \iint_{\Omega} \frac{1}{\mu_r} (\nabla \times \vec{\Psi}) \cdot (\nabla \times \delta \vec{\Psi}) dv, \quad (84)$$

and

$$\mathcal{T}(\vec{\Psi}) \equiv \iint_{\Omega} \varepsilon_r \vec{\Psi} \cdot \delta \vec{\Psi} \, dv. \quad (85)$$

The eigenvalue  $\xi$  is defined as

$$\xi \equiv k_0^2 = \frac{\omega^2}{c^2}. \quad (86)$$

All the desired mode information may be found by solving (82). For each mode, the eigenvalue is the square of the (generally complex) free-space propagation constant, which is related to the modal wavelength ( $\lambda_0$ ) (98) and the total optical loss or threshold gain ( $g_{th}$ ) (102). The eigenvectors are simply the time-harmonic (vector) electric fields ( $\vec{E}$ ). We approximate the solution to (82) using the finite element method.

The formalism developed thus far is general and could apply to any of several variational approaches to solving Maxwell's equations. We now narrow our attention to the finite element method (FEM). In the finite element method, the solution to (82) is approximated by limiting the space of admissible functions  $\vec{E}$  to the linear superposition of a finite set of basis functions (generally characterized by the fact that they are non-zero only over a subdomain  $\Omega_e$ , the domain of mesh element  $e$ ). In our vector FEM, we expand the fields over a basis of *vector functions* [32],

$$\vec{E} = \sum_{i=1}^N x_i \vec{\psi}_i. \quad (87)$$

Here  $N$  is the total number of basis functions in the expansion,  $x_i$  are unknown coefficients, and  $\vec{\psi}_i$  are the vector basis functions. These functions are second order node, edge, and face element functions, given in Appendix . They are specifically designed to model  $m = 1$  modes. Substituting (87) into (82) and exchanging the order of summation and integration yields

$$\sum_{i=1}^N x_i \left\{ \iint_{\Omega} \frac{1}{\mu_r} (\nabla \times \vec{\psi}_i) \cdot (\nabla \times \vec{\psi}_j) \, dv - k_0^2 \iint_{\Omega} \varepsilon_r \vec{\psi}_i \cdot \vec{\psi}_j \, dv \right\} = 0. \quad (88)$$

Ensuring (88) holds for all  $\vec{\psi}_j$  (same set of functions as  $\vec{\psi}_i$ ), ensures it will hold for any linear superposition of  $\vec{\psi}_j$ , the finite basis analogy of  $\delta \vec{E}$ . The  $N$  equations represented by (88) are *exactly* (83)–(85) taken over a finite basis, written conveniently in linear algebra notation as

$$\mathbf{S}\mathbf{X} - \xi \mathbf{T}\mathbf{X} = \mathbf{0}, \quad (89)$$

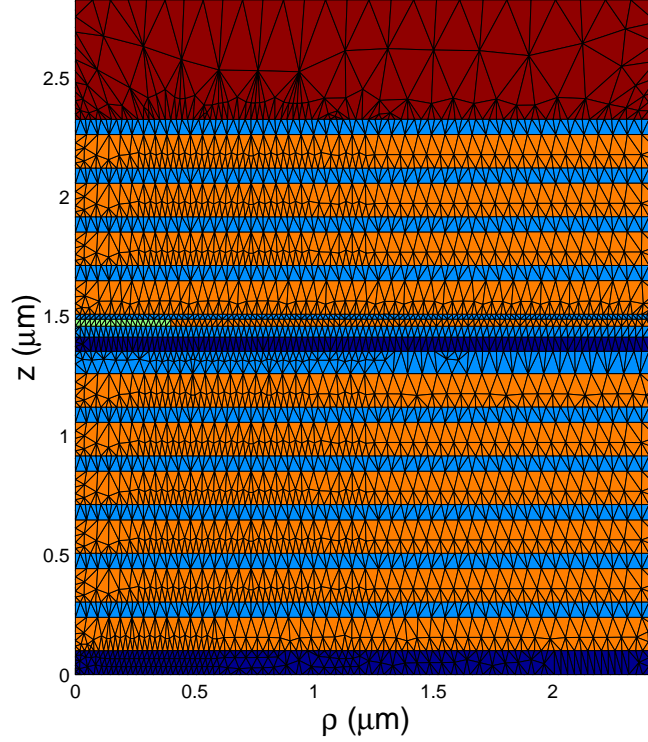


FIG. 20: Sample finite element mesh for an oxide-apertured, oxide DBR VCSEL.

where,

$$s_{i,j} \equiv \iint_{\Omega} \frac{1}{\mu_r} \left( \nabla \times \vec{\psi}_i \right) \cdot \left( \nabla \times \vec{\psi}_j \right) dv, \quad (90)$$

$$t_{i,j} \equiv \iint_{\Omega} \varepsilon_r \vec{\psi}_i \cdot \vec{\psi}_j dv, \quad (91)$$

and the eigenvalue ( $\xi$ ) definition (86) remains unchanged.

We define our basis set over a triangular mesh in the  $\rho - z$  plane, as illustrated in Fig. 20. By using (randomly shaped) triangular elements, we can accommodate general VCSEL designs—including for example *tapered oxides*—and avoid creating an artificial, mesh-driven predisposition to any given vector field component. Due to the form of our basis expansion and the use of absorbing regions (discussed below),  $\mathbf{S}$  and  $\mathbf{T}$  will be very large ( $N \sim 50,000$ ), sparse, non-Hermitian matrices. As a result, special matrix techniques are required to solve (89). In practice this is the most challenging part of the finite element solution, and certainly the most time consuming. We chose to solve the eigenvalue problem using an iterative Arnoldi algorithm [33, 34] with spectral transformation; this algorithm allows us to search for “mildly complex” (e.g.,  $\text{Re}(\xi) \gg \text{Im}(\xi)$ ) eigenvalues over a given range of the real axis.

By far the greatest potential error source in the finite element VCSEL analysis is mesh termination. Due to the incomplete optical confinement of both the oxide apertures and the VCSEL mirrors, the true domain of a VCSEL field solution extends to infinity in all directions. Hence, an artificial mesh termination is required for FEM application. A properly designed mesh termination for this problem must mimic the unbounded nature of the domain, eliminating non-physical reflections at the mesh edge. In addition, since the FEM computational demand—both CPU time and memory—scales super-linearly with  $N$ , we prefer to place our termination as close as possible to the primary domain of interest, thereby minimizing the amount of “wasted” mesh space.

To terminate our mesh, we insert an artificial *absorbing layer* (AL) between the principle problem (VCSEL) domain ( $\Omega_V$ ) and the problem boundary ( $\Gamma$ ) [31]. This layer allows us to use perfect conductor boundary conditions on  $\Gamma$ , as we assumed earlier, eliminating the surface integral term in the variational form and dramatically simplifying the FEM analysis. We define  $\Omega_V$  by a rectangular region in the  $\rho - z$  plane, bounded by the bottom mirror-to-substrate plane ( $\Gamma_B$ ) and the top mirror-to-air plane ( $\Gamma_T$ ) in the  $\hat{z}$  direction, and the transverse lasing mode size ( $\Gamma_S$ ) in the  $\hat{\rho}$  direction. We determine  $\Gamma_S$  *a-posteriori*, as discussed below. We surround  $\Omega_V$  by the AL as illustrated in Fig. 21, where the AL domain is the union of the top, side, and bottom AL regions ( $\Omega_{AL} = \Omega_T \cap \Omega_S \cap \Omega_B$ ). Due to the high reflectance of the distributed Bragg reflectors (DBRs), our main concern is absorbing any radiation incident on the radial boundary  $\Gamma_S$ . Therefore, we focus our analysis on the radial AL ( $\Omega_S$ ); the optimal axial AL design ( $\Omega_T$  and  $\Omega_B$ ) falls out of the radial analysis as we show explicitly later.

A basic requirement for minimizing reflection is that the impedance  $\left(\sqrt{\mu/\varepsilon}\right)$  of the absorbing layer in each region must match the radially adjacent VCSEL region. We enforce this condition by defining the absorbing layer material parameters as <sup>1</sup>

$$\varepsilon_{r,j}^{AL}(\rho) \equiv a(\rho)\varepsilon_{r,j}, \quad \text{and} \quad \mu_{r,j}^{AL}(\rho) \equiv a(\rho)\mu_{r,j}. \quad (92)$$

Here  $\varepsilon_{r,j}$  and  $\mu_{r,j}$  are the VCSEL material parameters in axial region  $j$  (defined by  $z_{j-1} <$

---

<sup>1</sup> Before choosing (92), we considered a diagonal anisotropic  $\bar{a}(\rho)$  for a *perfectly* matched layer (PML) design [35, 36]. However, we found that the extra degrees of freedom provided no advantage for absorbing *general* outward propagating cylindrical waves of the form  $\left(H_m^{(2)}(k\rho)e^{i\beta z}e^{im\phi}\right)$ .

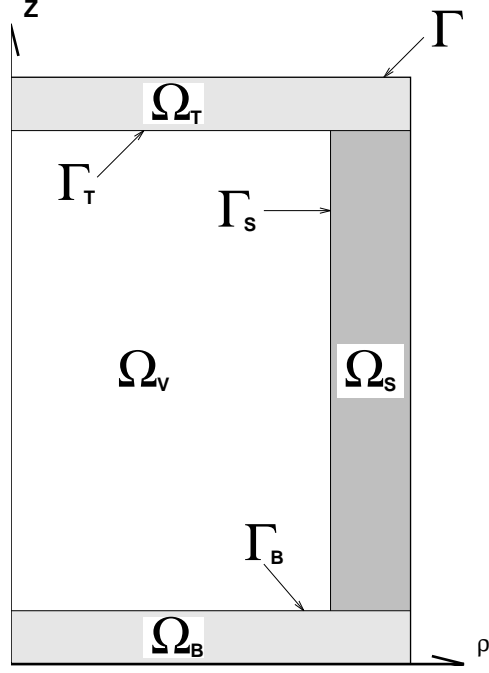


FIG. 21: Illustration of the FEM VCSEL problem domain:  $\Omega_V$  is the VCSEL domain, and  $\Omega_S$ ,  $\Omega_T$ , and  $\Omega_B$  are the side, top, and bottom absorbing layer (AL) domains, respectively. The VCSEL and AL domains are separated by the boundaries  $\Gamma_S$ ,  $\Gamma_T$ , and  $\Gamma_B$ , and the entire problem domain is bounded by the closed cylinder  $\Gamma$ .

$z < z_j$ ) radially adjacent to the AL (e.g., just to the left of  $\Gamma_S$ ), and

$$a(\rho) \equiv 1 - ib(\rho). \quad (93)$$

The absorbing layer performance depends entirely on the function  $b(\rho)$ . We arrive at a suitable function  $b(\rho)$  through a detailed design optimization. First, we obtain a rough estimate using an asymptotic description of the fields and reflections, as described in more detail later. Then we fine-tune the layer by minimizing the exact reflection values as obtained by a rigorous transfer matrix calculation.

To illustrate the application of the FEM for VCSELs, we analyze several versions of a basic 870 nm oxide-apertured, oxide DBR VCSEL [37]. The VCSEL has five and a half periods of  $\text{Al}_{0.3}\text{Ga}_{0.7}\text{As}/\text{Al}_x\text{O}_y$  in the bottom DBR and four in the top DBR. The cavity is  $1\lambda$  thick and contains a single 600 Å GaAs *bulk* gain region centered between two  $\text{Al}_{0.3}\text{Ga}_{0.7}\text{As}$  barrier layers. A 300 Å AlAs layer is included in the top barrier to form an oxide aperture. Although an actual oxide aperture formed in AlAs would have a square cross-section, we

treat it as circular to maintain the azimuthal symmetry. The entire structure including the GaAs substrate is illustrated in Fig. 20. The versions of this structure we examined are:

- 1 $\lambda$ –1THIN the structure as described above,
- 1 $\lambda$ –1THICK same structure with a 600 Å thick oxide aperture,
- 1 $\lambda$ –2THICK same structure with a 600 Å thick oxide aperture in both the top and bottom barrier regions, and
- $\lambda/2$ –1THICK same DBRs but with a  $\lambda/2$  cavity and a 600 Å thick oxide aperture in the top barrier region.

All materials indices are assumed to be real so that the only source of field loss is through absorption in the ALs. For this particular structure, the details of generating the absorbing layer function  $b(\rho)$  will later be shown.

In Figs. 22 and 23 we plot  $|E_\phi|$  and the time averaged electromagnetic energy density,

$$w \equiv \frac{1}{4} \left[ \varepsilon_0 \varepsilon_{r,j} \left| \vec{E} \right|^2 + \mu_0 \left| \vec{H} \right|^2 \right], \quad (94)$$

for the sample 1 $\lambda$ –1THIN,  $\rho_{ox} = 0.4 \mu\text{m}$  VCSEL; these plots are representative of the general lasing mode profiles for all the VCSELs we tested. The fields are found by substituting the lasing mode eigenvector ( $\mathbf{X}$ ) into the field expansion given in (87). The  $E_\phi$  profile (Fig. 22) is similar to the familiar standing wave profile obtained via simple scalar field techniques, however, we anticipate our result is more accurate due to the full vector solution. The energy density (94) is found by estimating  $\vec{H}$  from the  $\vec{E}$  field expansion (87) and Faraday's law. Although this is less familiar than the  $E_\phi$  profile, it is a more accurate representation of the spatial mode energy distribution throughout the VCSEL.

Using the spatial mode profile, we estimate the total and transverse confinement factors as

$$\Gamma^{\text{tot}} \equiv \frac{\int_{\Omega_{\text{pump}}} w dv}{\int_{\Omega_V} w dv}, \quad (95)$$

and

$$\Gamma^{\text{tr}} \equiv \frac{\int_{\Omega_{\text{pump}}} w dv}{\int_{\Omega_{\text{gain}}} w dv}, \quad (96)$$

respectively;  $\Omega_V$  is the VCSEL volume, and  $\Omega_{\text{pump}}$  and  $\Omega_{\text{gain}}$  are the pumped and total volume of the gain region, respectively. For purpose of calculation, we estimate  $\Omega_{\text{pump}}$  as

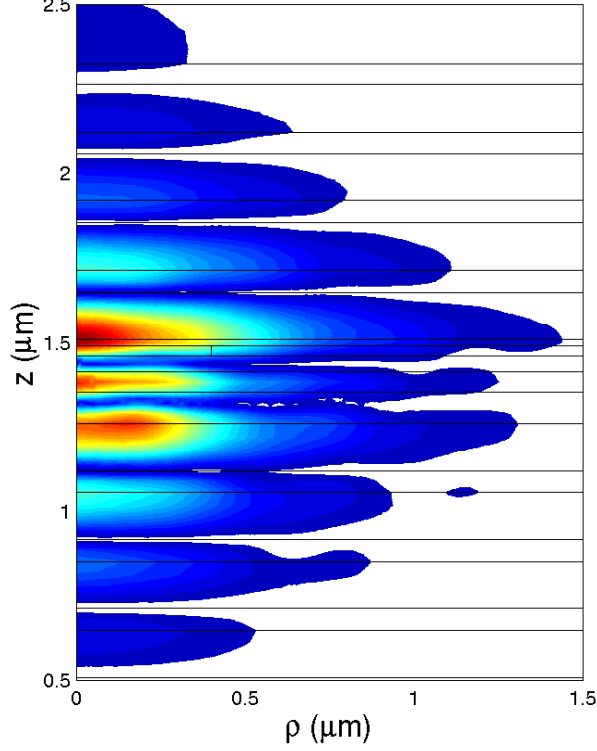


FIG. 22: Example plot of  $|E_\phi|$  for the  $1\lambda$ -1THIN structure with oxide aperture radius  $\rho_{ox} = 0.4 \mu\text{m}$ . To increase clarity, the figure domain is smaller than the calculation domain, and the background intensity has been set to white.

the volume of the active layer inside the oxide aperture (e.g., with  $\rho \leq \rho_{ox}$ ). The total confinement factor represents the percentage of the mode *energy* overlapping the active gain region<sup>2</sup>. We use this later in the Fabry-Perot laser equation to estimate material threshold gain from the total modal loss (102). The transverse confinement factor has less quantitative application but is a nice indicator of how well the lasing mode is confined in the transverse dimension.

We plot  $\Gamma^{\text{tr}}$  for each of the VCSEL structures in Fig. 24. The results for the  $1\lambda$  cavity are somewhat intuitive: for any given radius more and thicker oxides yield greater confinement. For the  $\lambda/2$  case, the oxide aperture does not overlap well (in the  $z$  direction) with the standing wave. Therefore, the transverse confinement is relatively small, however, the total

<sup>2</sup> This is a somewhat different definition than the more standard definition using the standing wave *intensity* ( $\sim |\vec{E}|^2$ ). However, the two definitions should yield similar results in most cases.



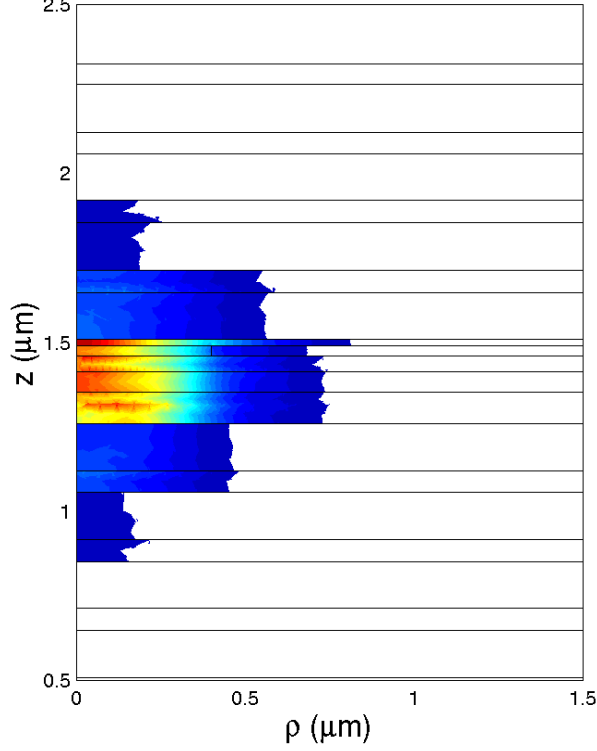


FIG. 23: Example plot of the stored energy density  $w$  for the  $1\lambda$  -1THIN structure with oxide aperture radius  $\rho_{ox} = 0.4 \mu\text{m}$ . To increase clarity, the figure domain is smaller than the calculation domain, and the background intensity has been set to white.

confinement factor—due to the short cavity—is very large, as shown in Fig. 25. The high contrast DBRs allow less field penetration and therefore a very high total confinement factor for all four test cases, compared to analogous semiconductor DBR VCSELs.

Due to the absorbing layers, the eigenvalues of (86) are complex, and take the general form

$$\xi_i = k_i^2 = \frac{\omega_i^2}{c^2} \equiv (r_i + i q_i)^2. \quad (97)$$

Here  $r_i$  and  $q_i$  are the real and complex parts of the (total) propagation constant  $k_i$  of mode  $i$ . From (97) we immediately recognize the mode resonance as

$$\lambda_i = \frac{2\pi}{r_i}. \quad (98)$$

By definition, the fields vary harmonically as

$$\exp(i\omega_i t) = \exp(ik_i c t) = \exp(ir_i c t) \exp(-q_i c t), \quad (99)$$

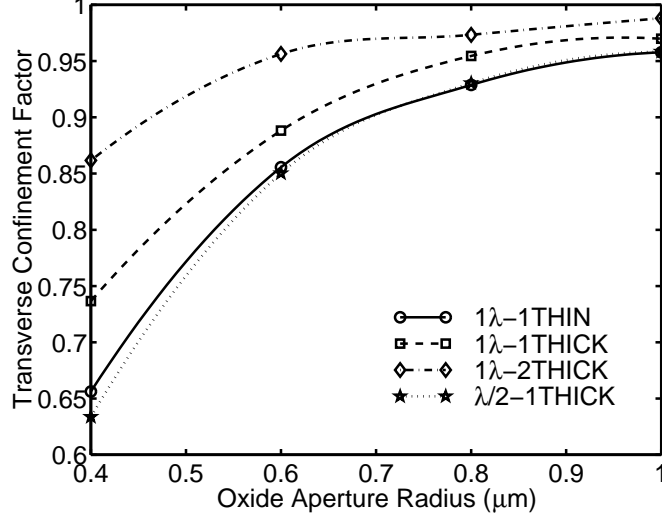


FIG. 24: Transverse confinement factor verses oxide aperture radius for the fundamental lasing mode. The lines are cubic spline fits of the discrete calculation data.

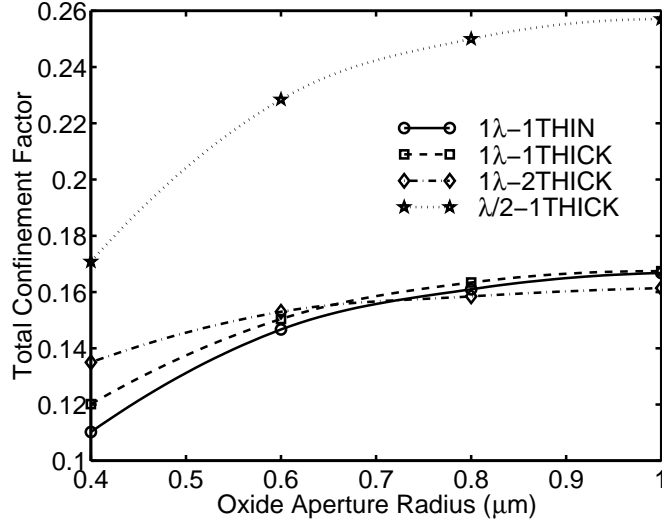


FIG. 25: Total confinement factor verses oxide aperture radius for the fundamental lasing mode. The lines are cubic spline fits of the discrete calculation data.

where the mode frequency is  $\text{Re}(\omega_i) = r_i c$  and the *total* cavity loss rate (1/seconds) is  $l_i \equiv q_i c$ . These results describe a three-dimensional leaky cavity, losing energy at a rate of  $l_i$ . We would prefer to express our results in terms of the more familiar Fabry-Perot (F-P)

laser model. To do this, we convert  $\omega_i$  to a complex propagation constant

$$\beta_i \equiv \frac{\omega_i^*}{c} n_{\text{gain}}, \quad (100)$$

where  $*$  is the complex conjugate, required such that a lossy  $\omega_i$  maps to a lossy  $\beta_i$ . The imaginary part of  $\beta_i$  gives the *field* loss rate (for  $\text{Im}(\beta_i) > 0$ ) in  $\text{cm}^{-1}$ . Since energy is proportional to the *square* of the field, the *intensity* lost per unit length ( $\alpha_i$ ) is given by

$$\alpha_i \equiv 2 \text{Im}(\beta_i). \quad (101)$$

In deriving  $\alpha_i$  *all* we have done is convert energy lost per time to energy lost per propagation length. To apply this loss rate to a “textbook” Fabry-Perot laser, the cavity length would have to be adjusted in accordance with the blueshift [10]. Finally, we calculate the threshold gain ( $g_{th}$ ) from the F-P lasing condition,

$$\Gamma_i^{\text{tot}} g_{th,i} = \alpha_i. \quad (102)$$

In Figs. 26 and 27 we plot the modal resonance and threshold gain as a function of oxide aperture radius for all four test VCSELs. The resonance results show the now familiar blueshift, with more and thicker oxide apertures yielding a larger shift. Interpretation of the threshold gain curves is more complicated. We discuss these results later in our discussions regarding optical losses and diffraction arising in this model.

To better understand the optical loss sources, we would like to divide the total optical mode loss ( $\alpha_i$ ) into a mirror loss ( $\alpha_i^{(\text{mirror})}$ ), due to emission out the ends of the VCSEL, and a diffraction loss ( $\alpha_i^{(\text{diffraction})}$ ), due to loss out the VCSEL side. To do this, we use conservation of energy and the relationship between  $\alpha$  and the radiated power and stored energy [24],

$$\alpha = \frac{P_V}{v_p W_V}. \quad (103)$$

Here  $v_p$  is the field phase velocity,

$$P_V \equiv \frac{1}{2} \text{Re} \left\{ \iint_{\Gamma_V} (\vec{E} \times \vec{H}^*) \cdot d\vec{s} \right\} \quad (104)$$

is the total time averaged (real) power exiting the VCSEL ( $\Omega_V$ ) through  $\Gamma_V$ , and

$$W_V \equiv W_V^e + W_V^m \quad (105)$$

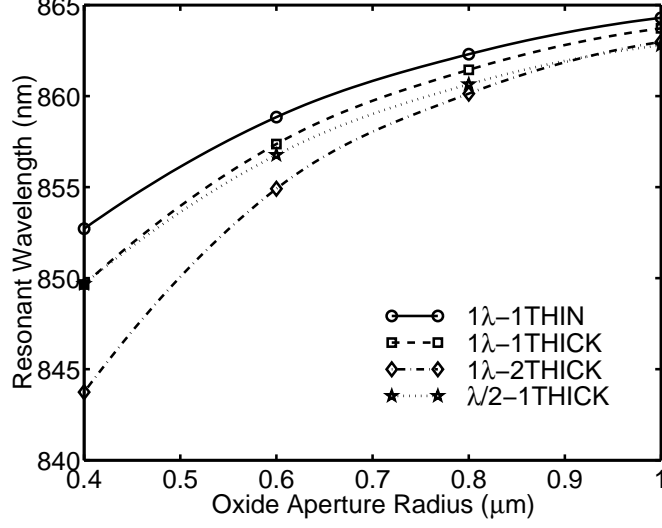


FIG. 26: Lasing mode resonance versus oxide aperture radius. The lines are cubic spline fits of the discrete calculation data.

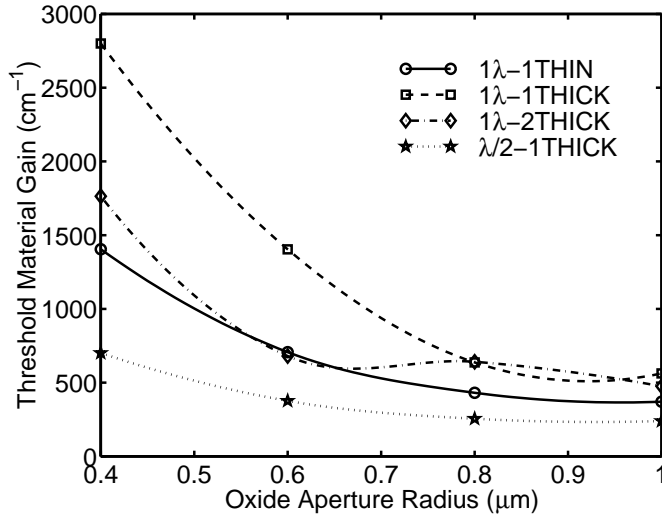


FIG. 27: Threshold (material) gain versus oxide aperture radius. The lines are cubic spline fits of the discrete calculation data.

is the total time averaged stored energy. This consists of the electric and magnetic field energies,

$$W_V^e \equiv \frac{1}{4} \iiint_{\Omega_V} \varepsilon_0 \varepsilon_{r,j} a \left| \vec{E} \right|^2 dv, \quad (106)$$

and

$$W_V^m \equiv \frac{1}{4} \iiint_{\Omega_V} \mu_0 a \left| \vec{H} \right|^2 dv, \quad (107)$$

respectively. Equation (103) is derived from the relationship between cavity Q and loss rate, adapted to the F-P laser model. We find in practice that numerical application of (103) gives results *exactly* matching those obtained with (101), verifying the general approach. It is then a simple matter to break  $\alpha$  into radial and axial components,

$$\alpha^{(\text{diffraction})} = \frac{P_S}{v_p W_V}, \quad (108)$$

and

$$\alpha^{(\text{mirror})} = \frac{P_T + P_B}{v_p W_V}. \quad (109)$$

Here

$$P_V = P_S + P_T + P_B, \quad (110)$$

breaks the total power exiting the VCSEL into that leaving through the side ( $P_S$ ), and that leaving through the top and bottom surfaces ( $P_T$ ) and ( $P_B$ ), respectively. These powers are calculated by restricting the integral in (104) to the corresponding surfaces. Note that for these calculations, we assume the VCSEL materials are lossless and calculate “cold cavity” radiative loss parameters. Although absorptive loss may be significant in operating VCSELs, this calculation should give a good estimate of the diffraction loss. The calculation can be easily modified to fold in absorptive losses if required.

In Figs. 28 and 29, we plot the radial mode loss and the radial percentage of the total mode loss, respectively. Comparing the two figures, we see that  $\alpha^{(\text{mirror})}$  the majority of the change in threshold with aperture radius is due to a change in  $\alpha^{(\text{diffraction})}$ . This is not surprising, since we expect the change in mirror reflectivity to be relatively small and the diffraction to increase as the aperture size decreases.

By examining the loss characteristics for each VCSEL design, we may deduce the physical mechanisms governing diffraction. Our results support the idea that diffraction may be viewed as a coupling between the bound eigenmode and the continuum of parasitic modes [38]. These are *radially* propagating slab modes in the unapertured (cladding) region. Deppe explains in [26] that for a cavity bound by perfectly conducting mirrors, the parasitic mode density will resemble a slanted staircase following the three dimensional density of modes. The jumps in the staircase occur at each vertical resonance in the cladding region.

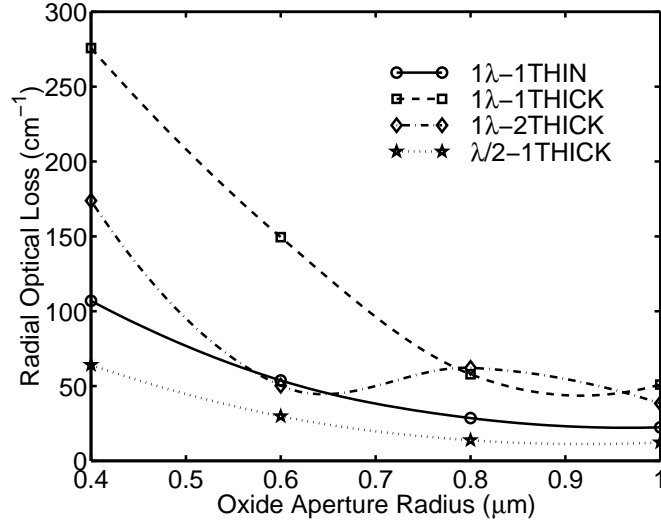


FIG. 28: Radial mode loss verses oxide aperture radius for the fundamental lasing mode. The lines are cubic spline fits of the discrete calculation data.

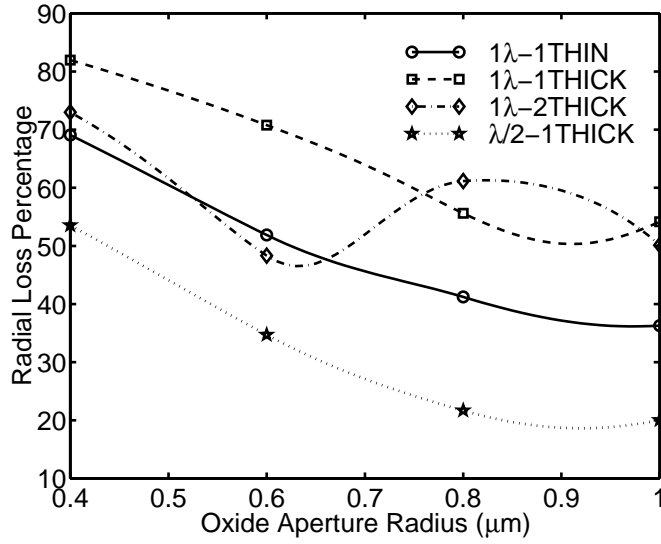


FIG. 29: Percentage of the total mode loss due to radial losses for the fundamental lasing mode. The lines are cubic spline fits of the discrete calculation data.

Deppe's results suggest that shorter cavities are superior since the eigenmode overlaps with a smaller density of parasitic modes. This idea is illustrated in Fig. 30.

For our high contrast DBRs, we expect very similar behavior to this ideal mirror case. Comparing the threshold gains of each structure (Fig. 27), the  $\lambda/2$  cavity threshold is con-

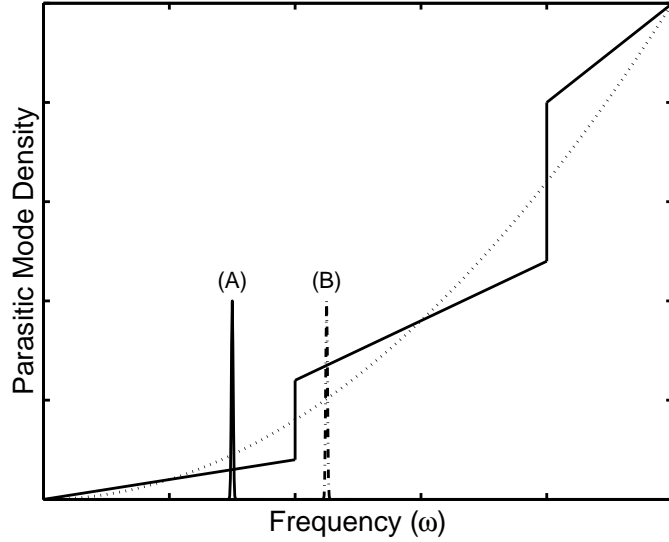


FIG. 30: Illustration of the “slanted staircase” parasitic mode density. The density follows the three-dimensional, free-space density of optical modes (dotted line). The jumps in the staircase occur at each vertical resonance in the cladding region. The two discrete modes are representative of a low threshold (A), and a higher threshold (B) lasing mode.

sistently lower than all the  $1\lambda$  cases. Moreover, comparing the percentage of the total mode energy lost to diffraction (Fig. 29), the  $\lambda/2$  VCSEL is again superior. These results can’t be attributed to transverse confinement, since the  $\lambda/2$  VCSEL has the smallest  $\Gamma^{\text{tr}}$  of all four cases. However, these results *could* be attributed to the larger *total* confinement factor (Fig. 25), *or* to a smaller density of parasitic modes interacting with the  $\lambda/2$  cavity eigenmode. It turns out that these two factors are closely related: the *longitudinal* confinement factor—or effective cavity length in the *cladding* region—determines the location of the steps in the parasitic mode density (Fig. 30).

Adopting Deppe’s parasitic mode density interpretation, we can explain the difference in threshold between the  $\lambda/2$  and  $1\lambda$  cavity VCSELs, but we *cannot* easily explain the disparity among the three  $1\lambda$  cases, which should have very similar parasitic mode densities. Furthermore, the parasitic mode density is *solely* a function of (effective) cavity length, and therefore cannot address radius-dependent changes in diffraction. To capture these radius-dependent effects, and to distinguish the various  $1\lambda$  cavity structures, we propose that the diffractive loss is a function of *both* the density of parasitic modes *and* the coupling strength between the eigenmode and the parasitic modes. Moreover, this coupling strength

is a function of two factors: (1) the relative alignment of the eigenmode and parasitic mode propagation vectors, and (2) the eigenmode penetration into the cladding region.

The  $1\lambda$ -1THIN VCSEL exhibits the lowest threshold and the lowest diffraction loss (Fig. 28) of all three  $1\lambda$  VCSELs. Because of the weak transverse confinement (Fig. 24) and the resulting mode spread, the field in this structure is more planar and the propagation vector is paraxial with respect to normal to the planar interfaces. As a result, the eigenmode wavevector is nearly *orthogonal* to the parasitic mode wavevectors, which lie principally in the plane of the layer structure. The parasitic mode wavevectors can have components out of the plane, but the larger these components are the less energy they will carry away in the radial direction. We attribute the low threshold for this design to this misalignment between the eigenmode and parasitic mode wavevectors. This hypothesis is further supported by the peculiar results for the double-apertured  $1\lambda$ -2THICK VCSEL.

The double-apertured VCSEL has the largest transverse confinement factor of all three  $1\lambda$  cavity VCSELs. Using the weighted index method [39], we showed that this transverse confinement has two primary effects:

1. It *confines* the mode energy within the aperture region.
2. It causes the eigenmode propagation vector to *tilt* away from normal to the DBRs.

The first effect acts to *decrease* the parasitic mode (or diffractive) loss by containing the mode energy, while the second acts to *increase* it through stronger coupling (better propagation vector alignment) to the parasitic modes. These processes compete, and, depending on VCSEL design and aperture radius, either effect may dominate. For the  $1\lambda$ -2THICK VCSEL, the transverse confinement is  $\geq 0.95$  for aperture radii from  $1.0$  to  $0.6\ \mu\text{m}$ ; for these radii, the first effect dominates. However, somewhere between  $0.6$  and  $0.4\ \mu\text{m}$  enough mode energy exists outside the oxide aperture such that the strong parasitic mode coupling causes the optical loss to rapidly increase. In essence, the cavity in the unapertured region ( $\rho \geq \rho_{ox}$ ) forms a waveguide whose source is the lasing eigenmode. When the eigenmode penetration into the waveguide region becomes large enough, the waveguide appears to “siphon” energy away from the eigenmode. This effect is clearly illustrated in the plots of  $|E_\phi|$  for the  $0.6$  and  $0.4\ \mu\text{m}$  cases in Figs. 31 and 32, respectively.

We have performed quasi-exact calculations of the lasing mode parameters in an oxide apertured, oxide DBR VCSEL. Our results are consistent with past trends from measure-



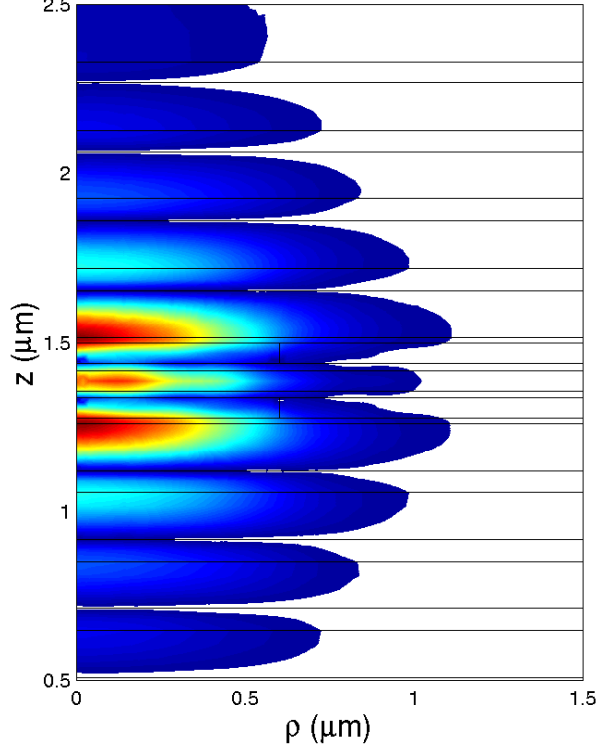


FIG. 31:  $|E_\phi|$  for the  $1\lambda$ -2THICK structure with oxide aperture radius  $\rho_{ox} = 0.6 \mu\text{m}$ . To increase clarity, the figure domain is smaller than the calculation domain, and the background intensity has been set to white.

ment and calculation. We find a blueshift in modal resonance with aperture radius and design. Most importantly, we calculate the total optical mode loss and threshold gain for our microcavity VCSELs. From these results we found that the physical factors which determine the parasitic mode loss are the density of parasitic modes and the percentage of the eigenmode coupling to the parasitic modes. The coupling percentage is itself a function of the eigenmode penetration into the cladding ( $\rho > \rho_{ox}$ ) region and the relative alignment between the parasitic mode and eigenmode propagation vectors. Roughly speaking, these two factors determine the magnitude of the parasitic mode source and the strength of the eigenmode-to-parasitic mode coupling.

This model may be used to qualitatively explain past, seemingly conflicting, oxide design results. In [40], the authors suggest thinner oxides placed at standing wave antinodes give the lowest thresholds. They consider semiconductor DBR VCSELs with longer effective cavity lengths and relatively large parasitic mode densities, approaching the three dimensional

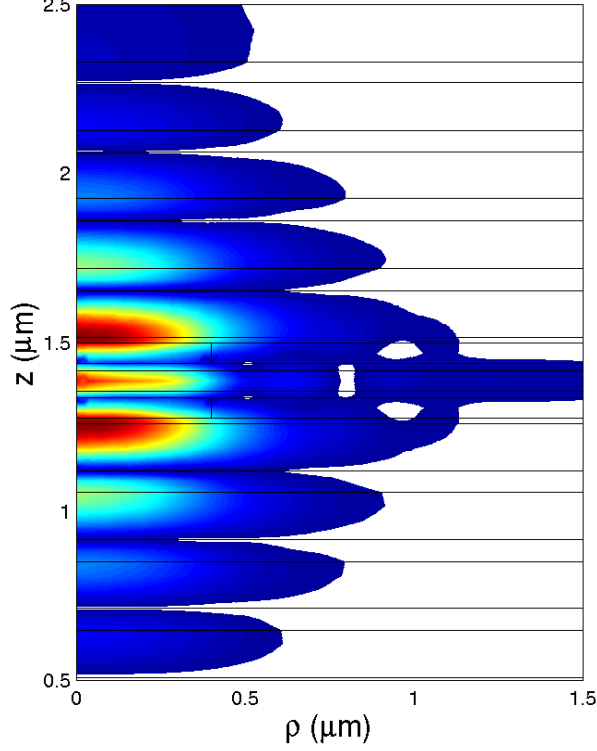


FIG. 32:  $|E_\phi|$  for the  $1\lambda$ -2THICK structure with oxide aperture radius  $\rho_{ox} = 0.4 \mu\text{m}$ . Note the field leakage into the waveguide formed by the oxide apertures and the cavity. To increase clarity, the figure domain is smaller than the calculation domain, and the background intensity has been set to white.

density of modes. As a result, even weak coupling to the parasitic mode continuum will yield a large diffractive loss, implying thinner oxides are better for their structures. On the other hand, the authors of [41] work with a  $\lambda/2$  cavity VCSEL with one semiconductor and one dielectric DBR. In their case, the cavity and corresponding optical density of modes is much smaller, and the confinement aspect of their oxide aperture dominates the increased coupling strength to yield a low threshold design.

Finally, we note that our general finite element method can also be extended to calculate the heat and carrier distribution throughout the VCSEL to yield an even more complete model. These are both scalar quantities and are therefore much easier to calculate. The main drawback with the FEM is the computational power, time, and memory required to solve the large sparse, complex, non-Hermitian generalized eigenvalue problem. However, with the availability of much faster processors and much larger memory modules in the near

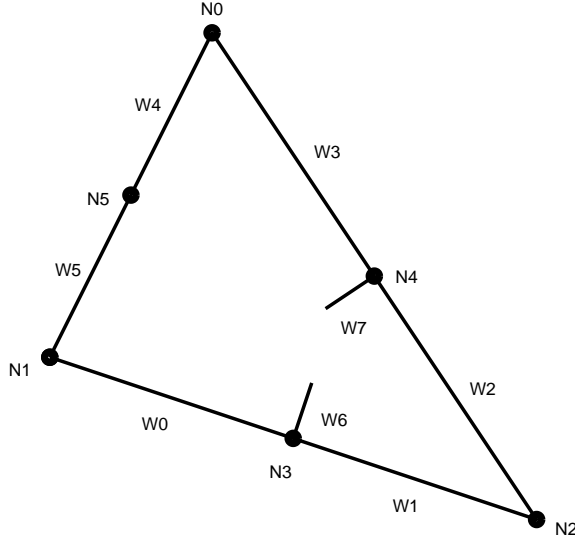


FIG. 33: Numbering convention of the six node, six edge, and two face based element functions.

future, this issue may soon disappear.

#### *Vector Basis Functions for $m=1$ Modes*

In this separate section, we review the vector basis functions employed in our finite element model. Based on the literature, we choose to span the mesh using second order node, edge, and face element functions [42, 43]. These functions have been shown to be a good compromise between mesh density and function order, roughly minimizing the total number of unknowns required to obtain a given solution accuracy. For each triangle in the mesh there are 14 basis functions: 6 node based  $(\vec{N}_0 - \vec{N}_5)$ , 6 edge based  $(\vec{W}_0 - \vec{W}_5)$ , and two face based  $(\vec{W}_6, \vec{W}_7)$ , as illustrated in Fig. 33[43, 44]. To define the 14 element functions, we use simplex (or barycentric) coordinates, defined over the triangular element via the affine transformation [45, 46],

$$\begin{bmatrix} 1 \\ \rho \\ z \end{bmatrix} = \begin{bmatrix} 1 & 1 & 1 \\ \rho_0 & \rho_1 & \rho_2 \\ z_0 & z_1 & z_2 \end{bmatrix} \begin{bmatrix} \zeta_0 \\ \zeta_1 \\ \zeta_2 \end{bmatrix}. \quad (111)$$

Here  $(\rho_0, z_0)$ ,  $(\rho_1, z_1)$ , and  $(\rho_2, z_2)$  are the three corners of the triangle, and  $\zeta_0$ ,  $\zeta_1$ , and  $\zeta_2$  are the simplex coordinates. Based on the  $\zeta_i$ , the element *vector* functions are

$$\vec{N}_0 \equiv (2\zeta_0 - 1) \zeta_0 (\hat{\phi} + \hat{\rho}), \quad (112)$$

$$\vec{N}_1 \equiv (2\zeta_1 - 1) \zeta_1 (\hat{\phi} + \hat{\rho}), \quad (113)$$

$$\vec{N}_2 \equiv (2\zeta_2 - 1) \zeta_2 (\hat{\phi} + \hat{\rho}), \quad (114)$$

$$\vec{N}_3 \equiv 4\zeta_0\zeta_1 (\hat{\phi} + \hat{\rho}), \quad (115)$$

$$\vec{N}_4 \equiv 4\zeta_1\zeta_2 (\hat{\phi} + \hat{\rho}), \quad (116)$$

$$\vec{N}_5 \equiv 4\zeta_0\zeta_2 (\hat{\phi} + \hat{\rho}), \quad (117)$$

$$\vec{W}_0 \equiv \rho\zeta_1\nabla_\tau\zeta_2 = \frac{\rho\zeta_1}{\Delta} \{b_2\hat{\rho} + c_2\hat{z}\}, \quad (118)$$

$$\vec{W}_1 \equiv \rho\zeta_2\nabla_\tau\zeta_1 = \frac{\rho\zeta_2}{\Delta} \{b_1\hat{\rho} + c_1\hat{z}\}, \quad (119)$$

$$\vec{W}_2 \equiv \rho\zeta_2\nabla_\tau\zeta_0 = \frac{\rho\zeta_2}{\Delta} \{b_0\hat{\rho} + c_0\hat{z}\}, \quad (120)$$

$$\vec{W}_3 \equiv \rho\zeta_0\nabla_\tau\zeta_2 = \frac{\rho\zeta_0}{\Delta} \{b_2\hat{\rho} + c_2\hat{z}\}, \quad (121)$$

$$\vec{W}_4 \equiv \rho\zeta_0\nabla_\tau\zeta_1 = \frac{\rho\zeta_0}{\Delta} \{b_1\hat{\rho} + c_1\hat{z}\}, \quad (122)$$

$$\vec{W}_5 \equiv \rho\zeta_1\nabla_\tau\zeta_0 = \frac{\rho\zeta_1}{\Delta} \{b_0\hat{\rho} + c_0\hat{z}\}, \quad (123)$$

$$\begin{aligned} \vec{W}_6 &\equiv \rho 4\zeta_1 (\zeta_2\nabla_\tau\zeta_0 - \zeta_0\nabla_\tau\zeta_2) \\ &= \frac{\rho 4\zeta_1}{\Delta} \{\zeta_2 (b_0\hat{\rho} + c_0\hat{z}) - \zeta_0 (b_2\hat{\rho} + c_2\hat{z})\}, \end{aligned} \quad (124)$$

$$\begin{aligned} \vec{W}_7 &\equiv \rho 4\zeta_2 (\zeta_0\nabla_\tau\zeta_1 - \zeta_1\nabla_\tau\zeta_0) \\ &= \frac{\rho 4\zeta_2}{\Delta} \{\zeta_0 (b_1\hat{\rho} + c_1\hat{z}) - \zeta_1 (b_0\hat{\rho} + c_0\hat{z})\}. \end{aligned} \quad (125)$$

Here

$$\nabla_\tau \equiv \frac{\partial}{\partial \rho} \hat{\rho} + \frac{\partial}{\partial z} \hat{z}, \quad (126)$$

the  $b_i$  and  $c_i$  are given by the inverse affine transformation,

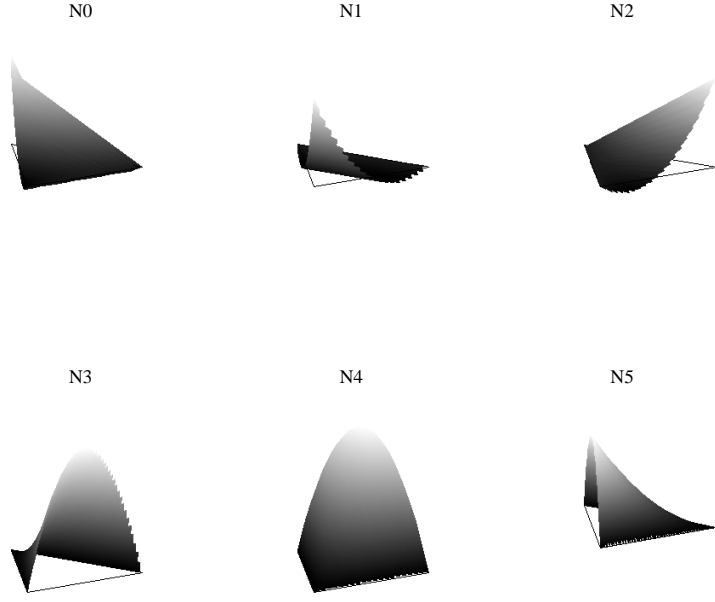


FIG. 34: Illustration of the six node based functions ( $\vec{N}_0 - \vec{N}_5$ ) for a typical element; the functions are overlayed on a triangle outline of the element.

$$\begin{bmatrix} \zeta_0 \\ \zeta_1 \\ \zeta_2 \end{bmatrix} = \frac{1}{\Delta} \begin{bmatrix} a_0 & b_0 & c_0 \\ a_1 & b_1 & c_1 \\ a_2 & b_2 & c_2 \end{bmatrix} \begin{bmatrix} 1 \\ \rho \\ z \end{bmatrix}, \quad (127)$$

and  $\Delta$  is twice the area of the triangle,

$$\Delta \equiv \sum_{i=0}^2 \rho_i (z_{i1} - z_{i2}) = \sum_{i=0}^2 \rho_i b_i = \sum_{i=0}^2 z_i c_i \quad (128)$$

( $i$ ,  $i1$ , and  $i2$  are modulo 3). These functions are illustrated in Figs. 34 and 35. These functions have three important properties that make them ideal for electromagnetic calculation in cylindrical coordinates.

First, when filling the  $\mathbf{S}$  and  $\mathbf{T}$  matrices, functions based on the same node or edge of neighboring elements (not necessarily with the same element function number  $\vec{N}_0 - \vec{W}_7$ ) are assigned the same coefficient  $x_i$ . As a result, the node and edge functions *naturally enforce tangential field continuity* (as illustrated in Fig. 36) *without necessarily forcing normal field continuity*, due to the two face functions.

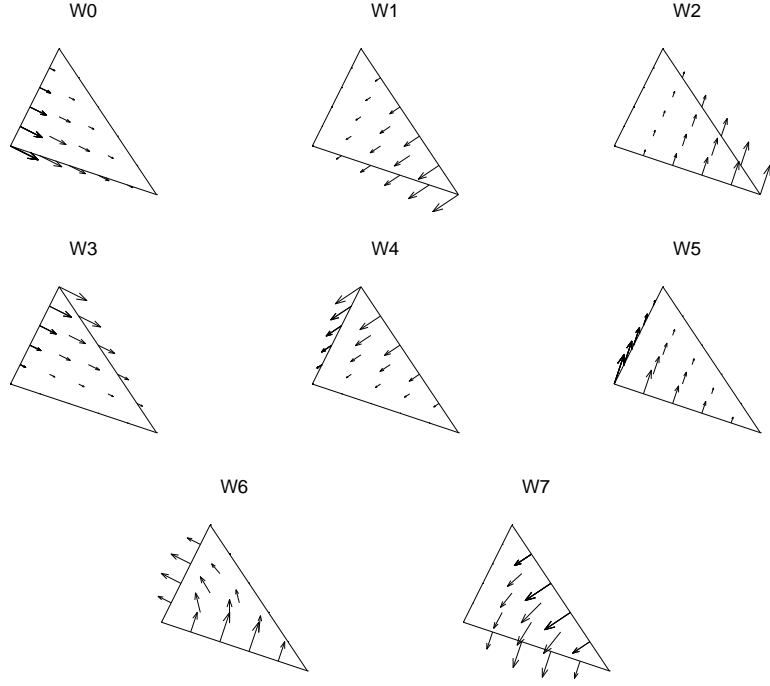


FIG. 35: Illustration of the six edge based ( $\vec{W}_0 - \vec{W}_5$ ) and the two face based ( $\vec{W}_6 - \vec{W}_7$ ) functions for a typical element; the functions are overlayed on a triangle outline of the element. These illustrations do not include the  $\rho$  weighting present in (118) – (125).

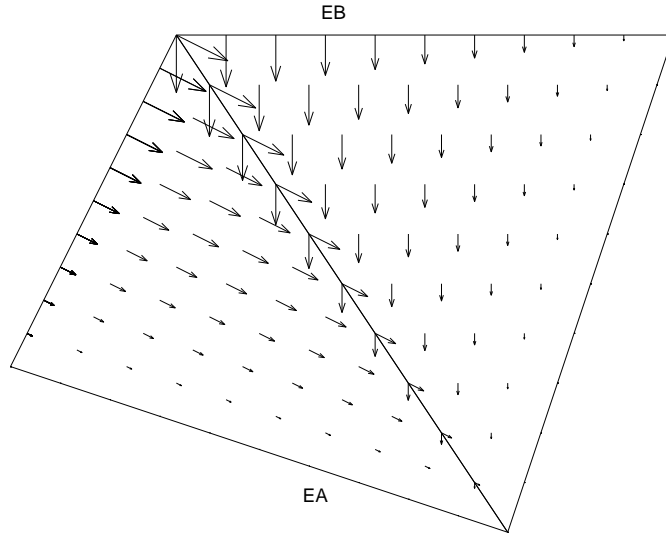


FIG. 36: Illustration of the natural tangential continuity between mesh elements. By assigning the same coefficient  $x_i$  to  $\vec{W}_1$  of element A and  $\vec{W}_0$  of element B, the vector sum of the two functions is tangential to their common edge.

Second, our element functions are modified from the more standard form [44] to force field regularity at  $\rho = 0$  (the axis condition). The lasing modes we seek are analogous to the ( $m = 1$ ) LP<sub>01</sub> fiber modes [23], where the azimuthal field dependence is  $\sin(\phi)/\cos(\phi)$ . The proper axis condition for the  $m = 1$  modes is [47]

$$\lim_{\rho \rightarrow 0} E_\rho = E_\phi, \quad (129)$$

and

$$\lim_{\rho \rightarrow 0} E_z = 0. \quad (130)$$

This condition is included in (112) – (125) by weighting the “standard” [44] edge and face functions by  $\rho$ , and including the node functions as part of the  $\hat{\rho}$  field expansion. Note that we may find  $m = 0$  and  $m > 1$  modes using a basis similar to (112) – (125), altered to accommodate the proper axis condition for these modes.

Third and least obvious, these elements properly model the null space of the curl operator, which has been shown to eliminate the occurrence of spurious solutions (modes) [48, 49].

#### *Absorbing Layer Design*

In this section, we give the details of an absorbing layer design pioneered for this effort. We use a two step process to optimize  $b(\rho)$ , the absorbing layer loss function: First, we obtain a rough estimate using an asymptotic description of the fields and reflections. Second, we fine-tune the layer by minimizing the exact reflection values as obtained by a rigorous transfer matrix calculation. In both steps we model the *radial* AL ( $\Omega_S$ ) as a set of discrete cylinders, as shown in Fig. 37, approximating  $a(\rho)$  as  $a_n = a((\rho_n + \rho_{n-1})/2)$ , where AL cylinder  $n$  is defined by  $[\rho_{n-1}, \rho_n]$ . To simplify further, we ignore the  $z$  dependence of the material parameters and perform our analysis using a single set of  $(\varepsilon_r, \mu_r)$ , the rough mean material values for the VCSEL. This should be sufficient, since we are not concerned about interfacial reflections between the various axial layers, and desire only to suppress non-physical radial reflections. We choose  $b(\rho)$  to minimize the reflection of cylindrical waves incident on the radial boundaries.

These waves are constructed from the  $\hat{z}$  and  $\hat{\phi}$  field components given in each region

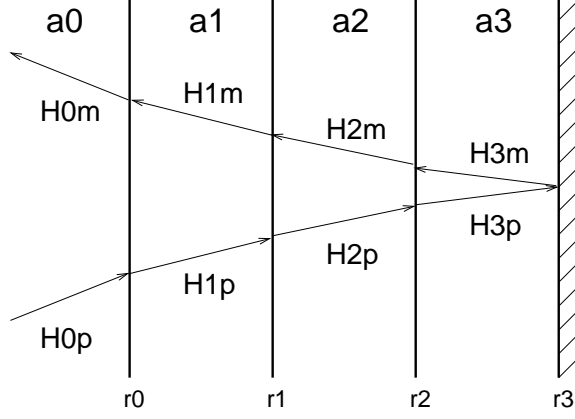


FIG. 37: Illustration of the geometry used to design the radial AL.  $\Omega_S$  is broken into discrete cylinders, each with a constant AL parameter  $a_n = a((\rho_n + \rho_{n-1})/2)$ .

(cylinder) by

$$H_{z,n}(\rho, z) = \left( A_n^{\text{TE}} H_0^{(2)}(k_n \rho) + B_n^{\text{TE}} H_0^{(1)}(k_n \rho) \right) e^{i\beta_n z}, \quad (131)$$

$$E_{z,n}(\rho, z) = \left( A_n^{\text{TM}} H_0^{(2)}(k_n \rho) + B_n^{\text{TM}} H_0^{(1)}(k_n \rho) \right) e^{i\beta_n z}, \quad (132)$$

$$H_{\phi,n}(\rho, z) = \frac{-i\omega\epsilon_0\epsilon_r a_n}{k_n^2} \frac{\partial E_z}{\partial \rho} \quad (133)$$

$$= \frac{i\omega\epsilon_0\epsilon_r a_n}{k_n} \left( A_n^{\text{TM}} H_1^{(2)}(k_n \rho) + B_n^{\text{TM}} H_1^{(1)}(k_n \rho) \right) e^{i\beta_n z},$$

$$E_{\phi,n}(\rho, z) = \frac{i\omega\mu_0 a_n}{k_n^2} \frac{\partial H_z}{\partial \rho} \quad (134)$$

$$= \frac{-i\omega\mu_0 a_n}{k_n} \left( A_n^{\text{TE}} H_1^{(2)}(k_n \rho) + B_n^{\text{TE}} H_1^{(1)}(k_n \rho) \right) e^{i\beta_n z},$$

where  $a_0 = 1$  ( $b_0 = 0$ ) in  $\Omega_V$  and we have assumed non-magnetic materials ( $\mu_r = 1$ ). The coefficients  $A_n^{\text{pol}}$  and  $B_n^{\text{pol}}$  are the magnitude for the outward and inward propagating waves, and pol = TE or TM labels the (uncoupled) polarizations of the  $m = 0$  modes. It has been shown [35] that absorbing layers that perform well for these  $m = 0$  modes will also work well for the  $m = 1$  modes that we are interested in.

We can describe cylindrical waves incident at an *angle*  $\theta$ —measured from the normal to  $\Gamma_S$  in the  $\rho - z$  plane ( $\hat{n}_{\Gamma_S}$ )—to the radial interface by writing the radial ( $k_n$ ) and axial ( $\beta_n$ ) propagation constants as

$$k_n = k_0 \eta a_n \cos(\theta), \quad (135)$$

$$\beta_n = k_0 \eta a_n \sin(\theta). \quad (136)$$



This choice ensures that  $k_n$  and  $\beta_n$  satisfy the dispersion relation

$$\omega^2 \mu_0 \varepsilon_0 \varepsilon_r a_n^2 = k_0^2 \varepsilon_r a_n^2 = k_n^2 + \beta_n^2, \quad (137)$$

in each region, where the (generally complex) index of refraction is

$$\eta \equiv \sqrt{\varepsilon_r}. \quad (138)$$

For the initial AL design analysis we employ the theory of small reflections [50], approximating the total Fresnel reflection for a cylindrical wave incident on the AL at  $\rho_0$  as

$$r \approx |r_0| + |r_1| t_1 + |r_2| t_{1,2} + \dots + |r_{N_{cyl}}| t_{1,2,\dots,N_{cyl}}. \quad (139)$$

Here  $N_{cyl}$  is the total number of cylinders in the AL,  $r_n$  is the Fresnel reflection coefficient at  $\rho_n$ , and  $t_{1,2,\dots,n}$  gives the attenuation due to the propagation from  $\rho_0$  to  $\rho_n$  and back. We use  $|r_n|$  rather than  $r_n$  in (139) to minimize the interference effects, since we are after a broadband AL design optimized for all angles of incidence. We estimate  $r_n$  using the asymptotic form for cylindrical waves in each region  $n$ . Due to the form of (92) and (131) – (134), the magnitude of the TE and TM Fresnel reflection coefficients are the same, hence we need only perform the analysis once. Taking the asymptotic form for the Hankel functions,

$$\lim_{\rho \rightarrow \infty} H_0^{(1)/(2)}(k_n \rho) \sim \frac{e^{\pm i k_n \rho}}{\sqrt{k_n \rho}}, \quad (140)$$

(+ applies to (1) and – applies to (2)) and enforcing tangential field continuity, we find

$$\begin{aligned} |r_n| &= \left| \frac{a_n k_{n+1} - a_{n+1} k_n}{a_n k_{n+1} + a_{n+1} k_n} \right| \\ &= \left| \frac{\cos(\theta_{n+1}) - \cos(\theta_n)}{\cos(\theta_{n+1}) + \cos(\theta_n)} \right|, \end{aligned} \quad (141)$$

for  $n = 0$  to  $N_{cyl} - 1$ .  $\theta_n$  and  $\theta_{n+1}$  are the (complex) propagation angles with respect to  $\hat{n}_{\Gamma_S}$  in regions  $n$  and  $n + 1$ , respectively. We set  $|r_{N_{cyl}}| = 1$  to enforce the perfect conductor boundary condition at the mesh edge ( $\Gamma$ ). Keeping only the first (lowest order) term in the derivatives of (140), we approximate

$$t_{1,2,\dots,n} = t_1 t_2 \dots t_n, \quad (142)$$

where

$$t_n \equiv e^{-i 2 k_n l_n}, \quad (143)$$

and  $k_n$  and  $l_n \equiv \rho_n - \rho_{n-1}$  are the radial propagation constant and cylinder thickness in region  $n$ . Substituting (141) – (143) into (139) and taking the magnitude yields,

$$|r| \approx \left| \sum_{n=0}^{N_{cyl}} |r_n| \prod_{\hat{n}=0}^n e^{-i2k_{\hat{n}}l_{\hat{n}}} \right|, \quad (144)$$

which we may solve for a given  $a(\rho)$  to find  $|r(\theta_i)|$ , the magnitude of the total Fresnel reflection for a general (e.g., includes axial propagation  $\exp(i\beta z)$ ) cylindrical wave incident on the AL at angle  $\theta_i$ . Note that (144) is equivalent to the result obtained via a plane wave, planar interface analysis, and may therefore be directly applied to the *axial* AL design ( $\Omega_T$  and  $\Omega_B$ ), in addition to the radial design ( $\Omega_S$ ).

To finalize our radial AL design we use a  $2 \times 2$  transfer matrix solution for the TE or TM fields. Enforcing continuity of (131) and (134), *or* (132) and (133) at each radial interface  $\rho_n$ , we have

$$L_n \begin{bmatrix} A_n \\ B_n \end{bmatrix} = R_{n+1} \begin{bmatrix} A_{n+1} \\ B_{n+1} \end{bmatrix}, \quad (145)$$

where

$$L_n \equiv \begin{bmatrix} H_0^{(2)}(k_n \rho_n) & H_0^{(1)}(k_n \rho_n) \\ \frac{a_n}{k_n} H_1^{(2)}(k_n \rho_n) & \frac{a_n}{k_n} H_1^{(1)}(k_n \rho_n) \end{bmatrix}, \quad (146)$$

and

$$R_{n+1} \equiv \begin{bmatrix} H_0^{(2)}(k_{n+1} \rho_n) & H_0^{(1)}(k_{n+1} \rho_n) \\ \frac{a_{n+1}}{k_{n+1}} H_1^{(2)}(k_{n+1} \rho_n) & \frac{a_{n+1}}{k_{n+1}} H_1^{(1)}(k_{n+1} \rho_n) \end{bmatrix}. \quad (147)$$

We have dropped the  $\text{pol}=\text{TE}/\text{TM}$  superscript since (145) holds for both polarizations. At the mesh boundary ( $\Gamma$ ), we enforce  $E_\phi = 0$  which relates the coefficients in the outermost AL cylinder by

$$A_{N_{cyl}} = -B_{N_{cyl}} \frac{H_1^{(1)}(k_{N_{cyl}} \rho_{N_{cyl}})}{H_1^{(2)}(k_{N_{cyl}} \rho_{N_{cyl}})}. \quad (148)$$

For convenience, we choose  $A_{N_{cyl}} = -H_1^{(1)}(k_{N_{cyl}} \rho_{N_{cyl}})$  and  $B_{N_{cyl}} = H_1^{(2)}(k_{N_{cyl}} \rho_{N_{cyl}})$ . Beginning in the outer AL cylinder and working inward via repeatedly applying (145), we calculate  $A_0$  and  $B_0$ . The total Fresnel reflection coefficient for an outward propagating wave incident on the AL is given by

$$|r| = \left| \frac{B_0}{A_0} \right|. \quad (149)$$

To design our AL, we ran the analysis outlined previously with VCSEL material parameters  $\varepsilon_r = 9$  and  $\mu_r = 1$ . We assumed a polynomial form for the AL loss function,

$$b(\chi) \equiv \sum_{i=1}^{\text{order}} \tilde{b}_i \chi^i. \quad (150)$$

Here order refers to the polynomial order,  $\tilde{b}_i$  are the polynomial coefficients, and

$$\chi \equiv \frac{\rho - \rho_{\Gamma_S}}{\rho_{\Gamma} - \rho_{\Gamma_S}} \quad (151)$$

is the normalized radial coordinate ranging from 0 at  $\Gamma_S$ , the VCSEL–AL interface, to 1 at  $\Gamma$ , the problem/mesh boundary. Through a numerical optimization, we found that a second order polynomial with coefficients,

$$\tilde{b}_1 = 0.1178, \quad (152)$$

$$\tilde{b}_2 = 0.7433, \quad (153)$$

worked best for  $b(\chi)$ . In addition, we found an AL thickness of  $1.5\lambda$  (at  $\lambda = 870$  nm) was superior, with little change in the AL properties for greater thicknesses. The reflection coefficient (calculated with the transfer matrix approach) verses angle is given in Fig. 38. The key point to recognize from Fig. 38 is the intensity reflection,  $R_{dB} \equiv 20 \log_{10}(|r|) \leq -50$  dB for  $\theta_i \leq 40^\circ$ , indicating a good “wide-angle” absorber design.

To provide a more practical test of our AL design, we analyzed the  $1\lambda$  –1THIN VCSEL (previously described), tracking the lasing mode (defined as the lowest loss mode, e.g., the mode with the smallest  $\text{Im}(\xi)$ ) eigenvalue as a function of  $\rho_{\Gamma_S} - \rho_{ox}$ , which is the separation between the VCSEL–AL boundary and the oxide aperture. We tested two different oxide aperture radii,  $0.5 \mu\text{m}$  and  $1.0 \mu\text{m}$ , using our  $1.5\lambda$  ( $= 0.435 \mu\text{m}$ ), second order polynomial AL design. The resulting real and imaginary parts of the eigenvalues converge for  $\rho_{\Gamma_S} - \rho_{ox} \geq 0.9 \mu\text{m}$  (corresponding to  $\approx 3\lambda$ ), denoting the minimum allowable separation between the oxide aperture and  $\Gamma_S$ . It is interesting to note that for the  $1.0 \mu\text{m}$  oxide aperture, the variation in the eigenvalue from  $\rho_{ox} = 1.2 \mu\text{m}$  to  $2.0 \mu\text{m}$  corresponds to a variation in the resonant wavelength of less than two angstroms, implying that the AL works well even when placed very close to the aperture. No analogous test was performed on the axial AL design; we assume that, based on the good results of the radial AL design and the high reflectance of the oxide DBRs, the optimized radial AL design should work for the axial AL as well. To perform the lasing mode analysis, we used  $\rho_{\Gamma_S} = 2.0 \mu\text{m}$  and varied the oxide aperture radius ( $\rho_{ox}$ ) from  $0.4 \mu\text{m}$  to  $1.0 \mu\text{m}$ .

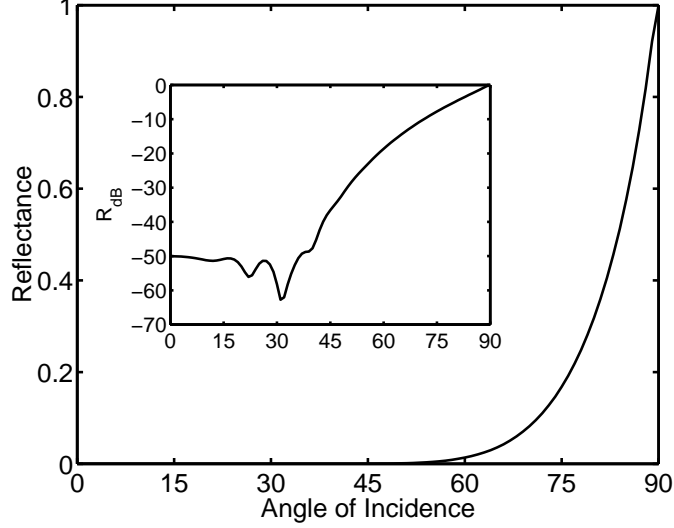


FIG. 38: Calculated intensity reflection  $R \equiv |r|^2$  of the radial absorbing layer (AL) using the rigorous transfer matrix approach. The calculation is based on a  $1.5\lambda$  thick AL at 870 nm, positioned with  $\rho_{\Gamma_S} = 2.0 \mu\text{m}$ . Thirty layers were used to discretize the AL loss function. Inset is the intensity reflection in decibels  $R_{dB} \equiv 20 \log_{10}(|r|)$ .

### Comparison of WIMP and VFEM to Published Results

In this section, we present detailed comparison and results when both the weighted index method and the vector finite element method simulations are applied to two structures found in the literature. The goal here is not only to calibrate and/or validate each model to known results, but also to examine the individual strengths and shortcomings of each model. As a *quasi-exact* approach, we expect the VFEM to give superior results for all investigated parameters (resonant wavelength, transverse confinement factor, diffraction losses, etc...). Nevertheless, the computation time and problem setup may make this method unattractive for a number of applications, and therefore this comparison of the two methods is warranted.

We computed the resonant wavelength, threshold gain, and transverse confinement factor as a function of oxide aperture radius for four variations of VCSEL structures grown, fabricated, and tested by Professor Y.-H. Lee's research group at the Korea Advanced Institute of Science and Technology (KAIST)[51, 52]. It can be seen from Fig. 39 that the eigenmode resonances match very well for each structure. The WIMP results deviate by a uniform translation in wavelength by  $\approx 2\text{nm}$ . This shift may be due to the difference in

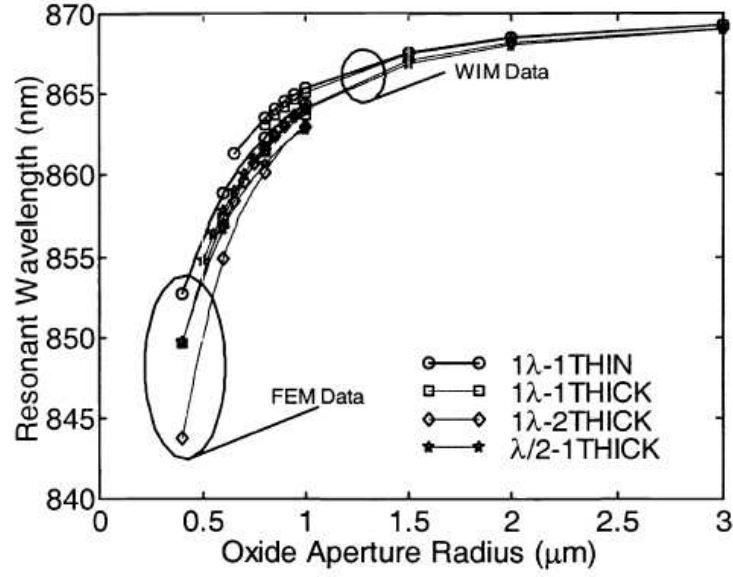


FIG. 39: Comparison of the resonant wavelength calculated using the WIMP and VFEM methods for the four variations of the KAIST VCSEL described in Refs.[51, 52].

how the VCSELs are represented in this versus the VFEM. Such small discrepancies can easily be attributed in how the material layer thicknesses or indices of refraction are handled in these codes. The threshold gain (Fig.40) shows much larger discrepancies, however. Indeed, the WIMP values for  $g_{th}$  deviate by roughly  $2\times$  the values of the reference VFEM results for all three  $1\lambda$  cases. The  $\lambda/2$  thick cavity results are even worse, with the wrong *trend* even occurring: the WIMP has the  $\lambda/2$  case having the highest value of  $g_{th}$ , while the VFEM demonstrates the experimentally validated case of such cavities having lower threshold. This lack of agreement could be partially explained by the fact that this VCSEL structure stretches the limits of the assumption of separability upon which the WIMP formalism is based. More realistically, however, is a fundamental problem in how the diffraction losses are calculated in WIMP. Finally, the transverse confinement factor,  $\Gamma^{tr}$ , is displayed for these structures in Fig.41. From this figure, it is evident that both models agree very well. In total, then, the WIMP is seen to give reasonable results (and certainly good *qualitative trends*!) for predicting  $\lambda$  and  $\Gamma$ , but parasitic mode coupling is still an issue of further research.

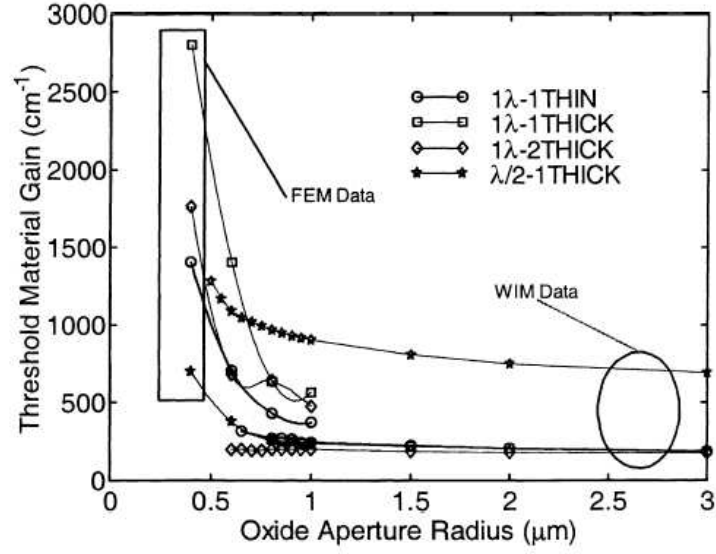


FIG. 40: Comparison of threshold gain calculated using the WIMP and VFEM methods for the four variations of the KAIST VCSEL described in Refs.[51, 52].

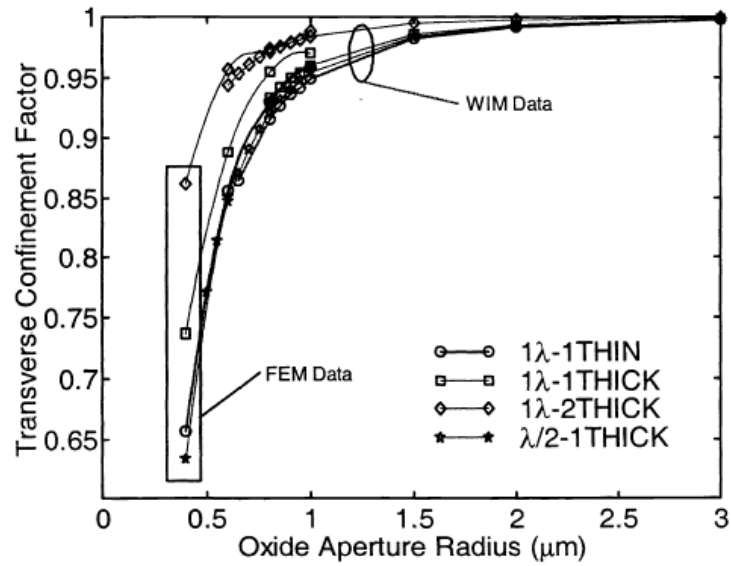


FIG. 41: Comparison of the transverse confinement factor calculated using the WIMP and VFEM methods for the four variations of the KAIST VCSEL described in Refs.[51, 52].

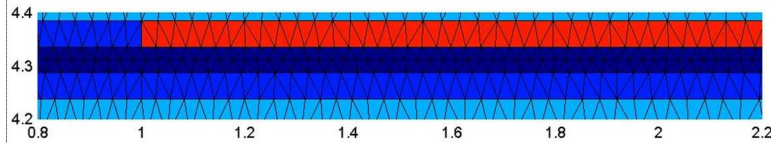


FIG. 42: Sample VFEM meshing of the “blunt” aperture region in an oxide-apertured VCSEL.

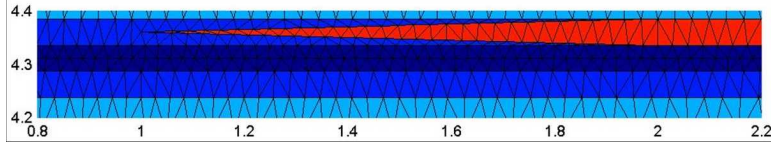


FIG. 43: Sample VFEM meshing of the tapered aperture region in a theoretical oxide-apertured VCSEL.

### VFEM Applied to Tapered Oxide Apertures

As shown in the previous section, the VFEM has proven to give superior results for diffraction losses occurring in a variety of structures when compared to the WIMP method. With its basis in the finite element method, this VFEM code is also able to handle structures that WIMP simply *cannot*, namely devices having more structure in the radial geometry. One example of such a device is a tapered-oxide-aperture VCSEL. A VFEM meshing of a traditional “blunt” oxide aperture structure is shown in Fig.42, while that for a tapered structure is shown in Fig.43. Although simulation of a structure like this might seem contrived, nothing is further from the truth. Indeed, it is possible to *force* tapering of such structures simply by varying the mole fraction of aluminum in the aperture’s  $\text{Al}_x\text{Ga}_{1-x}\text{As}$  layers from, say,  $x = 0.95$  to  $x = 1.00$ , which can be done either through mass flow controller operations in the case of MOCVD growth, or by digital alloying techniques[53].

The structures under investigation are a  $\lambda/2$ -cavity VCSEL based on a design from the University of Texas (henceforth denoted “UT”)[54], and a  $4 - \lambda$ -cavity VCSEL design generated at the University of Southern California (denoted hereon as “USC”)[55]. The UT structure has a single  $\text{In}_x\text{Ga}_{1-x}\text{As}$  QW gain source, and employs AlAs - GaAs bottom DBR mirrors (26 pairs) as well as post-growth-deposited dielectric mirrors (6 pairs of ZnSe - MgF). A schematic representation of the layer structure is shown in Fig.44, and a plot of the theoretical index of refraction and standing wave intensity profile is demonstrated in Fig.45.

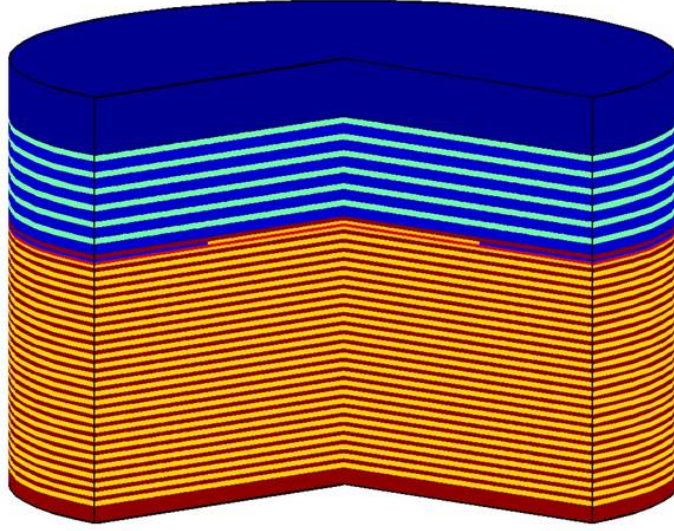


FIG. 44: Schematic representation of the “UT” short-cavity VCSEL under investigation.

Oxide apertures, nominally 396 Å thick on either side of the QW, occur at positions *midway* between the cavity standing wave nodes and anti-nodes. In contrast, the USC “long-cavity” structure is comprised of all-semiconductor mirror layers surrounding the  $4\text{-}\lambda$ -thick optical cavity. The structure has a single 300 Å oxide aperture centered on the standing wave peak (anti-node), above the QW active region. Fig.46 demonstrates the schematic representation and Fig. 47 standing wave fields for this structure, respectively.

For each of these structures, we computed the transverse confinement factor ( $\Gamma^{tr}$ ), the diffraction rate, the field distribution ( $E_\phi$ ), and the threshold material gain ( $g_{th}$ ) with respect to oxide aperture taper length (see Fig. 43). For each case, this variation was computed for three different inner oxide-aperture radii: 1, 2, and 3  $\mu\text{m}$ . For each of these radii, the taper length was then varied from 0  $\mu\text{m}$  (“blunt” aperture), to 3  $\mu\text{m}$ , in 1- $\mu\text{m}$  increments. Additionally, the oxide aperture thickness was kept constant, and only the taper length was varied, synonymous with “longer apertures are sharper.”

Results for calculation of the transverse confinement factor for both the USC and UT designs as a function of aperture taper length are shown in Figs. 48 and 49. As the taper length is increased, the volume of low index material in the vicinity of the VCSEL core decreases. This results in a reduction of the effective index[10] contrast between core and



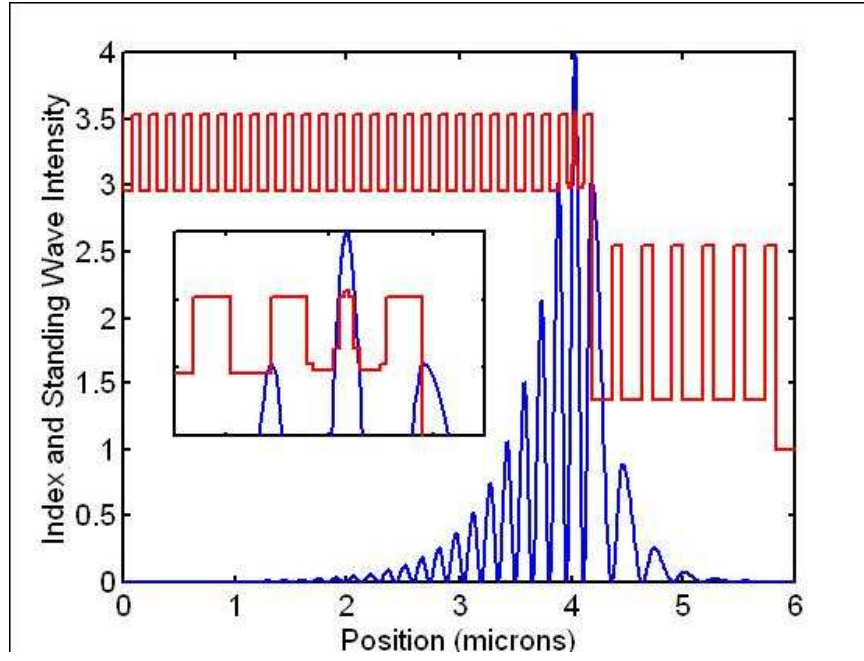


FIG. 45: Theoretical plot of the “UT” short-cavity VCSEL standing wave fields and refractive index profile.

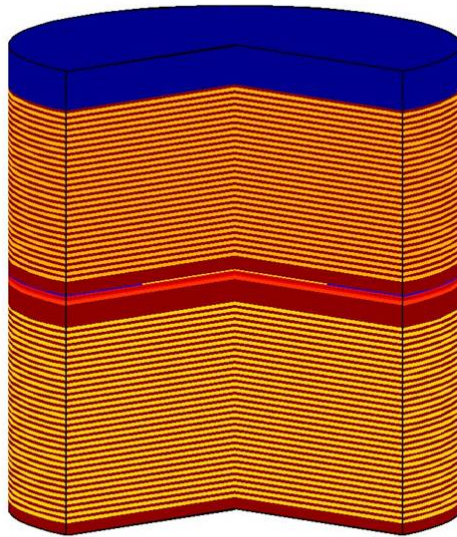


FIG. 46: Schematic representation of the “USC” long-cavity VCSEL under investigation.

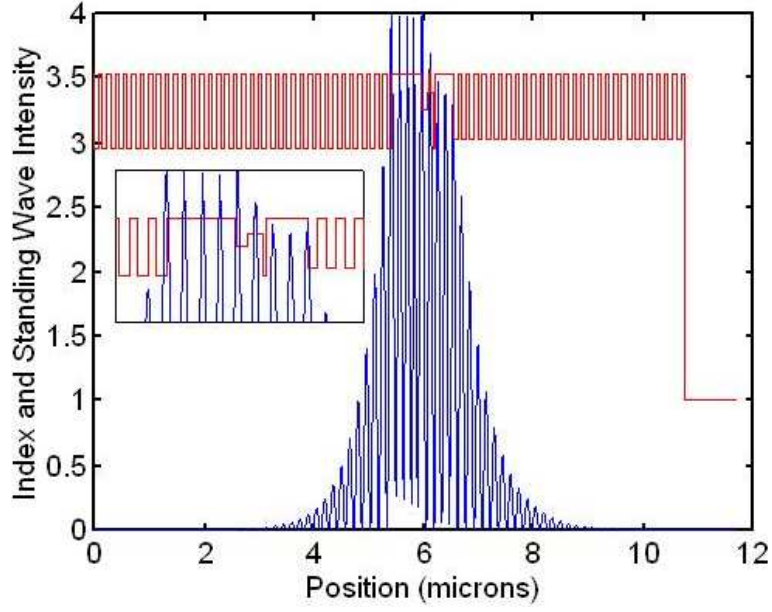


FIG. 47: Theoretical plot of the “USC” long-cavity VCSEL standing wave fields and refractive index profile.

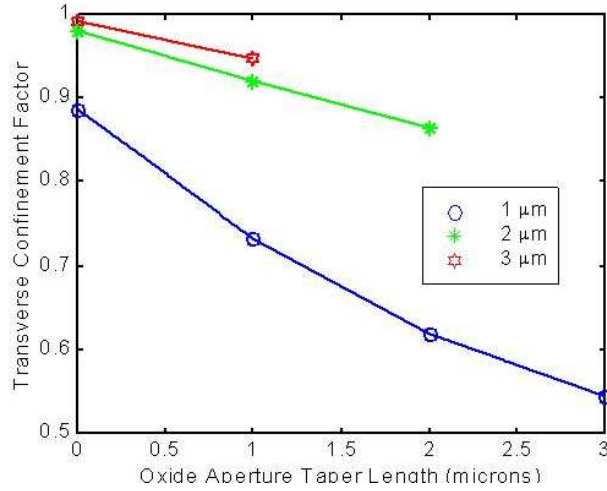


FIG. 48: Plot of  $\Gamma^{tr}$  as a function of oxide aperture taper radius for the UT structure. *Note:* This calculation assumes uniform gain over the aperture cross-section.

cladding regions. Consequently, the mode spreads out spatially, and  $\Gamma^{tr}$  diminishes. In lesson, the smaller the oxide aperture’s inner radius, the more pronounced are the effects of giving the aperture a tapered shape.

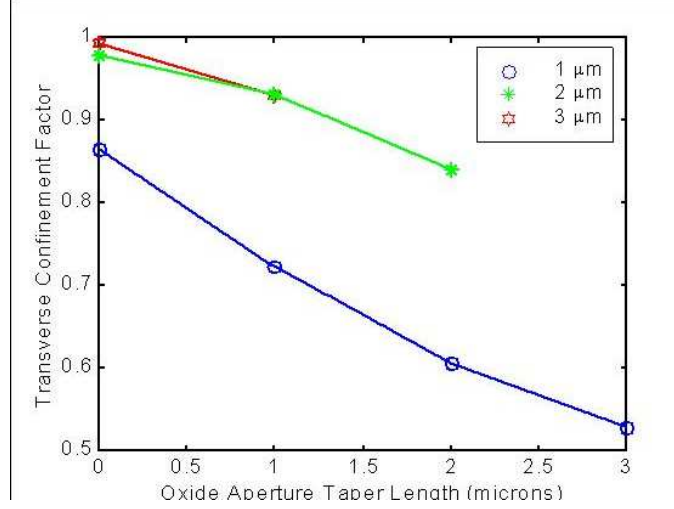


FIG. 49: Plot of  $\Gamma^{tr}$  as a function of oxide aperture taper radius for the USC structure. *Note:* This calculation assumes uniform gain over the aperture cross-section.

If we define the “diffraction rate” as the percentage of optical mode energy that is scattered or emitted radially out the side of the VCSEL, then we can compute the relative merits of tapering an oxide aperture toward unwanted contributions in effective diffractive losses. The diffraction rate as defined in this manner is plotted in Fig. 50 for the UT structure, and in Fig. 51 for the USC design. It is seen that tapering the aperture significantly reduces diffraction losses in both designs, and for all cases (all values of inner oxide aperture radius). Based on the results for these two disparate structures, reasons for this can be inferred in the following ways. As mentioned previously, more tapering leads to great spatial spreading of the mode. A resultant flatter wavefront naturally suffers less diffraction. As discussed by Hegblom and co-workers[11, 56], tapering of an aperture serves to give it a lens-like quality, which in turn re-focuses the mode and counters diffraction. Also per the Hegblom model, the symmetric taper in this structure produces a linear phase shift as a function of radial position, giving the element a lens with a linear profile. As a result, increasing the taper length beyond 1  $\mu\text{m}$  is seen to further reduce diffraction in the USC structure, but it has no appreciable further effect in the UT device.

As the USC cavity length is nearly double that of the UT design, the longer focal length lensing from longer tapering better matches the USC cavity, significantly reducing diffraction losses in this structure compared to the UT design. The mode of the UT VCSEL is best

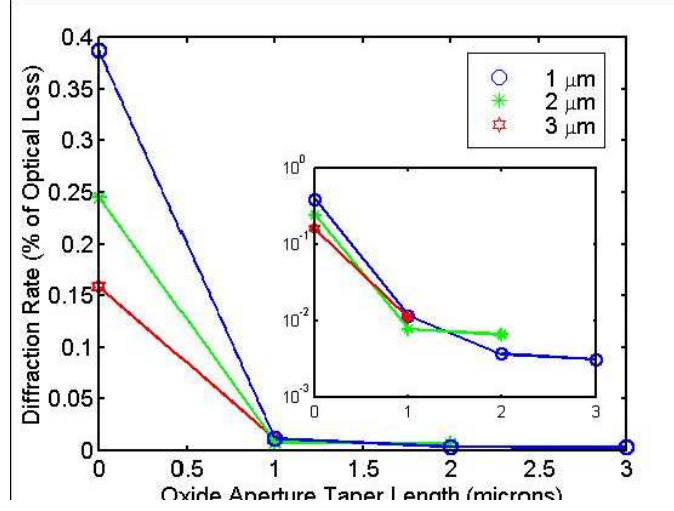


FIG. 50: Plot of “diffraction rate” (see main text) as a function of oxide aperture taper radius for the UT structure. The inset shows a blow up for longer taper lengths, demonstrating how slight the change in diffraction rate becomes for increased taper lengths *Note*: Each curve corresponds to a different value of oxide aperture inner radius.

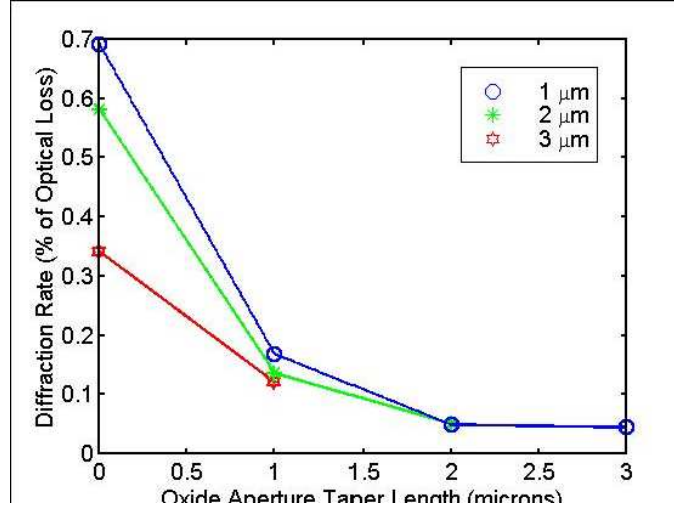


FIG. 51: Plot of “diffraction rate” (see main text) as a function of oxide aperture taper radius for the USC structure. *Note*: Each curve corresponds to a different value of oxide aperture inner radius.

suited for the 1  $\mu\text{m}$  tapers, and further reductions are *slight* if at all.

Perhaps the most dramatic visualization of the influence of tapered versus blunt oxide

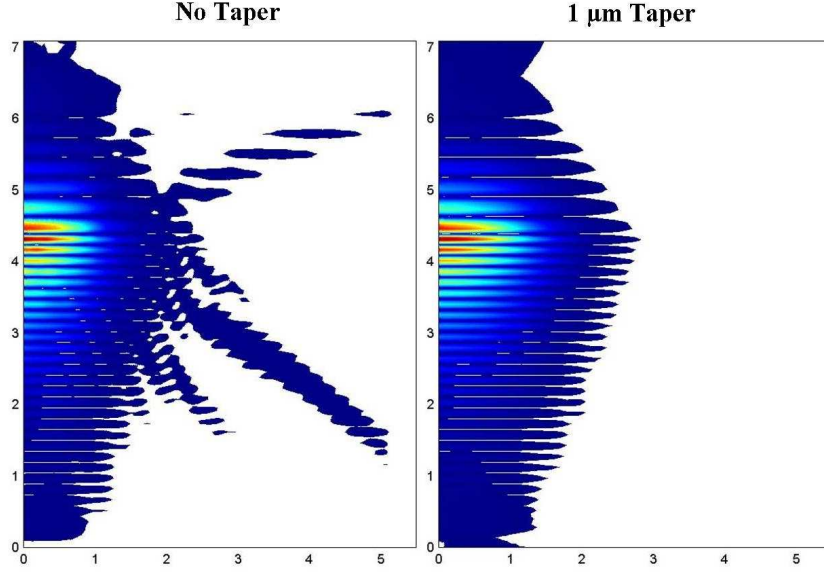


FIG. 52: Intensity plot of the field distribution  $E_\phi$  for the UT structure. On the left, the device as simulated with no tapering of the aperture. On the right, with a 1  $\mu\text{m}$  taper. Note the radial “fingers” showing the effects of diffraction from the blunt aperture.

apertures can be seen when we examine the electric fields in such devices. In Figs. 52-53 are plotted the field distributions of the optical field  $E_\phi$  for the UT and USC structures, respectively. For the UT structure, one sees significant scattering of the field from the oxide aperture, giving rise to significant energy losses when no aperture is included. Similarly, the “blunt” aperture case of the USC structure is also evident. Indeed, with a little imagination, one can almost visualize the reflection of this diffracted energy off of the top boundary surface (at 10  $\mu\text{m}$  on the vertical axis) back into the VCSEL as a potential guided mode.

Finally, we show the threshold material gain ( $g_{th}$ ) required to exactly offset optical losses in Fig. 54 (UT structure) and Fig. 55 (USC structure). This includes not only the effects of gain-to-mode spatial overlap, but also takes into account transverse mode confinement effects and diffraction losses, as shown above. For these results, we have assumed a uniform gain distribution over the cross-section of the aperture. This is not unreasonable in that one of the early motivating factors for the use of such aperture was in current confinement or guiding in transistor type devices. In a typical design mindset, for maximizing mode-to-gain interactions, the optical field should be sharply peaked at the cavity center. However, as the VFEM has demonstrated, the more concentrated this mode is, the more it can

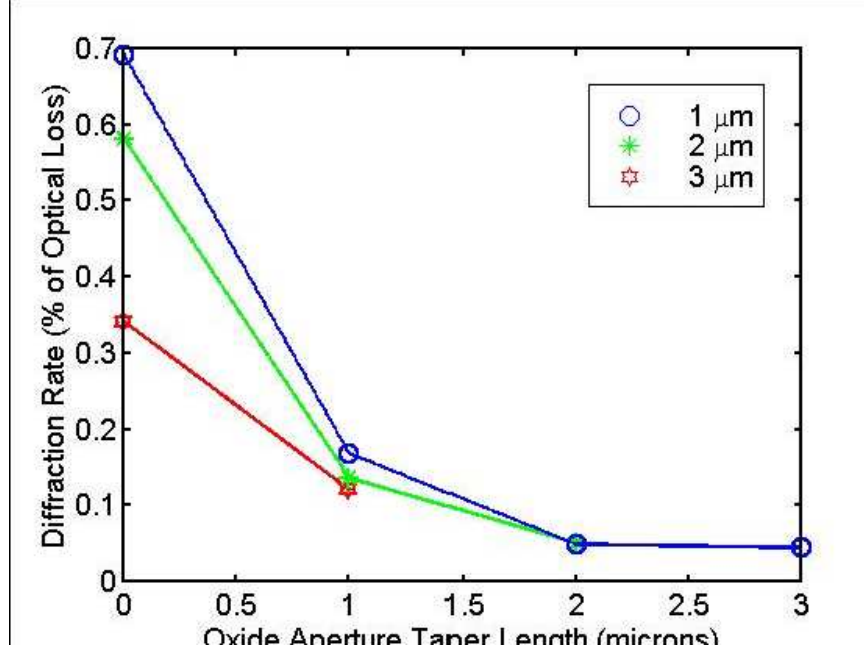


FIG. 53: Intensity plot of the field distribution  $E_\phi$  for the USC structure. On the left, the device as simulated with no tapering of the aperture. In the middle, a 1  $\mu\text{m}$  taper. On the right, a 3  $\mu\text{m}$  taper. Again, the radial “fingers” indicate diffraction from the blunt aperture, with possible reflection back into the structure at the semiconductor/air interface at 10  $\mu\text{m}$  on the vertical axis.

potentially diffract, and hence there exists an underlying overlap versus diffraction tradeoff consideration in optimizing a given design concept. Indeed, it is evident in the calculations for  $g_{th}$  for the UT structure that increasing the oxide taper eventually leads to increased  $g_{th}$ , which is explained as an eventual loss of optical confinement losing out to diffractive losses in such a design.

### Generalized Interface Approach for Exact Design in Graded Interface Distributed Bragg Reflectors

In this subsection, we introduce the concept of a *generalized interface*, and demonstrate how such a construct allows us to design high reflectivity distributed Bragg reflection mirrors (DBRs) by exactly phase matching the reflectance in layers that include arbitrary grades. The resulting generalized phase matching constraints depend upon the phase angles of the reflection and transmission coefficients for these grade layers, and we show the method for

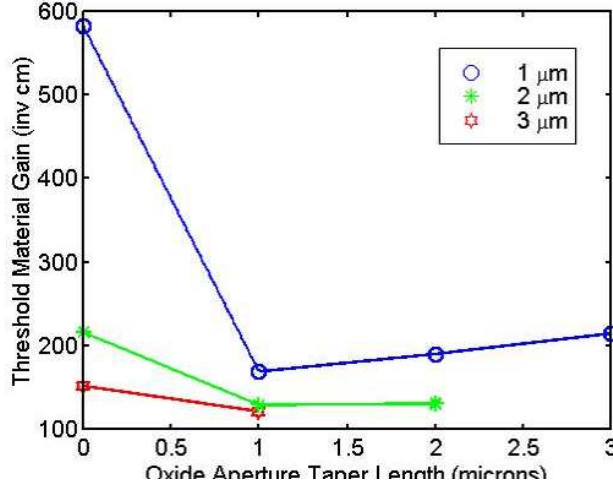


FIG. 54: Threshold material gain,  $g_{th}$ , for the UT structure. Each curve is for a different oxide aperture inner radius, and we have assumed uniform material gain distribution over the oxide aperture.

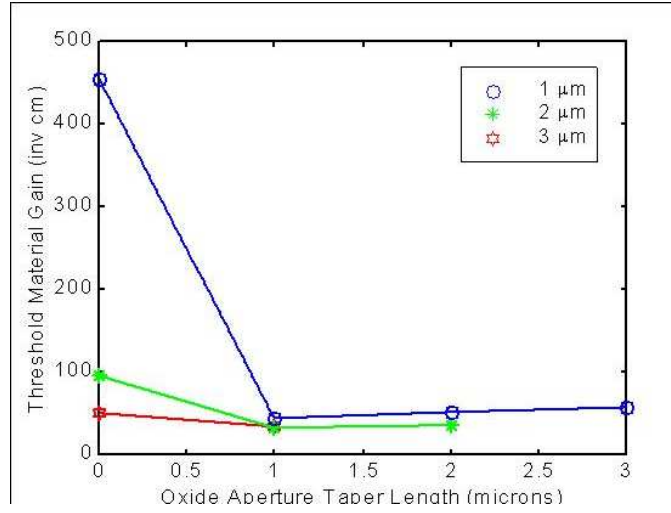


FIG. 55: Threshold material gain,  $g_{th}$ , for the USC structure. Each curve is for a different oxide aperture inner radius, and we have assumed uniform material gain distribution over the oxide aperture.

calculating these phases to arbitrary precision either analytically (for a certain set of grade profiles) or numerically (for arbitrary profiles).

The importance of this effort follows from the fact that the use of graded layers instead

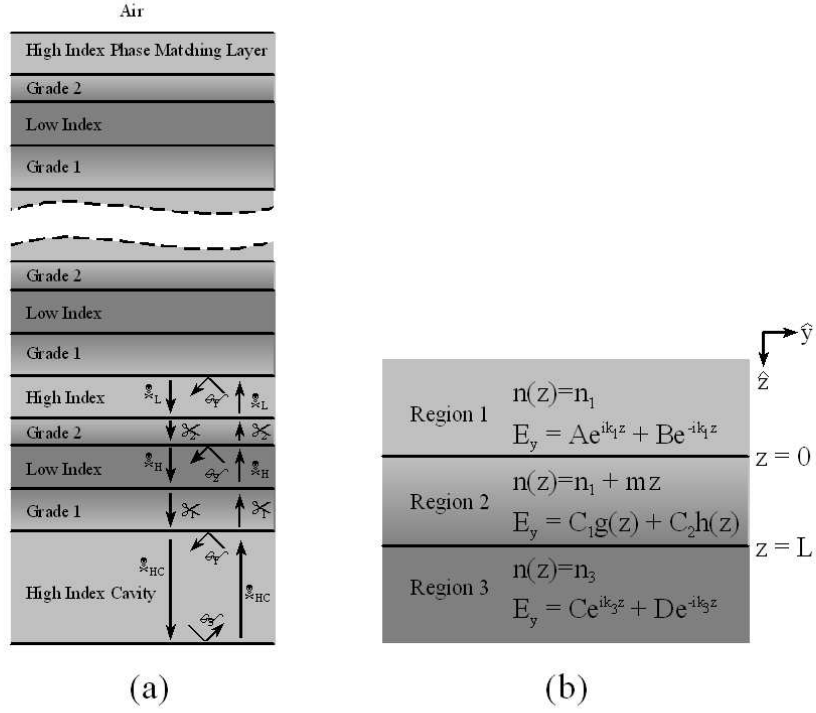


FIG. 56: a) Diagram of a periodic mirror structure with the various phase terms illustrated. b) Coordinate system and basis functions for the electric field for a section of the mirror.

of abrupt interfaces has been demonstrated to significantly reduce the voltage required to drive current through DBR mirrors. In the question for low-threshold lasers, then, such graded layer mirrors are rapidly becoming the norm, and a correct understanding of the optical principles necessary for microcavity resonance aligned to the active region's material gain peak is required to reach these ultimate low-threshold limits.

For a multilayer mirror to have high reflectivity, the individual mirror layers must be designed in such a manner as to insure that the reflections from every layer constructively interfere. This is most easily realized by ensuring that the phase change accrued by the field propagating in a round-trip from one graded layer to the next is equal to a multiple of  $2\pi$ . Figure 56 illustrates a periodic mirror structure, and shows the phase terms associated with the various layers.

The phase of the reflection off the first graded layer is denoted by  $\beta_1$ . The phase matching condition for the second graded layer is then:



$$\beta_1 + 2\pi k = \alpha_1 + \phi_H + \beta_2 + \phi_H + \alpha_1 \quad k = 1, 2, \dots \quad (154)$$

Here  $\beta_2$  is the phase for reflection off the second graded layer,  $\alpha_1$  is the phase for transmission through the first graded layer, and  $\phi_H$  is the phase for transmission through the constant high index layer. The phase for constant high index ( $n_H$ ) and low index ( $n_L$ ) layers of thickness  $d_H$  and  $d_L$  is simply given by:

$$\phi_H = \frac{2\pi n_H d_H}{\lambda}, \quad \phi_L = \frac{2\pi n_L d_L}{\lambda} \quad (155)$$

The phase matching condition for the next graded layer is:

$$\beta_2 + 2\pi l = \alpha_2 + \phi_L + \beta_1 + \phi_L + \alpha_2 \quad l = 1, 2, \dots \quad (156)$$

The transmitted and reflected phase terms  $\alpha$  and  $\beta$  are determined from the graded layer designs, and will depend in general on the index profile and thickness of the grades. It is possible by recursion to show that equations (154) and (156) ensure phase matching for every reflection, and that they are sufficient to determine both  $\phi_H$  and  $\phi_L$ , and thus the thickness, of both the high index and low index layers for a given graded layer design. The corresponding (minimum) thicknesses are:

$$d_H = \frac{\lambda (2\pi + \beta_1 - \beta_2 - 2\alpha_1)}{4\pi n_H} \quad (157)$$

$$d_L = \frac{\lambda (2\pi + \beta_2 - \beta_1 - 2\alpha_2)}{4\pi n_L} \quad (158)$$

where  $\lambda$  is the operating wavelength. The designs of the graded layers are typically determined by the desired electronic transport through the mirror, with the constant index layers providing the proper optical thicknesses.

In addition to designing the layers inside the mirror stack, it is also necessary to have a proper thickness for the layers that terminate the mirror. In the case of a VCSEL, the mirror would be terminated on one side by the cavity layer, and on the other side by either air or the substrate, depending on whether the mirror is the top mirror or the bottom mirror. For a bottom mirror, the form of the phase matching equation remains the same as equation (154), but the value of the reflected phase term  $\beta_1$  may or may not remain the same depending

on whether or not the high index mirror layers are composed of the same material as the substrate. For a top mirror, the value of  $\beta_1$  is zero (since no grade is necessary).

For the cavity, the condition for phase matching is that the round-trip phase of a wave resonating in the cavity is an integral multiple of  $2\pi$ . Thus, the phase matching condition is:

$$2\phi_{HC} + \beta_1 + \beta_3 = 2\pi m, \quad m = 1, 2, \dots \quad (159)$$

As mentioned previously, the values of the phase terms  $\alpha$  and  $\beta$  are determined by the particular choice of the graded layer index profile and thickness. A method for determining these values for linear index (composition) grading will be given in the next section.

The problem of graded DBR design has now been reduced to a calculation of the transmission and reflection phase angles  $\alpha$  and  $\beta$  for the graded layers. We obtain these angles from the transmission and reflection coefficients for propagation in the three region case illustrated in Fig. 56(b): the refractive index is constant in regions 1 and 3 with values  $n_1$  and  $n_3$ , respectively while region 2 is the grade. The refractive index varies approximately linearly with composition in the AlAs/GaAs[57] material system. If the desired composition grade is linear, then the index of refraction of the grade will have the form  $n(z) = n_1 + mz$  with  $z = 0$  at the interface between region 1 and region 2 and  $m \equiv (n_2 - n_1)/L$ . We limit ourselves to normal incidence (i.e. propagation along the  $z$  direction). Without loss of generality, we can assume that the electric field vector in regions 1 and 3 consists of only a  $\hat{y}$  component. In the constant-index regions, the field solutions are simply plane waves allowing us to write the general electric field in region 1 as  $E_y = Ae^{ik_1z} + Be^{-ik_1z}$  and in region 3 as  $E_y = Ce^{ik_3L} + De^{-ik_3L}$  where  $k_i = \frac{n_i\omega}{c}$  with  $\omega$  being the frequency and  $c$  the speed of light. To obtain the general solution in region 2 we must solve the sourceless, macroscopic Maxwell's equations with a spatially varying dielectric function. This produces three uncoupled scalar wave equations, one for each component of the electric field in the graded region. However, the fact that  $E = \hat{y}E_y$  in regions 1 and 3 along with the boundary conditions and the divergence condition  $\nabla \cdot \vec{E} = -\frac{1}{\epsilon(z)}\frac{\partial\epsilon}{\partial z}E_z$  will force  $E_x = E_z = 0$  inside region 2. We are left with the scalar wave equation for  $E_y$  given by

$$\frac{\partial^2 E_y}{\partial z^2} + \frac{\epsilon(z)\omega^2}{c^2}E_y = 0. \quad (160)$$

The general solution for  $E_y$  when the index of refraction varies according to  $\sqrt{\epsilon(z)} = n(z) = n_1 + mz$  is

$$E_y = C_1 \sqrt{\frac{n(z)}{m}} J_{\frac{1}{4}} \left( \frac{\pi n^2(z)}{\lambda m} \right) + C_2 \sqrt{\frac{n(z)}{m}} Y_{\frac{1}{4}} \left( \frac{\pi n^2(z)}{\lambda m} \right) \quad (161)$$

where  $J_{\frac{1}{4}}$  and  $Y_{\frac{1}{4}}$  are quarter-order Bessel functions of the first and second kind, respectively (see later details for geometric series expressions for  $J_{\frac{1}{4}}$  and  $Y_{\frac{1}{4}}$ ). Introducing the shorthand notation

$$g(z) = \sqrt{\frac{n(z)}{m}} J_{\frac{1}{4}} \left( \frac{\pi n^2(z)}{\lambda m} \right), \quad (162)$$

$$h(z) = \sqrt{\frac{n(z)}{m}} Y_{\frac{1}{4}} \left( \frac{\pi n^2(z)}{\lambda m} \right) \quad (163)$$

we can write the characteristic matrix  $M$  (ref. Born and Wolf [58]), which propagates the field  $E_y$  and its  $z$ -derivative from  $z = 0$  to  $z = L$ , as

$$M = \frac{1}{h(0)g'(0) - h'(0)g(0)} \begin{pmatrix} h(L)g'(0) - h'(0)g(L) & h(0)g(L) - h(L)g(0) \\ h'(L)g'(0) - h'(0)g'(L) & h(0)g'(L) - h'(L)g(0) \end{pmatrix} \quad (164)$$

where primes denote differentiation with respect to  $z$ .

Because the index is continuous at the grade boundaries, the  $\vec{E}$  and  $\vec{B}$  fields must be continuous there. For our solution this requires the continuity of  $E_y$  and its derivative. Applying the boundary conditions and using  $M$  to propagate  $E_y$  and its derivative across the grade, we can relate the fields in regions 1 and 3 according to

$$\begin{pmatrix} C e^{ik_3 L} + D e^{-ik_3 L} \\ ik_3 (C e^{ik_3 L} - D e^{-ik_3 L}) \end{pmatrix} = M \begin{pmatrix} A + B \\ ik_1 (A - B) \end{pmatrix}. \quad (165)$$

First we solve for transmission and reflectance coefficients for top-down incidence where  $A = 1$  and  $D = 0$ . This gives

$$t_t = \frac{C_t e^{ik_3 L}}{1 e^{ik_1 0}} = \frac{-2k_1}{-m_{11}k_3 - m_{22}k_1 + i(m_{12}k_1k_3 - m_{21})}, \quad (166)$$

$$r_t = \frac{B_t e^{-ik_1 0}}{1 e^{ik_1 0}} = \frac{m_{11}k_3 - m_{22}k_1 + i(m_{12}k_1k_3 + m_{21})}{-m_{11}k_3 - m_{22}k_1 + i(m_{12}k_1k_3 - m_{21})} \quad (167)$$

where the  $m_{ij}$  are the elements of  $M$  and we have used the fact that  $M$  is unimodular.

Now we solve for the coefficients with bottom-up incidence where  $D = 1$  and  $A = 0$  obtaining

$$t_b = \frac{B_b e^{-ik_1 0}}{1e^{-ik_3 L}} = \frac{2k_3}{m_{11}k_3 + m_{22}k_1 - i(m_{12}k_1k_3 - m_{21})}, \quad (168)$$

$$r_b = \frac{C_b e^{ik_3 L}}{1e^{-ik_3 L}} = \frac{m_{11}k_3 - m_{22}k_1 - i(m_{12}k_1k_3 + m_{21})}{m_{11}k_3 + m_{22}k_1 - i(m_{12}k_1k_3 - m_{21})}. \quad (169)$$

Note that  $k_1 t_b = k_3 t_t$  which implies that in the absence of absorption the transmitted phase is independent of propagation direction. From these relations, we obtain the desired phase angles  $\alpha$  and  $\beta$  by expressing the coefficients in exponential form as:

$$t_t = t_{t0} e^{i\alpha_1}, \quad r_t = r_{t0} e^{i\beta_1}, \quad t_b = t_{b0} e^{i\alpha_2}, \quad r_t = r_{b0} e^{i\beta_2}. \quad (170)$$

Figure 57 plots the various phase angles as a function of grade length for several popular material systems.

Once the phase angles for the desired grade thickness are known, the thicknesses of the constant index layers can be chosen using the phase matching conditions (equations (154) and (156)). The reflectivity spectrum of the complete structure can be calculated using the transfer matrix technique by using equation (164) for the graded layer.

For completeness, the fractional Bessel functions of the first and second kind can be evaluated using the following expressions:

$$J_\nu(x) = \sum_{k=0}^{\infty} \frac{(-1)^k \left(\frac{x}{2}\right)^{\nu+2k}}{k! \Gamma(\nu + k + 1)}, \quad Y_\nu(x) = \frac{J_\nu(x) \cos(\pi\nu) - J_{-\nu}(x)}{\sin(\pi\nu)} \quad (171)$$

The geometric series for  $J_{\frac{1}{4}}\left(\frac{\pi n^2(z)}{\lambda m}\right)$  converges within calculable error after ten or twenty terms for reasonable grade lengths and index values.

## GROWTH, FABRICATION, AND CHARACTERIZATION OF LOW-THRESHOLD VCSELS

In this section is detailed both the enhancements in core capability as well as results of our work in the creation of very-low threshold VCSELS. As mentioned in the introduction,

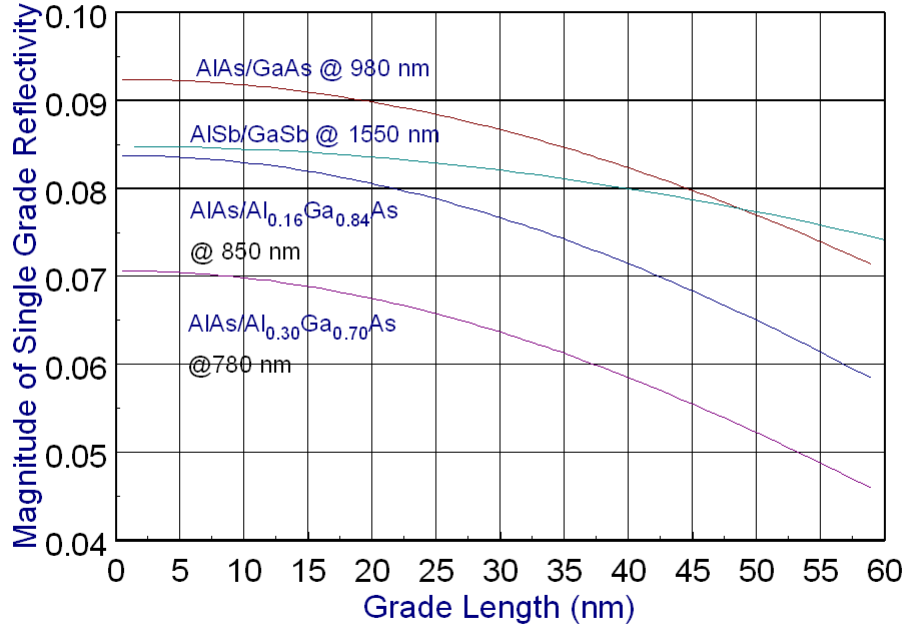


FIG. 57: Phase angle plots for several popular materials. a) AlAs/GaAs grade at 980 nm, b) AlAs/Al<sub>0.16</sub>Ga<sub>0.84</sub>As at 850 nm, c) AlAs/Al<sub>0.3</sub>Ga<sub>0.7</sub>As at 780 nm, d) AlSb/Al<sub>0.1</sub>Ga<sub>0.9</sub>Sb at 1550 nm

much of the initial effort of this project went into two main areas—improvements to modelling and simulations for correct designs, and then improvement to growth capabilities, which is the heart of any successful device-focused research.

### Growth Capability Development

Our initial forays into developing ultra-low threshold VCSELs began with growth of calibration structures, such as multiple quantum well (MQW) samples for determination of emission wavelength and photoluminescence (PL) intensity, and  $n$ - and  $p$ -doped DBR mirrors. The mirror growths served not only to calibrate the growth rates, when accompanied by fits of the accompanying reflection spectra, but also as a means of studying the conduction of current through the respective doped mirror structure.

Initially, our aim was to “walk before you run,” and we took the approach of attempting to demonstrate lasing in a conventional etched post, pump-through-the-mirrors VCSEL design before proceeding into state-of-the-art, very-low threshold, oxide-apertured, intracavity contacted designs.

During these initial stages, many growth issues and challenges facing the current MBE configuration became clear. For instance, the growth ovens and controllers were relatively unstable over the long times required for a VCSEL growth ( $\geq 14$  hours in typical cases). Indeed, reflection high-energy electron diffraction (RHEED) measurements taken prior to and after VCSEL growth showed significant discrepancies. At first, we attempted to correct this problem by adding optical monitors to the MBE system, and using fits to reflectance data at various stages in sample growth to correct for such growth rate drifts. The *Varian Gen II* MBE system used in this project is not readily adaptable for *in-situ* real-time monitoring of growth. However, this system does have affixed to it a sample preparation chamber used to load multiple wafers onto a wheeled substrate holder prior to an interlock connecting to the actual growth chamber. This intermediate chamber has optical viewports allowing the potential for reflection ( $R(\lambda)$ ) and photoluminescence ( $PL(\lambda)$ ) measurements while under high-vacuum conditions. In this way, we sought to break the growth of a VCSEL into stages—bottom mirror growth, growth of active region, and top mirror growth—and perform such *quasi-in-situ*  $PL(\lambda)$  and  $R(\lambda)$  measurements. The information from these spectra and resultant fits could then allow growth rate re-calibration without the need to load new RHEED samples into the chamber, and also without the need to break high-vacuum. Although this is not as useful as true real-time growth rate monitoring, it does significantly shorten the turnaround time and offer the opportunity for increased success for each growth run. Figure 58 shows an example of  $R(\lambda)$  and  $PL(\lambda)$  spectra measured for such an application. This figure shows that the fit values for  $\text{Al}_x\text{Ga}_{1-x}\text{As}$  and  $\text{GaAs}$  growth rates are 98.2% and 97.8% of the ideal rates, respectively. Also, this figure shows how the photoluminescence spectrum peaks near 971 nm, whereas the cavity dip measured after growth of the bottom mirror and active region of the VCSEL indicates a reflectivity “notch” at 967.3 nm, indicating relatively good alignment between gain peak and cavity resonance.

Although this ability of *quasi-in-situ* growth monitoring helped immensely, it was still far from allowing us to generate a working VCSEL. Two other significant enhancements to the

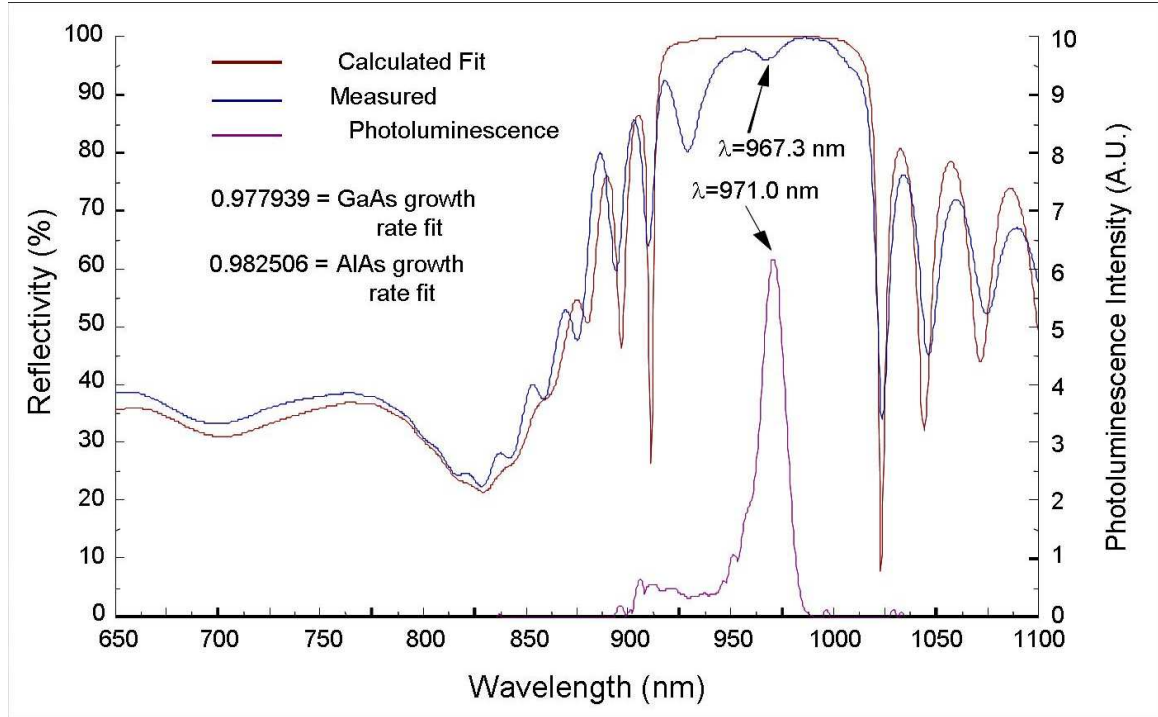


FIG. 58: Measured reflectivity and photoluminescence spectra for a VCSEL sample at various stages during growth. The red curve shows the calculated fit to only the bottom DBR spectrum (not shown); the blue curve is  $R(\lambda)$  for the DBR + active region, with an indicated cavity resonance at 967.3 nm; the magenta curve shows  $PL(\lambda)$  at this same stage in growth, with a peak at 971.0 nm, indicating suitable alignment of the gain to the cavity.

MBE tool were then performed. The first was a complete overhaul of the control code and machinery interfacing to the machine. In a sweeping re-vamp of this system, we replaced not only a host of convention growth effusion cells with larger capacity (400 g) *SUMO* cells from *EPI MBE Products*. The larger capacity cells not only would allow longer operation of the machine between re-filling of the cells, but were also demonstrated to be more stable for long-term growth operations. Along with the cells came a host of upgrades for the temperature controllers, and a new interfacing system (a *National Instruments FieldPoint Module*) to allow faster communications between a desktop computer system to all of the various controls of the MBE (including oven temperatures settings, shutter actuators, and substrate rotation control). The underlying software architecture for device growth was then separated into two elements of code. The first part was a *National Instruments LabView* interface control

starttable	
vcsl.def	
delay(100,as)	
repeat 41 times	
696 galas(si) "bottom mirror"	
812.69 alga2as(si) "bottom mirror"	
end	
608.74 galas(si) "oxide phase match layer"	
180 digitalgrade(galas(si),alga2as(si),steps=9) "grade up"	
superlattice(10,alga2as(si),40.18,alas(si),periods=13) "98% layer"	
180 digitalgrade(alga2as(si),galas(si),steps=9) "grade down"	
318.74 galas "note: setup carbon"	set(si,850)
delay(220,as) "cool down, arsenic up"	set(subst,510)
100 galas	
repeat 3 times	
delay(17,in,gal,as) "QW"	
100 galas "barrier"	
end	
delay(120,as) "arsenic down"	set(subst,600)
318.74 galas	
180 digitalgrade(galas(c),alga2as(c),steps=9) "grade up"	
superlattice(10,alga2as(c),40.18,alas(c),periods=13) "98% layer"	
180 digitalgrade(alga2as(c),galas(c),steps=9) "grade down"	
500 galas(c)	
repeat 31 times	
180 digitalgrade(galas(c),alga2as(c),steps=9)	
672.1 alga2as(c)	
180 digitalgrade(alga2as(c),galas(c),steps=9)	
520.57 galas(c)	
end	
180 digitalgrade(galas(c),alga2as(c),steps=9)	
672.1 alga2as(c)	
180 digitalgrade(alga2as(c),galas(c),steps=9)	
408.3 galas(c)	
200 galas(c)	
delay(600,as)	set(subst,100)
endtable()	

FIG. 59: Sample *Epitaxial Description Language* input deck for the instructions for growth of a 980-nm VCSEL via MBE.

code to perform all of the necessary hardware operations, including “graceful” shutdown of the system for maintenance. The second piece of control software, the so-called *Epitaxial Description Language (EDL)*, was a *Microsoft Visual C++* compiler code that renders text input from a *Microsoft Word* table into a series of commands capable of being read by the *LabView* code and summarily translated into machine operable instructions. This overhaul of the control software for the MBE system, although time consuming and laborious, resulted in an elegant and flexible “language” for growth of various structures by this system. An example of an *EDL* compiler code table for the growth of an entire VCSEL is demonstrated in Fig. 59. Examination of this input deck will show the inclusion of digital alloy grading in both the top *p*-doped DBR mirror, as well as to form high *Al* mole fraction oxide aperture layers.

The second major modification to this system was the inclusion of a carbon tetrabromide ( $\text{CBr}_4$ ) *p*-doping source. It has been found that the use of carbon as a *p*-doping source provides two main benefits: (1) the ability to dope at much higher concentrations



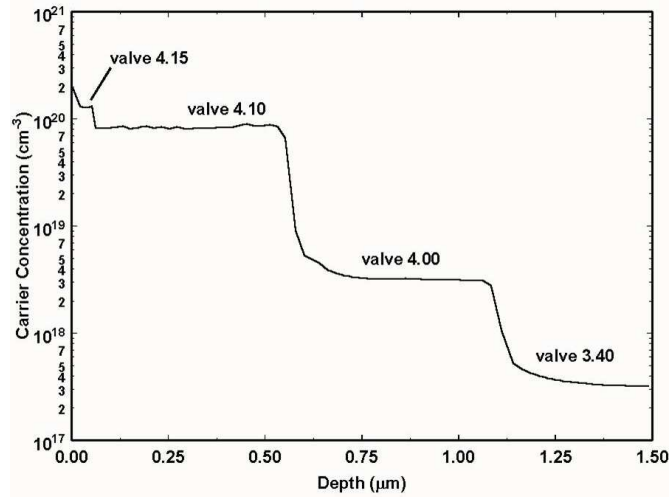


FIG. 60: Plot of activated dopant concentration versus depth in sample for a carbon-doped GaAs wafer.

( $\sim 10^{20} \text{ cm}^{-3}$ ), and (2) the fact that carbon as a  $p$ -type dopant does not diffuse nearly as much as more typical dopants, such as beryllium. In all, these combine to allow better tailored  $p$ -dopant profiles. As this flavor of dopant generally presents more material optical loss than  $n$ -dopants, one can readily see the advantages of being able to place heavily  $p$ -doped layers in regions of the optical cavity where the lasing mode field intensity is highest, and vice versa. Figure 60 shows a plot of activated dopant concentration versus depth in sample for a  $p$ -GaAs epitaxial growth. This was performed as a calibration sample to verify both our ultimate doping levels with this new oven, and also the control with valve position that this source enables.

### Processing Capability Development

The key processing steps for most semiconductor devices, after successful epitaxial growth, are typically (1) Deposition of metal contacts, (2) ability to etch various material with high fidelity, and (3) ability to isolate or passivate materials for profiled conduction of current through a device. This is equally true for VCSEL processing, but in our case, another key processing step includes the ability to perform selective oxidation in high aluminum mole fraction  $\text{Al}_x\text{Ga}_{1-x}\text{As}$  materials, the benefits of which has been previously discussed.

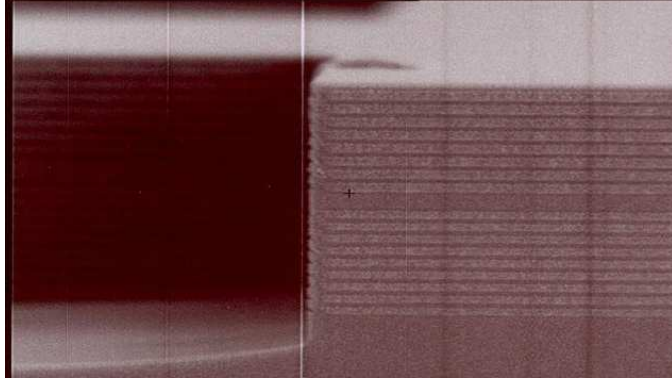


FIG. 61: SEM micrograph of an ICP/RIE etch of an AlAs-GaAs etalon structure. The individual layers comprising the top (8 periods) and bottom (8.5 periods) DBRs are clearly visible. Of note is the sidewall smoothness and anisotropic nature of the etch.

Ohmic contacts to standard III-V materials are well established, and we have made no effort to improve upon the voluminous amount of prior existing work. The reader may therefore reference any standard text on III-V material processing for suggested metal recipes for VCSEL fabrication. For our effort,  $p$ -metal deposition was typically Ti/Au or Ti/Pt/Au, whereas  $n$ -metal depositions were of the Ni/Ge/Au/Ni/Au variety.

For mesa etching, however, we employed a (then) state-of-the-art technology, inductively-coupled-plasma reactive ion etching (ICP/RIE), to perform mesa isolation and VCSEL device definition. The tool used was a *Plasma-Therm* (now *Unaxis*) model *SLR770* ICP/RIE system. This system is design etching a single wafer at a time, and is a loadlock system with 6 process gases. Our etch recipe used 30 sccm of  $\text{BCl}_3$  with 10 sccm of  $\text{Cl}_2$ , and the etch was done typically under the following tool conditions: pressure of 4 mTorr, wafer temperature of  $10^\circ \text{C}$ , utilizing 600 W of ICP power and 50 W of RIE power. Results from etching an “empty etalon” structure consisting of 8 periods of alternating top AlAs/GaAs DBR layers and 8.5 periods of bottom DBR layers with a  $1\text{-}\lambda$  GaAs etalon cavity layer are shown in Fig. 61. From this SEM micrograph, it is evident that we are obtaining very smooth and vertical sidewalls using this etch recipe. For sake of comparison, each alternating light (AlAs) and dark (GaAs) layer is comprising either mirror stack is nominally  $789 \text{ \AA}$  or  $696 \text{ \AA}$  thick, respectively.

Furthermore, in order to enable us to precisely control the etch depth, we outfitted this system with a homemade reflectance etch monitor system (Fig. 62). This system is

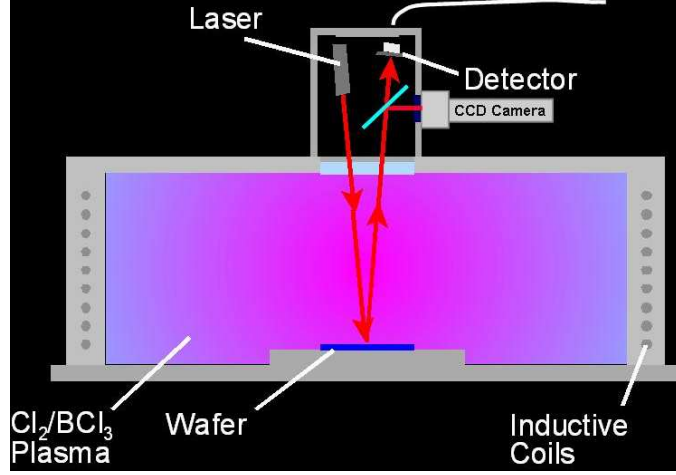


FIG. 62: Schematic cross section of the in-house ICP/RIE system, complete with custom-built reflectance monitoring system.

comprised of a laser diode (nominally  $\lambda_{laser} \approx 789 \text{ nm}$ ), a silicon photodiode detector, an imaging camera with laser line filter (to block all but a small portion of the laser diode signal, to prevent saturation during alignment), and a removable beamsplitter. The output of the photodiode is then sent to a desktop PC to collect the reflected signal as a function of time. The etch trace collected by this system for the sample shown in Fig. 61 is given in Fig. 63.

As an early demonstration of the powerful capability of this system, we processed VCSEL material grown by the *Army Research Laboratory, Sensors and Electron Devices Directorate* (at the time, under the direction of George Simonis). This *ARL* structure, denoted *ARL1236*, was an intracavity contacted device incorporating dual oxide apertures on either side of the gain region. Figure 64 shows our results in etching this sample. In this figure, the  $x$ -axis represents depth into the sample in  $\mu\text{m}$ , with the vertical axis plotting either the refractive index profile of the device, or the etch trace obtained from our etching system. The shaded areas represent the regions of top- or bottom-contact areas for this device, nominally  $\frac{3\lambda}{4n}$  thick, with  $\lambda$  the design wavelength (980 nm) and  $n$  the refractive index of the material. Also shown on this plot is the final etch profile of this device taken on a *Tencor P-10* stylus profilometer. This figure demonstrates our ability to etch device with the tight tolerances necessary to form intracavity contact VCSELs.

With our ability to etch samples and deposit Ohmic contacts, the final piece of the

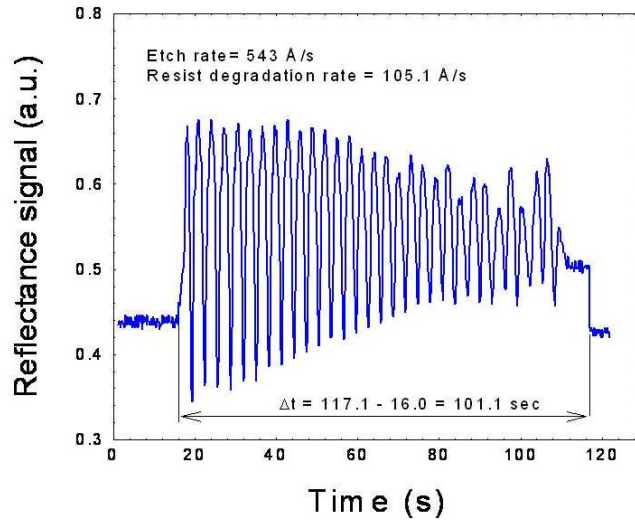


FIG. 63: Plot of reflected signal versus time for the etched sample of Figure 61.

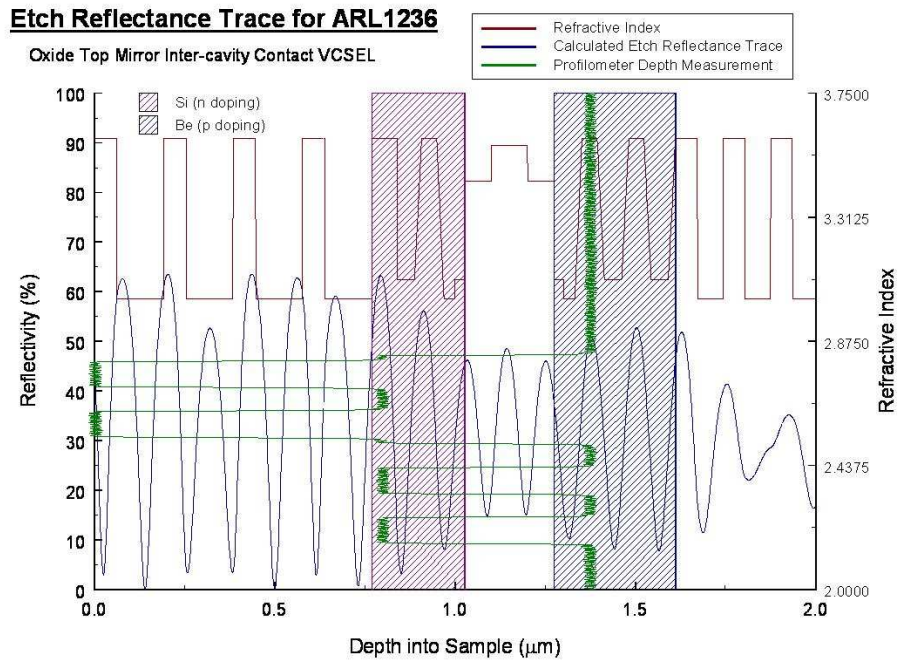


FIG. 64: Plot of reflected signal versus time for an intracavity contacted VCSEL grown by the Army Research Laboratory.

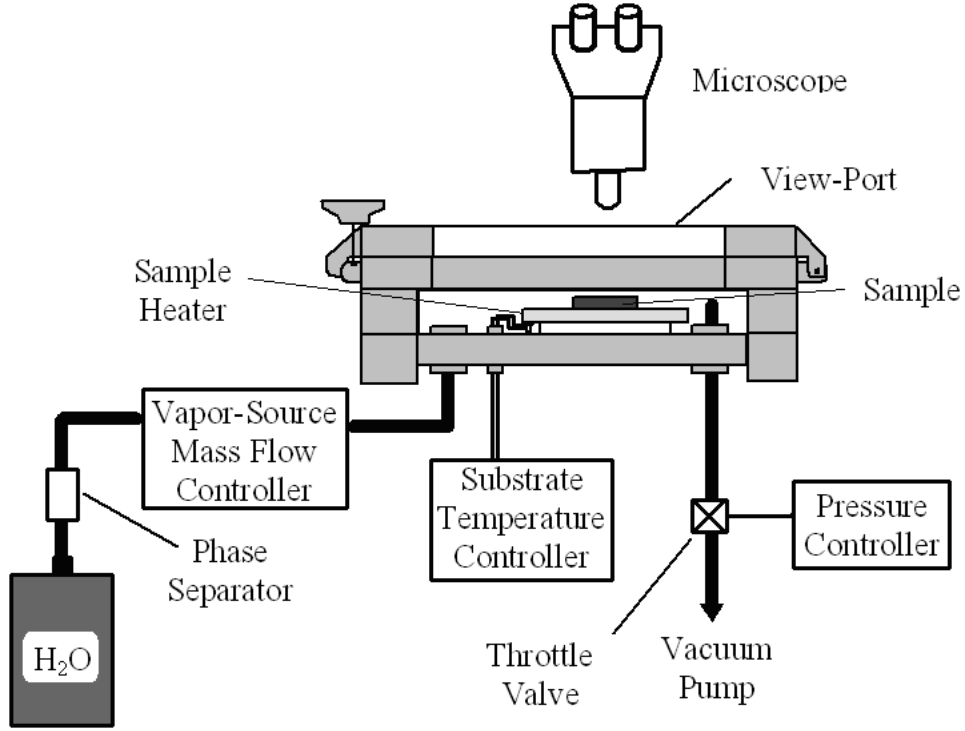


FIG. 65: Schematic diagram of our custom-built oxidation furnace complete with capability for in-situ monitoring.

puzzle for fabrication of oxide-apertured VCSELs was the formation of the oxide apertures themselves. In order to reproducibly define small features by oxidizing AlGaAs layers, it is essential to have good control over the oxidation reaction. To push VCSEL structures to their ultimate threshold limits, these apertures must constrict to  $1\ \mu\text{m}$  and below.[59]. Unfortunately, the oxidation reaction in a conventional furnace is hard to control, making it difficult to reproducibly define such small features. We have integrated a glass viewport into a cold-walled oxidation chamber to enable in-situ optical monitoring of the sample during oxidation (see Fig. 65). To prevent water vapor from condensing on the cold window and obscuring the sample, the reaction chamber is operated at low pressure (5 Torr). This low pressure also allows rapid evacuation of the chamber, which immediately halts the reaction. To gain additional control, we reduced the oxidation temperature to  $325\ ^\circ\text{C}$ , consequently slowing the oxidation rate to  $2\ \mu\text{m}$  per hour. The combination of optical monitoring, slow oxidation rate, and rapid shutoff greatly increases our control over the reaction and allows us to define small features precisely.

Real-time in-situ optical measurements of AlAs oxidation rates were performed using this system and the results were compared with a standard model [60]. Oxide-semiconductor distributed Bragg reflectors were also fabricated and measured, yielding highly-reflective mirrors suitable for vertical-cavity surface-emitting laser fabrication.

To verify that these oxides have suitable optical and mechanical properties for DBR mirror fabrication, we also measured the reflectance of oxidized DBR features. The low oxidation rate makes it impractical to oxidize large features. Therefore we constructed an imaging system capable of measuring the reflectance of small ( $\simeq 20\ \mu\text{m}$ ) features. The samples under study were composed of five periods of GaAs (695 Å) and AlAs (1530 Å) grown by molecular beam epitaxy on a GaAs substrate. Vertical posts, with square and circular cross sections ranging in size from 5 to 40 microns, were reactive-ion-etched into the wafer using the following procedure. The wafer was first covered by  $\text{Si}_3\text{N}_4$  using plasma-enhanced chemical vapor deposition and then coated with photoresist. The resist was patterned using conventional lithographic techniques, the  $\text{Si}_3\text{N}_4$  was anisotropically etched in a  $\text{CF}_3\text{H}/\text{O}_2$  plasma, and the remaining resist was removed. The patterned  $\text{Si}_3\text{N}_4$  was used as a mask for an anisotropic  $\text{BCl}_3/\text{He}$  plasma etch of the epitaxial layers, and was subsequently removed by isotropic etching in a  $\text{CF}_4/\text{O}_2$  plasma. Finally, the exposed AlAs layers in the wafer were protected from atmospheric water vapor by re-depositing 500 Å of  $\text{Si}_3\text{N}_4$  over the entire wafer. The resulting features exhibited side-wall angles less than  $5^\circ$  from perpendicular. All oxidation samples were prepared from this single wafer: immediately prior to oxidation, samples were cleaved from the wafer and the  $\text{Si}_3\text{N}_4$  protective layer was removed by a  $\text{CF}_4/\text{O}_2$  plasma etch.

The oxidation furnace, schematically depicted in Figure 65, comprises a conventional sample heater with an integral thermocouple to control the sample temperature. Pure water vapor is delivered to the chamber at a fixed flow rate through a vapor-source mass-flow controller. A feedback control system maintains the chamber pressure at 5 Torr: the system consists of a capacitance-manometer pressure sensor driving a butterfly throttle-valve on a mechanical vacuum pump. As the AlAs layers are oxidized, the near-infrared reflectivity of the DBR samples changes dramatically. By illuminating the sample with near-infrared light and viewing the reflection with a silicon CCD camera attached to a long-working-distance microscope, we easily discriminate between the oxidized and unoxidized regions. The dramatic contrast is evident in the near-infrared photograph shown in Figure

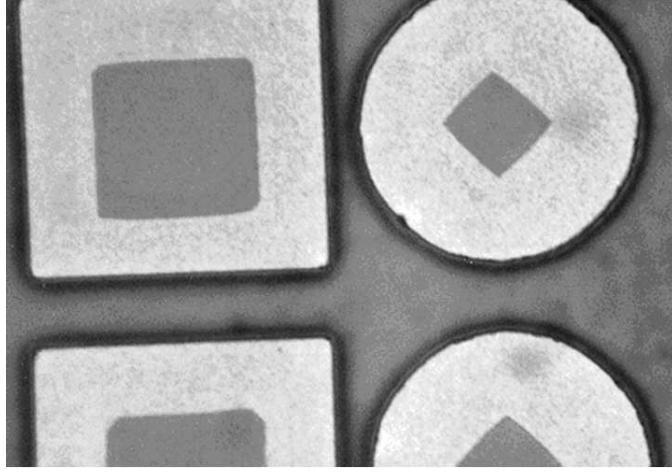


FIG. 66: Near infrared image of a sample during the oxidation process. The high refractive index contrast between the unoxidized AlAs ( $n \simeq 3.0$ ), and native oxide ( $n \simeq 1.6$ ) is readily apparent in this image.

66.

Samples were oxidized in the system at temperatures ranging from 325 to 400 °C. The color of the oxidized samples was identical for all oxidation conditions. Thick AlAs samples that were oxidized downward from the top surface of the wafer were found to be somewhat unstable mechanically, tending to delaminate from the substrate material just at the point when the layer was fully oxidized. However, laterally oxidized samples showed no tendencies to delaminate under any of the oxidation conditions discussed here, and in fact were found to be quite rugged. In addition, unprotected AlAs samples were found to degrade quite quickly (in a matter of a few days) in ambient conditions, but oxidized samples, even those oxidized at low temperatures, show no signs of degradation after nearly one year. Since the purpose of this study is to develop a process to fabricate VCSELs using laterally oxidized layers, we hereafter consider only laterally oxidized samples.

By viewing the samples through the CCD camera and charting the lateral extent of the oxide as a function of time, we measured the oxidation rate without removing the sample from the chamber or interrupting the reaction. The results are plotted in Figure 67. The temperature range studied was limited at the low end by the length of time needed to reliably measure an appreciable oxidation distance, and was limited at the high end by the components of the oxidation system, notably the elastomer seals on the chamber. For some

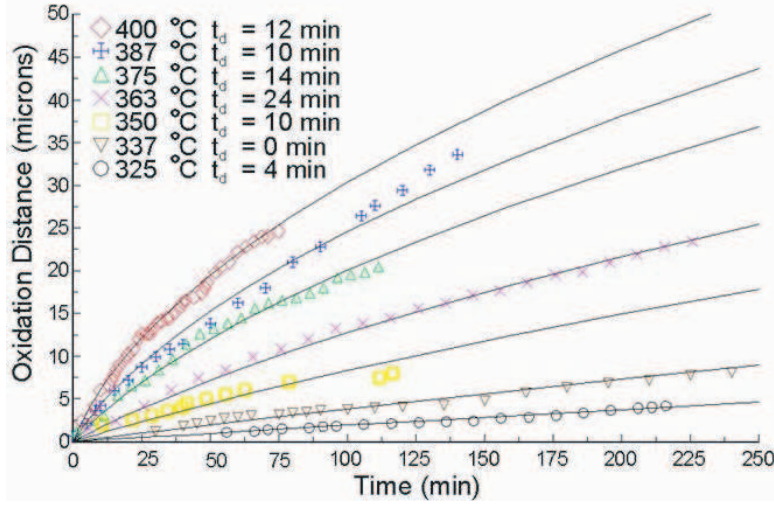


FIG. 67: Oxidation distance as a function of time for several temperatures. All oxidations were carried out at a water vapor pressure of 5 Torr and a flow rate of 500 sccm.

samples, a small time delay (approximately 5-15 min) elapsed before noticeable oxidation occurred; the delay did not vary systematically with oxidation temperature. This delay could result from uncontrolled surface oxidation in the brief time between  $\text{Si}_3\text{N}_4$  removal and sample loading.

### VCSEL Device Results

As a result of all of the previous underlying work, we designed, grew, and fabricated a lasing structure aimed at sub-mA threshold current operation. The resultant structure design was a dual oxide apertured structure employing 21 carbon-doped  $p$ -type GaAs/ $\text{Al}_{0.9}\text{Ga}_{0.1}\text{As}$  DBR mirror layers (complete with 180 Å digital alloy grades between the materials), a  $1\text{-}\lambda$  cavity region with 3 80-Å  $\text{In}_{0.2}\text{Ga}_{0.8}\text{As}$  as the active region. The bottom DBR consisted of 41 pairs of silicon doped GaAs/ $\text{Al}_{0.9}\text{Ga}_{0.1}\text{As}$   $n$ -type mirror layers *without* any grading between the layers. As seen in Figures 68, 69, we have made an *extra-cavity contacted* device (for ease of fabrication) that, when operating at room temperature, displays a threshold current of  $i_{th} = 122 \mu\text{A}$  with a threshold voltage of  $V_{th} = 2.76 \text{ V}$ . As detailed in Figure 68, we see the following behavior for lasing wavelength,  $\lambda_{lase}$ , as a function of the oxide aperture radius,  $\rho_{OX}$ :  $\lambda_{lase}$  holds steady for devices with larger oxide apertures (little effect



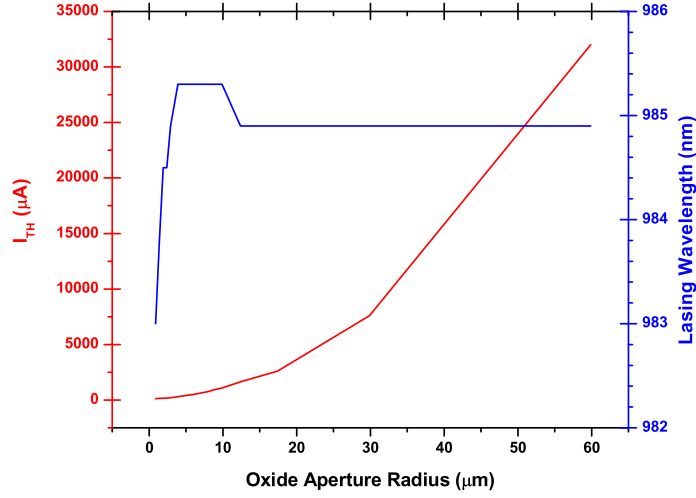


FIG. 68: Plot of  $i_{th}$  and  $\lambda_{lase}$  as a function of oxide aperture radius for an in-house design, grown, and fabricated VCSEL structure. See the accompanying text for the device description.

on the microcavity resonance condition); as the size of the aperture shrinks, the wavelength actually redshifts slightly (presumably due to device heating due to increased current crowding effects); and eventually the lasing emission blueshifts, as predicted by both the VFEM and WIMP simulations. As our “cold cavity” simulations were not performed under a coupled optical + thermal + electrical phenomenology, the effects of current crowding inducing heating in these structures was not incorporated.

One of the critical features for obtaining very efficient, low-threshold VCSELs is to ensure that the gain peak aligns with the cavity resonance under anticipated operating conditions. Indeed, this was part of the underlying motivation for development of the WIMP and VFEM tools—to incorporate such shifts *a priori* in our designs. One is never guaranteed, however, that growth will match the design conditions. To test that the gain peak was close to the cavity resonance for the smallest oxide aperture devices (first data points, lowest  $i_{th}$  in Figures 68, 69), we performed similar experiments in a temperature controlled probe-stand. It is well known that the gain peak shifts much more rapidly with temperature than the cavity resonance (see, e.g., [61] and references therein). Hence, but performing measurements of  $i_{th}$  as a function of temperature, we may infer the amount of mismatch in gain and cavity

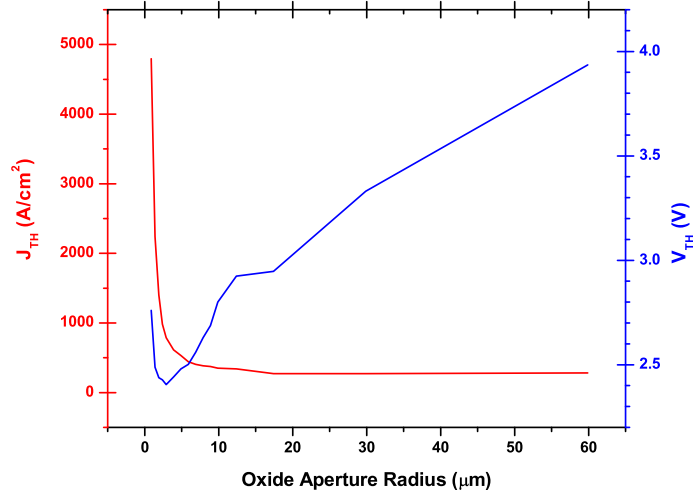


FIG. 69: Plot of  $j_{th}$  and  $V_{th}$  as a function of oxide aperture radius for an in-house design, grown, and fabricated VCSEL structure. See the accompanying text for the device description.

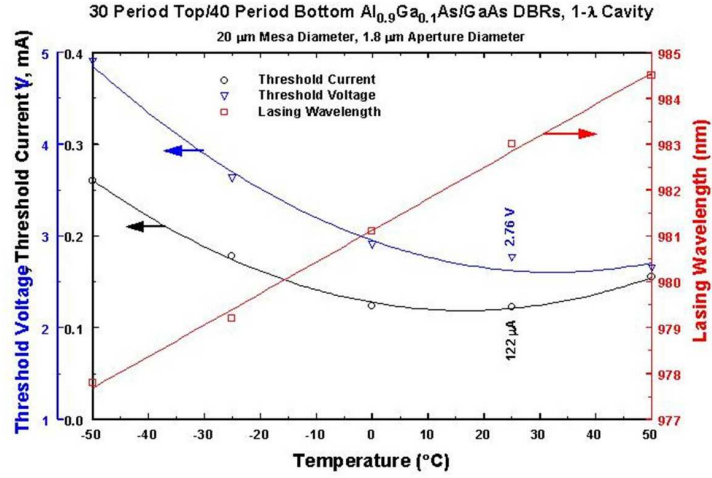


FIG. 70: Plot of  $i_{th}$ ,  $V_{th}$ , and  $\lambda_{lase}$  as a function of temperature for one of the oxide aperture VCSELs shown in Figure 68. The minimum for  $i_{th}$  and  $V_{th}$  occurs near 17 °C, indicating good match between design and the ultimate device results.

resonances. Figure 70 shows the results of this experiment.

From this figure, it is evident that our design was very close to ideal, in that, for a structure with  $\rho_{OX} = 1.8\mu\text{m}$ , the minima in both  $i_{th}$  and  $V_{th}$  occurs just slightly below room temperature, nominally 17 °C. For completeness, the shift in  $\lambda_{lase}$  with temperature is also plotted.

## SUMMARY AND FUTURE EFFORTS

In the AFOSR supported in-house research project, we embarked on an effort to generate extremely low-threshold VCSELs. To support this effort, state of the art simulation suites were developed to outline the optical physics of microcavity structures, including etched post designs, and oxide apertures layers with or without spatial tapered profiles. The two methods, the weighted index method with parasitic mode coupling (WIMP), and the full vector finite-element method (VFEM), has been applied to many VCSEL structures. We have succeeded in predicting lasing wavelength blueshifts with decreasing oxide aperture diameters, both for published results and for our own in-house made devices. We have successfully managed to describe the relative design merits for inclusion of oxide apertures in microcavity resonator designs, again through explaining and interpreting the heretofore confusing results found in the literature. We have also shown the benefits toward applying tapered oxide aperture designs for “blunting” the diffraction losses incurred by “blunt” apertures. Finally, in the design arena, we have developed quasi-analytic means for calculating the transmission and reflection properties of graded-layer structures, and showed the utility of this *generalized interface* approach for design of DBR mirrors and VCSELs using digital alloying grading at the material interfaces.

Our in-house growth and fabrication yielded VCSELs operating cw at room temperature with threshold currents as low as 122  $\mu\text{A}$ . For a *manufacturable* (i.e. high-yield) structure utilizing current injection through the  $p$ - and  $n$ -DBR mirrors, this was less than a factor of 2 from the best published results at the time, and less than a factor of 14 from the best devices *period*.

As a result of this research effort, we have also greatly increase the growth and fabrication capability at AFRL. An overhaul of the *Varian GEN II* MBE machine used for this project has results in VCSEL class material. We have also demonstrated a custom built steam oxidation furnace for creation of native oxides of aluminum from AlGaAs material, com-

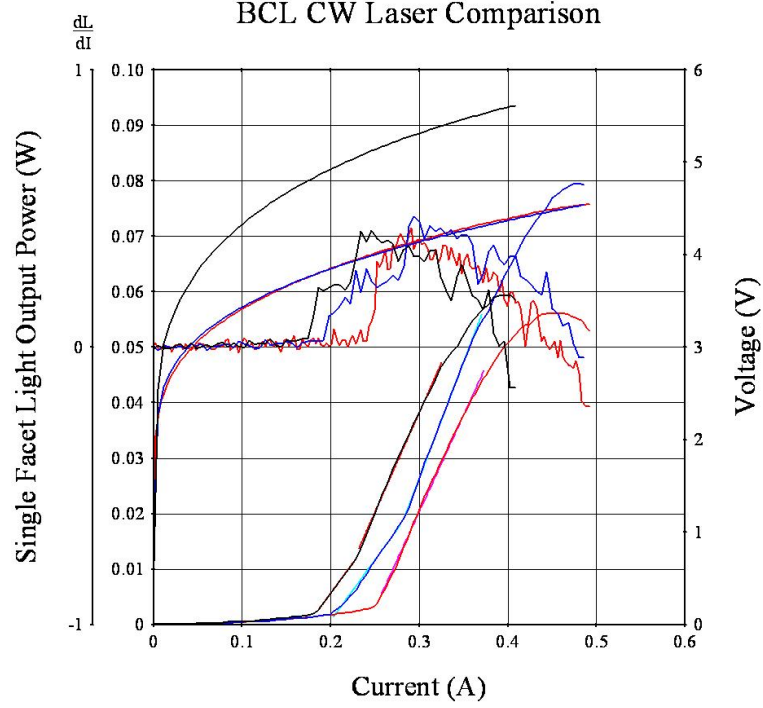


FIG. 71: Plot the reduced voltage needed to drive a *bipolar* cascade edge emitting laser. A detailed description of this device is not in the scope of this report, and the reader is encourage to consult reference [62] for further details on this newer effort.

plete with in-situ monitoring allowing for high-precision control of oxide-apertured VCSEL structures.

Future efforts for optoelectronics and semiconductor device research will see spillover benefits from the efforts made on this project. Indeed, we have embarked on efforts to generate *interband* (so-called “bipolar”) cascade lasers for the purpose of radiofrequency-photonic links. These devices, which incorporate Esaki tunnel junctions as small-resistance interconnects between lasing active regions, are predicted to have superior noise and overall link gain characteristics compared to tradition laser diodes, a feature we aim to demonstrate experimentally. Indeed, we have already shown single- and multi-color emission from edge emitting structures (see Figure 71 and [62], for example), and we are now pursuing VCSEL geometries for device improvements. This, and other efforts, will be the subject of a future report.

## ACKNOWLEDGMENT

This work marks the effort of several researchers, many of whom are no longer with AFRL. In particular, the effort of Dr. John P. Loehr (project lead from 1 March 1996 - 1 Aug 2000), Dr. Stewart A. Feld (principle engineer, developer of the custom oxidation furnace), and contributions by Dr. Michael J. Noble (conferred a PhD from the Air Force Institute of Technology for his work in developing WIMP and VFEM codes) and Dr. Ralph E. Sherriff (prime consultant for software development, many of the theoretical underpinnings of the VCSEL gain calculations, and experimental setups for testing reflectivity of oxide DBRs).

In addition, the Optoelectronics team that pioneered this work would like to acknowledge the following individuals and organizations for their support and aid in these efforts:

- \* Dr. Alan Craig, Dr. Kent Miller, and Dr. Gernot Pomrenke for the support of this research at AFOSR through in-house grant LRIR 2305DW01.
- \* Mr. Paul Cassity of Wyle Laboratories, Wright-Patterson AFB, for aid and assistance with plasma processing of samples (etching and deposition).
- \* Mrs. Carol Isbill (AFRL/SNDD) and Mr. Joseph Breedlove (Wyle Laboratories), for the efforts on the metal evaporation systems for good Ohmic contacts to our devices.
- \* Mr. Larry Callahan (Wyle Laboratories) for aid in packaging and testing of these devices.
- \* Mr. David Wilson, (Wyle Laboratories), purchasing representative for our Division, for putting up with sometimes *insane* requests to have what we wanted immediately!
- \* Drs. Joseph Van Nostrand and Kent Averett, both of AFRL/MLPSM, for coming to our rescue numerous times when growth just wasn't happening as planned, and figuring out what was wrong with the system or growth methodology when the rest of us were stumped.
- \* And finally, Mr. James Ehret, for inhuman efforts to always seek to improve the quality of the MBE material he grew for this effort (and for being one of the most flexible and cooperative growers one could imagine working with!).

---

\* Electronic address: `Thomas.Nelson@wpafb.af.mil`; This work was supported by the Air Force Office of Scientific Research under LRIR 2305DW01.

- [1] D. Talwar, J. Loehr, and B. Jogai, *Physical Review* **B-49**, 10345 (1994).
- [2] J. Loehr, *Physical Review* **B-50**, 5429 (1994).
- [3] J. Loehr, *Physical Review* **B-52**, 2374 (1995).
- [4] J. Jewell, J. Harbison, A. Scherer, Y. Lee, and L. Florez, *IEEE Journal of Quantum Electronics* **27**, 1332 (1991).
- [5] D. Huffaker, D. Deppe, and J. Shin, *Applied Physics Letters* **67**, 4 (1995).
- [6] K. Choquette, W. Chow, G. Hadley, H. Hou, and K. Geib, *Applied Physics Letters* **70**, 823 (1997).
- [7] S. Brorson, H. Yokoyama, and E. Ippen, *IEEE Journal of Quantum Electronics* **26**, 1492 (1990).
- [8] T. Baba, T. Hamano, F. Koyama, and K. Iga, *IEEE Journal of Quantum Electronics* **27**, 1347 (1991).
- [9] T. Baba, T. Hamano, F. Koyama, and K. Iga, *IEEE Journal of Quantum Electronics* **28**, 1310 (1992).
- [10] G. Hadley, *Optics Letters* **20**, 1483 (1995).
- [11] E. Hegblom, D. Babić, B. Thibeault, and L. Coldren, *Applied Physics Letters* **68**, 1757 (1996).
- [12] R. Harrington, *Time-Harmonic Electromagnetic Fields* (McGraw-Hill Book Company, New York, 1961).
- [13] J. Jackson, *Classical Electrodynamics* (John Wiley and Sons, 1975), 2nd ed.
- [14] D. Burak and R. Binder, *IEEE Journal of Quantum Electronics* **33**, 1205 (1997).
- [15] P. Kendall, M. Adams, S. Ritchie, and M. Robertson, *IEE Proceedings* **134 pt A**, 699 (1987).
- [16] M. Robertson, P. Kendall, S. Ritchie, P. McIlroy, and M. Adams, *IEEE Journal of Lightwave Technology* **7**, 2105 (1989).
- [17] T. Ikegami, *IEEE Journal of Quantum Electronics* **QE-8**, 470 (1972).
- [18] R. Michalzik and K. Ebeling, *IEEE Journal of Quantum Electronics* **31**, 1371 (1995).
- [19] D. Babić, K. Streubel, R. Mirin, N. Maralit, J. Bowers, E. Hu, D. Mars, L. Yang, and K. Carey, *IEEE Photonics Technology Letters* **7**, 1225 (1995).

- [20] G. Yang, M. MacDougal, and P. Dapkus, *Electronics Letters* **31**, 886 (1995).
- [21] K. Choquette, K. Lear, R. Schneider, K. Geib, J. Figiel, and R. Hull, *IEEE Photonics Technology Letters* **7**, 1237 (1995).
- [22] E. Snitzer, *Journal of the Optical Society of America* **51**, 491 (1961).
- [23] T. Okoshi, *Optical Fibers* (Academic Press, New York, 1982).
- [24] C. Balanis, *Advanced Engineering Electromagnetics* (John Wiley and Sons, 1989).
- [25] G. Hadley, K. Choquette, and K. Lear, in *Technical Digest, Conference on Lasers and Electro-optics* (1996), 1996 Technical Digest Series, p. 425.
- [26] D. Deppe, T.-H. Oh, and D. Huffaker, *IEEE Photonics Technology Letters* **9**, 713 (1997).
- [27] B. Saleh and M. Teich, *Fundamentals of Photonics* (John Wiley and Sons, Inc., 1991).
- [28] G. Agrawal and N. Dutta, *Long-Wavelength Semiconductor Lasers* (Van Nostrand Reinhold, 1986).
- [29] L. Lewin, *IEEE Transactions on Microwave Theory and Techniques* **MTT-23**, 576 (1975).
- [30] J. Kardontchik, *IEEE Journal of Quantum Electronics* **QE-18**, 1279 (1982).
- [31] J. Jin, *The Finite Element Method in Electromagnetics* (John Wiley and Sons, Inc., 1993).
- [32] J. C. Nedelec, *Numerische Mathematik* **35**, 315 (1980).
- [33] *Partial Differential Equation Toolbox 2.0: User's Guide*, The MathWorks, Inc. (1997), documentation for Beta test.
- [34] Y. Saad, *Numerical Methods for Large Eigenvalue Problems* (Manchester University Press, 1992).
- [35] J. Maloney, M. Kesler, and G. Smith, in *13th Annual Review of Progress in Applied Computational Electromagnetics* (1997), pp. 900–908.
- [36] Z. Sacks, D. Kingsland, R. Lee, and J. Lee, *IEEE Transactions on Antennas and Propagation* **43**, 1460 (1995).
- [37] J.-H. Shin, I.-Y. Han, and Y.-H. Lee, *IEEE Photonics Technology Letters* (1998).
- [38] D. Deppe, D. Huffaker, Q. Deng, T.-H. Oh, and L. Graham, in *LEOS '97 Conference Proceedings* (IEEE LEOS, 1997), pp. 287–288.
- [39] M. Noble, J. Loehr, and J. Lott, *IEEE Journal of Quantum Electronics* (1997), in Review.
- [40] E. Hegblom, B. Thibault, and L. Coldren, in *IEEE Summer Topical Meetings: Vertical-Cavity Lasers* (Montreal Canada, 1997).
- [41] D. Deppe, D. Huffaker, T.-H. Oh, H. Deng, and Q. Deng, *IEEE Journal of Selected Topics in*

- Quantum Electronics **3**, 893 (1997).
- [42] R. Graglia, D. Wilton, and A. Peterson, IEEE Transactions on Antennas and Propagation **45**, 329 (1997).
  - [43] S. Polstyanko and J.-F. Lee, Journal of Lightwave Technology **13**, 2290 (1995).
  - [44] T. Itoh, G. Pelosi, and P. Silvester, eds., *Finite Element Software for Microwave Engineering* (John Wiley and Sons, Inc., 1996).
  - [45] Z. Cendes, IEEE Transactions on Magnetics **27**, 3953 (1991).
  - [46] P. Silvester and R. Ferrari, *Finite Elements for Electrical Engineers* (Cambridge University Press, 1996), 3rd ed.
  - [47] M. Wong, M. Prak, and V. Fouad Hanna, in *IEEE Microwave Theory and Techniques (MTT-S) Digest* (1995), pp. 285–288.
  - [48] D. Sun, J. Manges, X. Yuan, and Z. Cendes, IEEE Antennas and Propagation Magazine **37**, 12 (1995).
  - [49] J.-F. Lee, D. Sun, and Z. Cendes, IEEE Transactions on Magnetics **27**, 4032 (1991).
  - [50] D. Pozar, *Microwave Engineering* (Addison-Wesley, 1990).
  - [51] M. Noble, J. Lott, and J. Loehr, IEEE Journal of Quantum Electronics **34**, 606 (1998).
  - [52] M. Noble, J. Loehr, and J. Lott, in *Proceedings of the SPIE* (1999), vol. 3625, pp. 359–370.
  - [53] P. Newman, J. Pamulapati, H. Shen, M. Taysing-Lara, J. Liue, G. Simonis, B. Koley, M. Dagenais, S. Feld, and J. Loehr, Journal of Vacuum Science and Technology **B-18**, 1619 (2000).
  - [54] T.-H. Oh, D. Huffaker, and D. Deppe, IEEE Photonics Technology Letters **9**, 875 (1997).
  - [55] A. Bond, P. Dapkus, and J. O’Brien, IEEE Photonics Technology Letters **10**, 1362 (1998).
  - [56] E. Hegblom, D. Babić, B. Thilbeault, and L. Coldren, IEEE Journal of Selected Topics in Quantum Electronics **3**, 379 (1997).
  - [57] D. Aspnes, S. Kelso, R. Logan, and R. Bhat, Journal of Applied Physics **60**, 754 (1986).
  - [58] M. Born and E. Wolf, *Principles of Optics* (Pergamon Press, Oxford, England, 1980), sixth ed.
  - [59] A. Sugg, E. Chen, N. Holonyak Jr., K. Hsieh, J. Baker, and N. Finnegan, Journal of Applied Physics **74**, 3880 (1993).
  - [60] S. Feld, J. Loehr, R. Sherrieff, J. Wiemer, and R. Kaspi, IEEE Photonics Technology Letters **10**, 197 (1998).
  - [61] J. Loehr, *Physics of Strained Quantum Well Lasers* (Kluwer Academic Publishers, 1997).



- [62] W. Siskaninetz, J. Ehret, T. Dang, J. Van Nostrand, J. Lott, and T. Nelson Jr., IEE Electronics Letters **38**, 1259 (2002).